IDEA League

Master of Science in Applied Geophysics

Research Thesis

Inversion algorithm development for passive electromagnetic detection of line sources

Prototyping a submarine power cable tracking system

Tobias Stolz

August 9, 2019

Inversion algorithm development for passive electromagnetic detection of line sources

Prototyping a submarine power cable tracking system

Master of Science Thesis

for the degree of Master of Science in Applied Geophysics

by

Tobias Stolz

August 9, 2019

IDEA LEAGUE
JOINT MASTER'S IN APPLIED GEOPHYSICS

Delft University of Technology, The Netherlands
ETH Zürich, Switzerland
RWTH Aachen, Germany

Dated: *August 9, 2019*

Supervisor(s):

Prof. dr. ir. E. C. Slob

M. Künzel

Committee Members:

Prof. dr. ir. E. C. Slob

M. Künzel

Prof. dr. H. Maurer

Confidentiality Statement

This report is under confidentiality and it is not to be made public until the 30^{th} of August, 2020.

Delft University of Technology
August 9, 2019

Tobias Stolz

Abstract

The position of installed submarine power cables is often not accurately known for several reasons. The precise knowledge of the cable position is important for the maintenance process and necessitates the need for cable tracking systems. Current systems are in many cases imprecise and have a short sensing distance, limited to a few meters. A device with better accuracy and sensing range is in demand for enhancing the cable maintenance process. Three new inversion algorithms are introduced which invert the passive electromagnetic field created from an injected signal in the target cable. The cable is treated like a line source. This can be seen as an inverse source location finding problem, while the source time signature is known. The algorithms are tested on synthetic data, modeling a power cable in homogeneous sea water with noise. Several parameters like sensor array, dip angle of the cable and relative position to the system are analyzed. The influence of soil and the sea surface are studied on synthetic data created from a numerical three-layer forward model. Additionally, a prototype is developed, and different processing schemes are presented and compared. The system is tested with different inversion algorithms on a field cable on land.
A solution is found which can determine the cable position accurately in sea water with noise terms for a distance up to 6 m. However, this system is highly sensor array dependent. A second inversion method gives a smaller sensing range of 5 m but can be used with more versatility. In a different modeled scenario without noise terms, the cable is buried in marine sediments and air is on top of a layer of sea water. The sensors are in the sea water layer. The soil has a great impact on the accuracy of the inversion. In some cable-system-orientations, the absolute error caused by the layered earth exceeds 1 m. The prototype is successfully tested on a field cable for different scenarios. An inverted cable position in a global reference frame can be obtained by including a motion sensor.

Acknowledgements

I am grateful to the team of League Geophysics for giving me the opportunity of working on an exciting topic in a friendly and casual environment in the beautiful city of Amsterdam. Michiel Künzel, Wouter Wester and Martin Koelman, keep on with the good work you do and maintain the enthusiastic spirit of the company. I am looking forward for some challenging table tennis matches when I am back at the office! I owe my deepest gratitude to Evert Slob, my supervisor from TU Delft, for his guidance, availability and willingness to support me in my work. I would also like to thank Dieter Werthmüller from TU Delft for introducing me into EM modeling.
Finally, I would like to say thank you to my colleges from my study program: I had a blast with you the last two years. It was an exciting and merry time. I am already looking forward for a reunion.

Delft University of Technology — Tobias Stolz
August 9, 2019

Table of Contents

List of Figures

List of Tables

Abbreviations

AC	Alternating Current
Array	Sensor Array
AUV	Autonomous underwater vehicle
CTS	Cable Tracker System
CTS $\mathbf{I}^m$ ($\mathbf{II}^m$, $\mathbf{III}^m$)	Cable Tracker System I (II, III) with motion sensor
CTS $\mathbf{I}^I$ ($\mathbf{II}^I$)	Cable Tracker System I (II) with known current
C	Cable Setup
DC	Direct Current
DFT	Discrete Fourier Transformation
EM	Electromagnetic
FIR	Finite Impulse Response
FFT	Farst Fourier Transformation
GPS	Global Positioning System
HV	High Voltage
IIR	Infinite Impulse Response
LV	Low Voltage
MV	Medium Voltage
PS	Power Spectrum
ROV	Remote Operated Vehicle

UDP	User Datagram Protocol
USBL	Ultra Small Baseline
XLPE	Cross-linked Polyethylen

Variables

A_{-}	Amplitude of the up-going electric field
$\mathbf{B}$	Magnetic flux density
$\hat{\mathbf{B}}$	Magnetic flux density in Laplace domain
$\mathbf{B}^i$	Magnetic flux density measurement of sensor i
$\mathbf{B}^{i'}$	Transformed magnetic flux density measurement of sensor i
$\mathbf{c} = (c_x, c_y, c_z)^T = (c_r, c_\theta, c_y)^T$	Cable position relative to sensor array center
$\mathbf{c}^{'} = (c_x^{'}, c_y^{'}, c_z^{'})^T = (c_r^{'}, c_\theta^{'}, c_y^{'})^T$	Transformed cable position relative to sensor array center
$\mathbf{c}^i = (c_x^i, c_y^i, c_z^i)^T = (c_r^i, c_\theta^i, c_y^i)^T$	Cable position relative to sensor i
$\mathbf{c}^{i'} = (c_x^{i'}, c_y^{i'}, c_z^{i'})^T = (c_r^{i'}, c_\theta^{i'}, c_y^{i'})^T$	Transformed cable position relative to sensor i
$\hat{\mathbf{c}}^{i'}$	Directional vector pointing from sensor i to the cable in the transformed coordinate system
df	Frequency resolution
$\delta(\cdot)$	Delta function
δ	Skin depth
$\mathbf{E}$	Electric field
$\hat{\mathbf{e}}_x$, $\hat{\mathbf{e}}_y$, $\hat{\mathbf{e}}_z$	Unit vectors of Cartesian coordinates
$\hat{\mathbf{e}}_x^{'}$, $\hat{\mathbf{e}}_y^{'}$, $\hat{\mathbf{e}}_z^{'}$	Unit vectors of transformed Cartesian coordinates
$\hat{\mathbf{e}}_N$, $\hat{\mathbf{e}}_E$, $\hat{\mathbf{e}}_g$	Unit vectors pointing North, East and parallel to gravity

$\hat{\mathbf{e}}_\phi$	Unit azimuth vector
ϵ	Permitivity
ϵ_0	Permitivity in free-space
ϵ_r	Relative permitivity
ϵ_s, ϵ_w, ϵ_a	Relative permitivity of soil, sea water and air
η, η_s, η_w, η_a	Conductivity function (global, soil, water and air)
f_c	Cutoff frequency
f_s	Injected tone frequency
$\widetilde{\mathbf{G}}$	Greens function in wavenumber-Laplace domain
Γ	Vertical wavenumber
γ	Propagation constant
$\hat{\mathbf{H}}$	Magnetic field in Laplace domain
$\widetilde{\mathbf{H}}$	Magnetic field in wavenumber-Laplace domain
I	Current
$\hat{\mathbf{I}}$	Signal in Laplace domain
$\mathbf{J}$	Current density
$\hat{\mathbf{J}}^e$	Electric line source in Laplace domain
$\widetilde{\mathbf{J}}^e$	Electric line source in wavenumber-Laplace domain
$K_1(\cdot)$	Bessel function of second kind
k_x, k_y	Horizontal wavenumber
μ	Permeability
μ_0	Permeability in free-space
μ_r	Relative permeability
μ_s, μ_w, μ_a	Relative permeability of soil, sea water and air
n_s	Number of sensors
ω	Angular frequency
Φ, Ψ, Θ	Euler angels
R_{sw}, R_{wa}	Global reflection coefficient of the soil-water boundary and water-air boundary

r	Distance
r_{sw}, r_{wa}	Local reflection coefficient of the soil-water boundary and water-air boundary
$\mathbf{r}$	Displacement vector
ρ	Resistivity
ρ_s, ρ_w, ρ_a	Resistivity in soil, water and air
$\mathbf{s} = (s_x, s_y, s_z)^T$	Sensor array center
$\mathbf{s}^i = (s_x^i, s_y^i, s_z^i)^T$	Position of sensor i
$\mathbf{s}^{i'}$	Transformed position of sensor i
$\widetilde{\mathbf{s}}^{i'}$	Transformed position of sensor i, shifted along the cable
σ	conductivity
σ	Standard deviation
σ^2	Variance
$sign(\cdot)$	Sign function
$\mathbf{T}$	Transformation matrix
ζ, ζ_s, ζ_w, ζ_a	Resistivity function (global, soil, water and air)

Chapter 1

Introduction

1-1 Introduction

The submarine power cable market is a growing industry which puts cables, a crucial infrastructure of modern society, in the seabed. Cables installed in the seabed become virtually undetectable. After the installation of a submarine cable, the knowledge of its position is inaccurate. Additionally, the cable is moving in its lifespan due to sediment movement and other external influences. The movement of the cable is an additional factor which contributes to a false expected object's position. The maintenance process comprises locating of the cable for updating the current position to ensure an unobstructed repairing in case of failure. Monitoring the cable's burial depth is required to find exposed parts. These are sensitive to damage from the shipping industry and needs to be covered with sediments. Depending on the operator's policy, the insurance requirements and the marine environment where the cable is laid out, it is required to detect the current position a few times per decay up to several times per year. Tracking systems are required for performing this task which can rely on various different concepts. Current available systems often cannot guaranty the required accuracy which is needed for this task and lack in detecting distance. Cable operators often ask for a detected cable position which has a relative error to the true cable position that is less than 10 %. The required detecting distance depends on the survey but it is in general below 5 m. This report introduces three new algorithms for inverting the electromagnetic (EM) field from a cable, modeled as a line source. The performance of the systems is evaluated on synthetic data for the influence of noise, and the sea floor and water surface. Finally, a prototype is developed and data from a measurement campaign on a field cable acquired. The inversion algorithms are tested on the data set.

First, background information about submarine power cables are given which concludes with a short market overview of available cable tracking systems and their advantages and limitations. Based on these details, specific requirements and properties are found which are considered when developing the new system. Thereafter, analytical and numerical models are stated and compared which are used for creating synthetic data. Three novel inversion

Type	Abbreviation	Voltage
Low Voltage	LV	$< 0.6\,\mathrm{kV}$
Medium Voltage	MV	$0.6 - 69\,\mathrm{kV}$
High Voltage	HV	$69 - 230\,\mathrm{kV}$
Extra High Voltage	EHV	$> 230\,\mathrm{kV}$

Table 1-1: Voltage classification according to the ANSI C84.1-1989 standard.

algorithms are briefly explained in the next chapter, and tested and studied on synthetic data afterwards. Besides a study of possible sensor arrays, the behaviour in a noise disturbed environment, and the impact of seafloor and the water surface are examined. The next chapter is about the cable tracking system prototype. Its components and in particular the processing schemes are briefly explained. The prototype is tested using different settings on a field cable. The report ends with a summary of the project, its outcomes and an outlook about tasks left for finalizing a product.

1-2 Background

The era of electrical engineering started in the 19^{th} century and made electricity to a resource of modern society. With this shift came a requirement for new infrastructure and new ways of transporting electricity, including the transport of electric power through water like rivers, lakes and seas. One of the first documented underwater cable was laid across the Isar River in the south of Germany in 1811 [1]. Since then, extensive research has been carried out, enhancing cable design and the capability of transporting more energy over a larger distance. Nowadays, submarine power cables operated at voltages of more than 500 kV and with capacities of 500 MW or greater. Energy can be transported hundreds of kilometers. A good example is the NorNed cable, currently the worlds longest submarine cable, with a length of 580 km and a capacity of 700 MW that connects the electrical grids of Norway and the Netherlands [2].

Two key parameters in choosing an offshore power cable are the operating voltage and the type of operating current. According to the ANSI C84.1-1989 standard, voltage is classified as low voltage (LV), medium voltage (MV), high voltage (HV) and extra high voltage (EHV) which is specified in Table 1-1. Submarine power cables run in general under an operational voltage and the current changes corresponding to the power that is transported. Most electrical power transmission systems use alternating current (AC) in a three-phase design for MV applications. A transformer can easily change the voltage as required and the need for a converter at each site of the line is eliminated. Even though it is project specific, cable operators prefer often direct current (DC) for distances larger than 50 km to reduce the reactive power which limits an AC cable design to smaller distances [3][4].

1-2-1 Applications of submarine power cables

Modern submarine cables serve multiple purposes. Islands that are near the shore can be connected with the mainland power grid through submarine power cables. The often inefficient

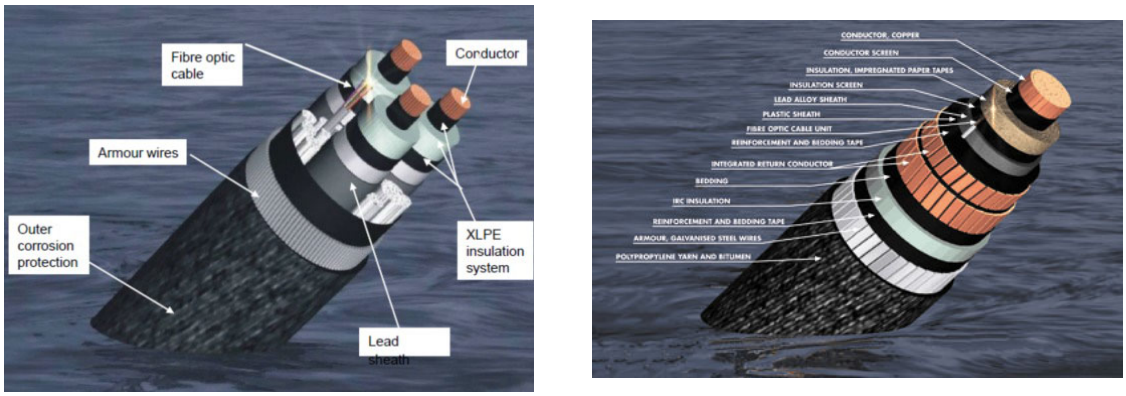

(a) AC power cable

(b) DC power cable

Figure 1-1: Cross section of an AC and DC submarine power cable [7].

power generator, such as a diesel generator, can be replaced which is more economically and ecologically beneficial. Whereby the maximum economical length of these cables is $10-30$ km, islands which are located further away from the mainland were not connected with a submarine cable for a long time due to the dramatically increase in losses with distance in an AC system. The island Heligoland, which is 53 km before the coast of Germany, got its power connection to the shore not before 2009 by a MVAC cable [5].
Submarine cables are able to connect autonomous grids. Using HVDC current allows regions with different frequency control systems to be merged and it allows for high power transmission over long distances. Autonomous grids may have different load peaks due to time shifts and consumer behaviour. Additionally, the energy generation might differ and electricity is produced only at certain times which is often the case with renewable energies. Both factors can lead to power shortage or surplus and this can be compensated by connecting grids.
With the increased installation of offshore wind farms in recent years, the need for submarine cables rose. Inside the wind farm, the turbine generators are usually spaced 300-800 m apart and they are interconnected with three-phase MVAC cables [6]. The connection of the turbine interconnector grid to the shore is usually also of an MVAC type for small wind farms. A HVAC connection is required when there are many turbines, a large power output or large distance to the shore. In those cases, a step-up transformer on an offshore platform is typically required. In rare cases, a HVDC connection is more economical. However, it requires converter stations both offshore and onshore and is therefore usually reserved for very large wind farms or grid connections.
Another application where submarine power cables play an important role is the power transport across rivers, channels, straits, fjords or bays. The type of current and strength of voltage depends on the transport design at the endings of the submarine cables, which can be AC or DC, depending on the purpose of the power line.
Other applications of submarine power cables are the connection of offshore drilling platforms with the shore, heating cables for pipelines and power supply of subsea observatories like Tsunami pre-warning systems [6].

1-2-2 Submarine cable design

A typical submarine power cable consists of one or multiple conductors, an insulation system, a water-blocking sheath and armoring. In some cases, a fibre optic cable for telecommunication, cable integrity monitoring and data transport is added into the cable design. The cross section of a typical three-phase AC cable and a DC cable is shown in Figure 1-1.

The conductor

The conductor is made of copper or aluminium. Even though aluminium is cheaper in relation to the current-carrying capability, most submarine power cables have a copper conductor since a smaller cross section is required and material in the outer layer can be saved. In any case, both materials have their benefits and disadvantage and their use depends on the requirements of the projects and the metal market. The conductor can vary in shape between hollow and solid. In some cases, a single conductor is preferred where in others cases thinner single conductors are bundled to a strand. Solid conductors are preferred for cross sections up to 400 mm and are easily manufactured. Hollow cables and cable bundles are used to reduce the loss due to the skin effect and to reduce the material needed [6]. The skin effect describes an EM interaction which occurs in AC circuits and which causes most of the current in a circuit to flow at the outer edge of the conductor [8]. Recent research concerns superconducting transmission lines which could reduce energy loss due to transmission significantly [9]. According to [10], around 6% of all electricity generated in United States is lost due to inefficient transmission which could potentially be reduced by superconducting cables.

The insulation system

The insulation has the purpose to stop current flowing from the extremely high potential in the conductor to the low potential of the surroundings. The most common insulator for LV to HV submarine power cables is cross-linked polyethylene (XLPE). Even though XLPE could be used as an insulator for higher voltages, no suitable joints exist which excludes its use for cables much longer than 50 km operated under HV. If XLPE is used to insulate HVDC, space charge phenomena can occur where charge accumulates at certain places and causes disadvantageous electric field peaks [11]. This problem can be solved by using special formulations of XLPE. Another common insulation is oil-filled paper which can be used in AC and DC designs up to HV. Under operation, the oil is under pressure and controlled by a station at shore. Channels are required to enable hydraulic communication - often the interior of a hollow conductor is used for oil transport. Due to the required hydraulic communication, cable length is restricted to $30 - 60$ km. For HVDC, mass-impregnated paper insulation is used [6].

Water-blocking sheath and armoring

The insulation needs to be kept dry to guarantee functionality. In HV cables, a metallic sheath around the insulation layer is used which can be aluminium, lead or copper. In LV and MV

setups, non-metallic shielding is often sufficient. An armoring provides the necessary tension stability and mechanical protection. A submarine cable is exposed to its biggest stress during installation which is caused by the hanging of the cable and the movement of the installation vessel. If a (subsea) power cable bends more than its design bending radius, damage may result which can lead to an interruption in current flow through the cable. In the worst case, this can lead to a faulty cable, requiring highly costly repairs. Additionally, the cable needs to be protected against other installation tools, fishing gear and anchors. Typical armoring consists of $2 - 8\,\text{mm}$ thick steel wires which are wound around the cable. For protecting against corrosion, the steel wires are often coated with zinc. A final outer layer preserves the corrosion protections from scratches. It is commonly made of a polymer or yarn [6].

1-2-3 Cable tracker systems

Cable failures

Failure of submarine cable can have multiple reasons which can be separated in three categories: External aggression, manufacturing deficiencies and other. External aggression can be caused by fishing, anchors, abrasion and geological disturbance (subsea earthquakes, rock falls in fjord areas, turbidites or mass flows etc). It accounts for more than 90% of all cable failures between 2010-2015 [12]. According to [13], more than 200 cable failures per year are reported. In case of a failure, the cable needs to be repaired quickly, considering its impact on society and economy. Tracking systems are used as a cost effective and accurate localization method for cables. The detection of the cable depth is in particular important in the cable maintenance process [14]. According to industrial standards, cables should be buried in waters with a depth of 1500m or less. Burial depth should be around $0.6 - 3\,\text{m}$ to ensure adequate protection against outside influence [15].

Cable tracking

A variety of techniques are available for carrying out this task. In some cases a diver, a remote operated vehicle (ROV) or an autonomous underwater vehicle (AUV) brings the measuring equipment close to the estimated cable position for tracking. In other cases, the sensors are dragged behind a vessel which is especially suitable for shallow water measurements.

Cable tracking methods

Several different methods of cable tracking exist. Visual tracking can be used when the cable is not buried. It is limited by visibility, which is usually poor in coastal water and at a continental shelf. Artificial light illuminating the object solves the problem but adds blurring artefacts to the image because of scattering and attenuation effects [16]. Filtering and signal processing are required to improve detection accuracy and for automation which uses deterministic and statistical methods [17].

Sonar methods use acoustical waves for detection. Sound is able to penetrate the seabed and can in some cases detect buried objects. Sonar methods perform generally better than visual techniques. An overview of sonar imagery techniques is described in [18]. The performance

is limited in shallow-water and in complex geological environments because of reflection and scattering effects of propagating sound waves [16]. In some cases, the acoustic contrast of the cable within the surrounding sediments is not high enough for a detectable object [19]. Acoustic detection can be carried out with sidescan sonar which is limited to unburied cables or a sub-bottom profiler which permits detection of buried cables. [20].

Passive magnetic surveys can detect the horizontal location of a cable well but have difficulty reliably determining a cable's burial depth. It performance is similar on unburied and buried cables. Future cables might lack in paramagnetic materials which is a fundamental condition for a detectable magnetic anomaly as pointed out by [19].

EM tracking systems use the the most suitable method for detecting buried cables [21]. Active and passive methods exist.

In an active measurement, a primary, time-varying EM field is transmitted from the device which induces eddy currents in a (ferro-)magnetic object depending on its geometry. The current flow creates a secondary, time-varying field which magnetic components are detected by the receivers of the system. The drawback of this method is that the field travels a longer distance since it goes back and forth and the received signal becomes small. Empirically valid, the received signal strength reduces by r^{-6} with the distance r to the object which limits the detection range to just over 2 m [22]. The market leading pulse induction cable and pipe tracking system is the TSS 440 by *Seatronics*.

Several passive EM cable detection systems exist where the source signal is created by the object itself. A signal of known frequency is induced into the cable at shore. The time-varying current creates a magnetic field which is detected by the tracker. Commonly, a block function signal is applied. A block function consists of a dominant frequency and its odd multiples. The block length depends on the dominant frequency. Cable detection can be based on one or multiple frequencies.

The passive EM methods works on all types of cables where a signal can be injected in: DC, AC and even fibre-optic cables. In case of an AC power cable, the operation frequency and its multiples can be used as a signal for detection. The operation frequency in Europe is 50 Hz.

An interesting cable detection project is the autonomous underwater vehicle Aqua Explorer 2 developed in cooperation by the KDD R&D Laboratories and Tokai University in Japan. However, after first launch of the project in 1997, only five cable-inspection missions were carried out [23]. This system is based on two 3-axis magnetometers. The cable position is determined by measuring the magnetic field vector at two locations and simple geometrical relations [24].

The measuring device manufacturer *Tinsley* developed the cable tracking system 5930 MK II for operation by a professional diver in shallow sea. This system detects the cable by measuring the magnetic field induced by a signal with a 3-axis magnetometer. The distance to the cable is determined based on the expected decay of the magnetic field. Due to the approach, the detection range is limited to 3 m [21].

A different approach is conducted by *Innovatum*. By installation, the cable is marked with a permanent magnetic signature. When the cable position needs to be determined, their cable tracking system *Smartrak* measures the magnetic signature and determines position including depth. In case of an unprepared cable, the same system is able to detect the cable based on an input tone [25].

Finally, model based inversion of the magnetic signal exists. Using an underlying model of the cable, its position is determined, often in an iterative manner. Systems that work based on this approach are the Orion by *Optimal Ranging* and the TSS 350 by *Seatronics*.
A number of different cable tracker systems were developed by [26]. The systems were tested on synthetic data. Field surveys on installed submarine cables were carried out but the prototypes were not sufficiently tested for a product. Several model based inversions, to some extent applying Neural Networks, were developed and tested by [26]. They did not give the satisfactory outcome. Even after adding a Kalman and an unscented Kalman filter algorithm to the inversion and using multiple sample points in contrast to inversion of a single point, the results were not satisfactory mainly due to the need of good prior knowledge of the survey environment. In a final approach, a Particle Filter algorithm was developed and tested which estimates a cable position accurately. This statistical method can detect a cable in a depth of 10 m which is a better detection range than existing systems. However, the sailing line of the sensors must be perpendicular to the cable direction. In other words, data from the same cable position but measured at different locations is required for a solution. Furthermore, the current in the signal needs to be known which is in general not the case in cable tracking surveys.
The described EM methods are based on time-varying signals produced by an injected tone or an AC power cable. Three methods which are based on the static magnetic field of a DC power cable are described by [27]. The methods were tested successfully on a sea trial and could detect the position of a sea cable from a distance of up to 4 m by a current of 1 A.

1-3 Statement of the problem

The location of submarine power cables is known with uncertainty after installation and, additionally, the position changes during their lifetime due to water and sediment movement, and other external influences. The exact location of the submarine cable is crucial for the operator for maintenance and a quick repair duration in case of failure. Since the cable should be buried, the depth is of interest. Different cable tracker systems are on the market for carrying out the task of detecting cables (c.f. Section 1-2-3). The available systems have either a small measuring range which makes them unsuitable for surveys without a professional diver or the detection accuracy is insufficient. The offshore cable industry has a demand for a cable tracking system of submarine power cables with high accuracy and large measuring range. Additionally, a simple handling is desired and the system should be adjustable for specific requirements of the survey.
In this report, we present a passive EM system for localization of the cable positions based on a known, injected signal (i.e. a tone). The signal in the cable creates a magnetic field which is detected by five 3-axis fluxgate magnetometers in a frame. The orientation of the frame is measured using a motion sensor. Model and geometrical based inversion schemes are developed allowing the cable position to be determined relative to the sensor array. A software package is created on top of existing hardware. No new hardware components are developed.
The inversion codes are tested on synthetic data. It is aimed for a system that determines the cable position up to a distance of 5 m, with an accuracy of ± 1 m in all three components. Additionally, the inversion codes and processing schemes should perform on real data. For

testing, a cable is setup on land and a measurement campaign is conducted which will proof the concept.

1-4 Description of the survey environment, set up and the object of detection

The survey domain is a shallow marine environment with conductive sea water. The water depth is less than 30 m. Above the sea level is air. The cable is buried in marine sediments in $0 - 2$ m depth.
Submarine power cables have a complex structure which is described in Section 1-2-2. In this report, it is assumed that the cable is a simple wire and the layers around the conductor are ignored. Furthermore, the width of the conductor is not taken into account because modern submarine power cables have a conductor's diameter of less than 0.1 m which is small compared to the offset distance between sensor and cable which is a few meter [28]. Additionally, it is assumed that the cable is not bent. This is a reasonable assumption in most cases. However, where the cable is connected to an offshore platform, for example a wind turbine, this assumption does not hold. We consider a cable which is mostly horizontally aligned but with degree of freedom in dip.
A block function signal is injected into the cable with known center frequency. The frequency can vary and depends on the survey set up but it will in general stay between $10 - 100$ Hz. Below 10 Hz, the number of samples per second is small which results in a slow survey speed since a certain number of samples per inversion is needed for noise reduction. With increasing frequency, attenuation of the EM field due to conductivity of sea water grows. The center frequency which is used in this study is 31 Hz which is a trade-off between samples per second and attenuation. Power lines in Europe are operated with 50 Hz. The frequency chosen is well below and therefore is not influenced by active cables close to the survey location. Additionally, the chosen frequency is a prime number and, therefore, it cannot be a multiple of a different signal.
The signal in the cable creates a magnetic field which is measured with five 3-axis fluxgate magnetometers in a rigid frame. The frame rotation is tracked with a motion sensor. The sensors can be dragged behind a survey vessel on a wing, or be mounted on an ROV. In a shallow survey environment, utilizing a wing is a more common choice. In very shallow water, hull mounting is common. The position of the sensor frame can be located with an Ultra Short Baseline (USBL). Using the S2C R 48/78 system by *Evo Logics* as example, accuracy of ± 0.2 m at 100 m distance between vessel and sensor frame can be achieved according to the manufacturer [29].

Chapter 2

Forward models of a line source

In this chapter, analytical and numerical methods are described for determining the magnetic field of a cable. Two analytical solutions of a line source are described. The first equation is for determining the magnetic field of a static line source and it is independent of the conductivity of the medium. The second analytical solution is for a non-static line source derived in frequency domain. The solution depends on the medium's conductivity. The numerical model derives the EM field in horizontal wavenumber-Laplace domain for a three-layered earth.

2-1 Analytical solutions

2-1-1 Static line source

The initial point for deriving the analytical solution of the magnetic field of a cable with a static current are the Maxwell's equations and in particular the Gauss' Law and Ampere's Law [30]:

$$\nabla \cdot \mathbf{B} = 0 \tag{2-1a}$$

$$\oint_C \mathbf{B} \cdot d\mathbf{l} = \iint_S \epsilon\mu \frac{\partial \mathbf{E}}{\partial t} \cdot d\mathbf{s} + \iint_S \mu \mathbf{J} \cdot d\mathbf{s} \tag{2-1b}$$

with the line integral over the closed path C and its line element $d\mathbf{l}$, the magnetic flux density $\mathbf{B}$, the electric field $\mathbf{E}$, permeability μ, permittivity ϵ and the current density $\mathbf{J}$. The double integral with surface element $d\mathbf{s}$ is evaluated over the surface S which is bounded by C. The first equation means that a magnetic charge does not exist. The second equation shows that a rotating magnetic field is created by a dynamic electric field and an electric current. The permittivity ϵ and permeability μ are physical properties which are defined as [31]:

$$\epsilon = \epsilon_r \epsilon_0 \tag{2-2a}$$

$$\mu = \mu_r \mu_0 \tag{2-2b}$$

with the permittivity in free-space $\epsilon_0 = 8.85 \times 10^{-12}\,\mathrm{F/m}$ and the permeability in free-space $\mu_0 = 4\pi \times 10^{-7}\,\mathrm{H/m}$ [32]. The relative permittivity is ϵ_r and the relative permeability is μ_r which are medium specific. By definition, they are both 1 in the free-space. For a steady, constant current I, Eq. (2-1a) and Eq. (2-1b) can be transformed to the Biot-Savart Law [33]:

$$\mathbf{B}(\mathbf{r}) = \frac{\mu_0 I}{4\pi} \oint_C \frac{d\mathbf{l} \times \mathbf{r}'}{|\mathbf{r}'|^3}, \tag{2-3}$$

with I is the current, $\mathbf{r}'$ is the displacement vector which is the vector from the line element $d\mathbf{l}$ at position $\mathbf{l}$ and the point of interest $\mathbf{r}$. The displacement vector is defined as: $\mathbf{r}' = \mathbf{r} - \mathbf{l}$. For a straight wire with infinite length, the total magnetic field can be derived using Eq. (2-3) in cylindrical coordinates (r, ϕ, z) with the z coordinate along the cable and the azimuth unit vector $\hat{\mathbf{e}}_\phi$ [31]:

$$\mathbf{B}(r, \phi, z) = \frac{\mu_0 I}{2\pi r} \hat{\mathbf{e}}_\phi. \tag{2-4}$$

Therefore, the total magnetic field is proportional to the current I, inversely proportional to distance r and it is invariant to the position along the cable. The direction of the field is rotational around the cable.

2-1-2 Non-static line source

The magnetic flux of a current carrying wire is derived in [34], [35] and [36] for a non-static line source. The solution for an infinite long cable is in cylindrical coordinates:

$$\mathbf{B}(r, \phi, z) = \frac{\mu \gamma I}{2\pi} K_1(\gamma r) \hat{\mathbf{e}}_\phi \tag{2-5}$$

where K_1 is the modified Bessel function of the second kind and order one, and γ denotes the propagation constant defined as:

$$\gamma = \sqrt{-\omega^2 \mu \epsilon + i \omega \mu \sigma} \tag{2-6}$$

with the electric conductivity σ of the medium and the angular frequency ω of the current in the cable. The resistivity ρ of the medium is defined as: $\rho = 1/\sigma$ and the temporal frequency f of the current as: $f = \omega/(2\pi)$. The low frequency simplification is valid for the case $\sigma >> \epsilon\omega$ and than Eq. (2-6) can be approximated as [37]:

$$\gamma = (i + 1)\sqrt{\omega \mu \sigma / 2}. \tag{2-7}$$

For the magnetostatic case of a DC source, the propagation constant goes to zero, in which limit Eq. (2-5) becomes Eq. (2-4).

2-2 Numerical model

The electromagnetic field of a line source can be derived numerically for a 1D layered earth. First, we derive an expression for the magnetic field produced by a line source in a homogeneous earth in horizontal wavenumber-Laplace domain. Afterwards, we give the solution for a three-layered earth consisting of an air half-space, a sea water layer and a soil half-space. The derivation are based on [38].

2-2-1 Homogeneous earth

A submarine power cable can be described as an electric line source $\mathbf{J}^e(\mathbf{x}, t)$. In Laplace domain, an electric line source $\hat{\mathbf{J}}^e$ parallel to $\hat{\mathbf{e}}_x$ is given as:

$$\hat{\mathbf{J}}^e(\mathbf{x}, s) = \hat{I}(s)\delta(z - c_z)\delta(y - c_y)\hat{\mathbf{e}}_x \tag{2-8}$$

with the signal $I(s)$ in Laplace domain, the Delta function $\delta(\cdot)$, the cable depth c_z and cable horizontal offset c_y. The Laplace transformation variable s can be real and positive or with $s = i\omega = i2\pi f$. A 1D medium is characterized by a horizontal shift-invariance and a 2D spatial Fourier transformation can be carried out, i.e., the horizontal components are given in wavenumber domain but the z-direction is spacial. The source is given in wavenumber-Laplace domain as:

$$\widetilde{\mathbf{J}}^e(k_x, k_y, z, s) = \hat{I}(s)\delta(k_x)\delta(z - c_z)\hat{\mathbf{e}}_x. \tag{2-9}$$

with the horizontal wavenumber k_x and k_y. We can conclude that an EM field is only for $k_x = 0$. The electric field at the receiver depth s_z, produced by the electric source, is given as [38]:

$$\widetilde{\mathbf{E}}(k_x = 0, k_y, z = s_z, s) = -\zeta\hat{I}(s)\widetilde{G}(s_z - c_z)\hat{\mathbf{e}}_x \tag{2-10}$$

with the scalar Greens function:

$$\widetilde{G}(s_z - c_z) = \frac{\exp(-\Gamma|s_z - c_z|)}{2\Gamma}. \tag{2-11}$$

The vertical wavenumber Γ is for $k_x = 0$:

$$\Gamma = \sqrt{k_y^2 + \gamma^2}, \tag{2-12}$$

where

$$\gamma = \sqrt{\zeta\eta}, \quad \eta = \sigma + s\epsilon \text{ and } \zeta = s\mu. \tag{2-13}$$

The magnetic field $\widetilde{\mathbf{H}} = (\widetilde{H}_x, \widetilde{H}_y, \widetilde{H}_z)^T$ is than [38]:

$$\widetilde{H}_x(k_x = 0, k_y, z = s_z, s) = 0 \tag{2-14}$$

$$\widetilde{H}_y(k_x = 0, k_y, z = s_z, s) = -\zeta^{-1}\partial_{s_z}\widetilde{E}_x = -\hat{I}\text{sign}(s_z - c_z)\frac{\exp\left(-\Gamma|s_z - c_z|\right)}{2} \tag{2-15}$$

$$\widetilde{H}_z(k_x = 0, k_y, z = s_z, s) = -ik_y\zeta^{-1}\widetilde{E}_x = \hat{I}\frac{ik_y\exp\left(-\Gamma|s_z - c_z|\right)}{2\Gamma} \tag{2-16}$$

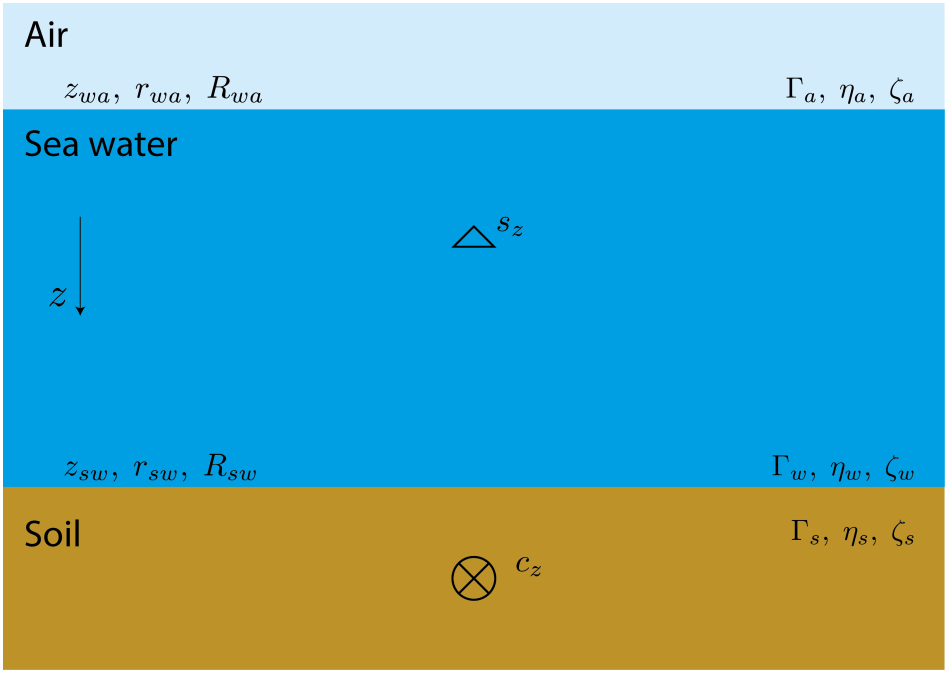

Figure 2-1: Schematic sketch of the three-layered earth model.

with the sign-function sign$(\cdot)$. The transformation of the magnetic field $\widetilde{\mathbf{H}}(k_x, k_y, s_z)$ in wavenumber-Laplace domain to the magnetic field $\hat{\mathbf{H}}(s_x, s_y, s_z)$ in space-Laplace domain at receiver position $(s_x, s_y, s_z)^T$ is defined as:

$$\hat{\mathbf{H}}(s_x, s_y, s_z, s) = \frac{1}{2\pi} \int_{k_y=-\infty}^{\infty} \widetilde{\mathbf{H}} \exp\left(-ik_y s_y\right) dk_y. \tag{2-17}$$

In the case of the magnetic field in a homogeneous domain (Eq. (2-14)-Eq. (2-16)), the integral expression of Eq. (2-17) has an analytical solution in the form:

$$\hat{H}_x(s_x, s_y, s_z, s) = 0 \tag{2-18}$$

$$\hat{H}_y(s_x, s_y, s_z, s) = -\text{sign}(s_z - c_z) \frac{(c_z - s_z)\gamma \hat{I}}{2\pi\sqrt{(s_y - c_y)^2 + (s_z - c_z)^2}} K_1(\gamma r) \tag{2-19}$$

$$\hat{H}_z(s_x, s_y, s_z, s) = \frac{(c_y - s_y)\gamma \hat{I}}{2\pi\sqrt{(s_y - c_y)^2 + (s_z - c_z)^2}} K_1(\gamma r), \tag{2-20}$$

which is the same results as Eq. (2-5) but in Cartesian coordinates and for the magnetic field. Eq. (2-5) gives the magnetic flux density of a line source in cylindrical coordinates. The magnetic flux density $\hat{\mathbf{B}}$ can be calculated from the magnetic field $\hat{\mathbf{H}}$ from:

$$\hat{\mathbf{B}} = \mu \hat{\mathbf{H}}. \tag{2-21}$$

2-2-2 1D three-layered earth

Based on the homogeneous solutions, a model for a 1D layered earth can be derived. We consider a specific configuration where the cable is buried in the soil of the sea. The receivers

are in the sea layer and on top of the sea is air. The soil layer and the sea layers are half-spaces. The layers have the properties of the conductivity function η_*, resistivivty function ζ_* and the vertical wavenumber Γ_*. The subscript $*$ is a for air, w for sea water and s for soil. The depth of the water-air layer is z_{wa} and of the soil-water layer z_{sw}. The depth of the receiver is s_z and of the cable c_z. A schematic sketch is shown in Figure 2-1.
The cable will create an EM field traveling upwards. At the soil-water boundary, a part will be transmitted and the other reflected. The reflected field travels downwards and does not contribute to the measurement. A local reflection coefficient r_{sw} at the soil-water boundary can be defined [38]:

$$r_{sw} = \frac{\Gamma_w - \Gamma_s}{\Gamma_w + \Gamma_s} \tag{2-22}$$

In water, the field has a direct path to the receiver and a path which travels to the water-air boundary, gets reflected and than travels downwards. The local reflection coefficient at this boundary is [38]:

$$r_{wa} = \frac{\Gamma_a - \Gamma_w}{\Gamma_a + \Gamma_w} \tag{2-23}$$

A global reflection coefficient includes the contribution of multiples, i.e. the field which is multiple times reflected at boundaries. The global reflection coefficient R_{sw} at the soil-water boundary an the global reflection coefficient R_{wa} at the water-air boundary are [38]:

$$R_{sw} = \frac{r_{sw} + R_{wa}\exp\left(-2\Gamma_w|z_{sw} - z_{wa}|\right)}{1 + r_{sw}R_{wa}\exp\left(-2\Gamma_w|w_{sw} - z_{wa}|\right)} \tag{2-24}$$

$$R_{wa} = r_{wa}. \tag{2-25}$$

The electric field $\widetilde{\mathbf{E}}_w(z = s_z)$ at a receiver depth s_z in the sea water layer, which is emitted by a line source in the soil half-space, has the form [38]:

$$\begin{aligned}\widetilde{\mathbf{E}}(z = s_z) = &-\hat{I}\zeta\widetilde{G}_s(z_{sw} - c_z)A_w^-(\exp(-\Gamma_w|s_z - z_{sw}|) \\ &+R_{wa}\exp(-\Gamma_w|z_{sw} + s_z - 2z_{wa}|))\hat{\mathbf{e}}_x,\end{aligned} \tag{2-26}$$

with the Greens function $\widetilde{G}_s(z_{sw} - c_z)$ in soil defined by Eq. (2-11) and the amplitude A_w^- of the up-going electric field which has the form [38]:

$$A_w^- = \frac{1 + R_{sw}}{1 + R_{wa}\exp\left(-2\Gamma_w|z_{sw} - z_{wa}|\right)}. \tag{2-27}$$

The magnetic field is than derived by Eq. (2-14)-(2-16):

$$\widetilde{H}_x(z = s_z) = 0 \tag{2-28}$$

$$\begin{aligned}\widetilde{H}_y(z = s_z) = &-\hat{I}\text{sign}(s_z - c_z)\Gamma_w\widetilde{G}_s(z_{sw} - c_z)A_w^- \\ &(\exp(-\Gamma_w|s_z - z_{sw}|) - R_{wa}\exp(-\Gamma_w|z_{sw} + s_z - 2z_{wa}|))\end{aligned} \tag{2-29}$$

$$\begin{aligned}\widetilde{H}_z(z = s_z) = &ik_y\hat{I}\widetilde{G}_s(z_{sw} - c_z)A_w^- \\ &(\exp(-\Gamma_w|z_{sw} - s_z|) + R_{wa}\exp(-\Gamma_w|z_{sw} + s_z - 2z_{wa}|)).\end{aligned} \tag{2-30}$$

The magnetic field in space-Laplace domain $\hat{\mathbf{H}}(s_x, s_y, s_z, s)$ can be calculated numerically with Eq. (2-17). The magnetic flux density is determined from the magnetic field with Eq. (2-21).

2-3 Comparison of the numerical model with analytical solutions

In the following, we compare different model domains and the influence on the measurement. We compare the analytical solution for a cable in air and in sea water with the numerical solution for a three layered earth. The magnetic permeability is in all layers μ_0, the permeability of vacuum. Air is non-conductive and we assign an arbitrary high resistivity of $\rho_a = 2 \times 10^{20}\,\Omega$m. We assume a resistivity for water of $\rho_w = 0.3\,\Omega$m and for soil of $\rho_s = 1\,\Omega$m, which are typical values for sea water and marine sediments [39]. The relative permittivity in air is approximated with the value for vacuum ($\epsilon_{r,a} = 1$). A typical relative permittivity for sea water is $\epsilon_{r,w} = 85$ and for soil of the seabed is $\epsilon_{r,s} = 23$ according to [40]. However, the low frequency approximation is taken and the permittivity is irrelevant. The cable is along the x-direction and, therefore, the magnetic field $B_x = 0\,$T. The tone in the cable has a strength of 0.1 A and a frequency of $f_s = 31\,$Hz. The solutions in air and in sea are derived by Eq. (2-5), the expression for a varying line source in a homogeneous space. The layered earth model assumes a buried cable in the seabed at a depth of 1 m. The water depth is 28 m. For different distances r diagonal to the cable, the solutions are compared. When the magnetic field is computed directly above the sea bottom, the horizontal and vertical offset to the cable is 1 m in this setup. The magnetic field B_x, By and the total field B_0 are shown in Figure 2-2a. Figure 2-2b shows the absolute difference between the solutions of sea water and of the layered model with the solution in air.
Due to the same distance in horizontal and vertical offset, B_y and B_z have same values for the homogeneous earth solutions. In the three-layer model, B_z shows a similar behaviour with distance as the homogeneous solution in sea water. With distance, the absolute difference between these solutions and the solution in air increases exponentially because of the exponential attenuation caused by conductivity. In sea water, the attenuation is greater than in the three-layer mode. This is caused by the average conductivity in homogeneous sea water which is higher than the average conductivity in the three-layer model because soil has a lower conductivity than sea water. The magnetic field B_y shows boundary effects which amplify the amplitude in water. In wavenumber-Laplace domain, the horizontal magnetic field is proportional to Γ_w, the vertical wavenumber in sea water, which is positive and intensifies the field (c.f. Eq. (2-29)). Additionally, B_y attenuates due to conductivity. Figure 2-2b suggests that at a distance of 14.5 m, both effects counter balance and beyond, the influence of water is more significant than boundary effects.

Figure 2-3 compares the solutions relative to frequency of the injected tone. The same setup as before is considered. The sensor is 3 m above the cable, i.e. 2 m above the sea floor, and the horizontal offset is 3 m. With increasing tone frequency, the influence of the earth structure and conductivity becomes more and more significant. For frequencies less than 40 Hz, the absolute difference between both models and the solution in air for all components is below 0.3 nT. The vertical field B_z is less influenced by boundary effects than B_y.

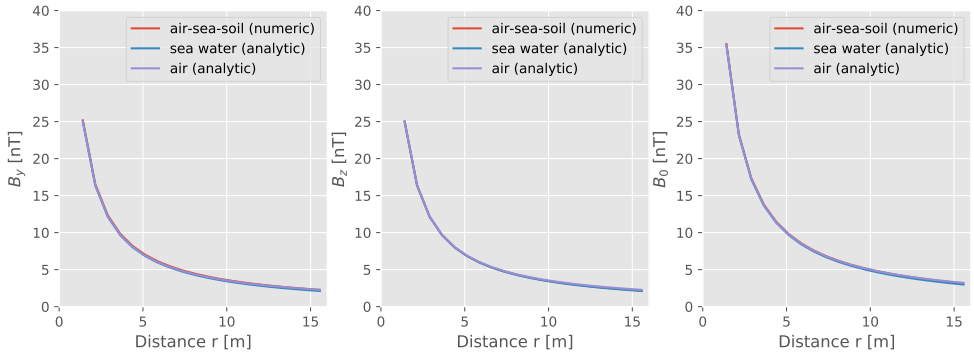

(a) Magnetic field measurements for air, sea water and the three-layer model.

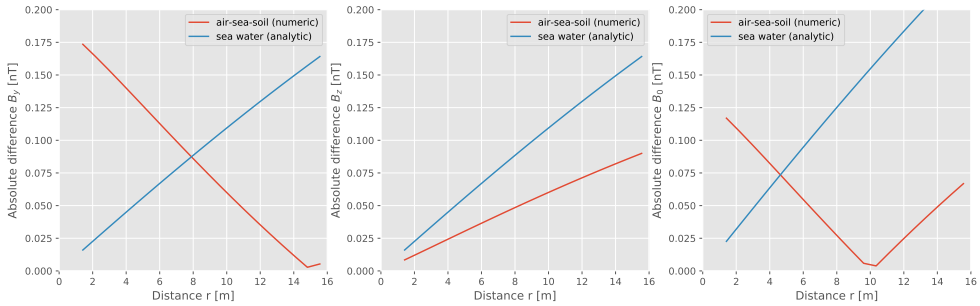

(b) Absolute difference between the solutions in sea water and the three-layer mode, and air.

Figure 2-2: Comparison of analytical solutions in air, sea water and the numerical three-layer model relative to distance between sensor and cable.

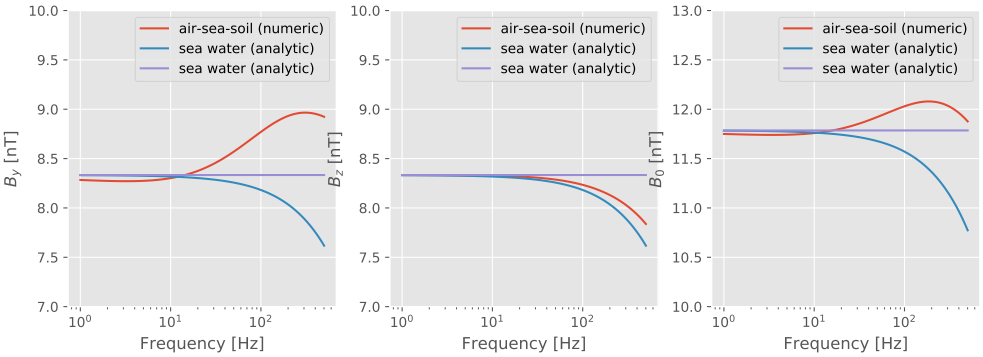

(a) Magnetic field measurements for air, sea water and the three-layer model.

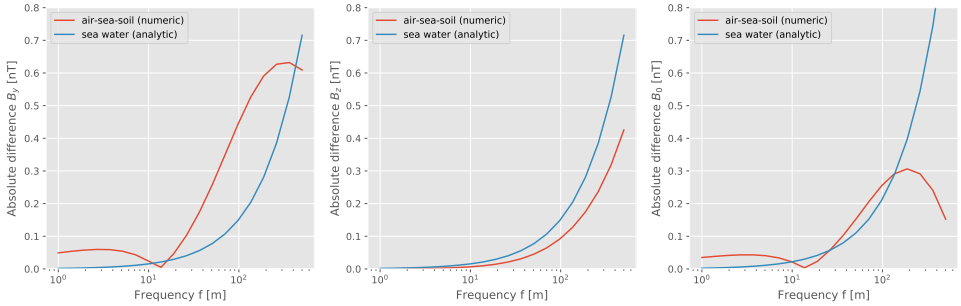

(b) Absolute difference between the solutions in sea water and the three-layer mode, and air.

Figure 2-3: Comparison of analytical solutions in air, sea water and the numerical three-layer model relative to source frequency.

Chapter 3

Theory of inversion algorithms

In this chapter, the theory of three different cable tracker systems (CTS I, CTS II and CTS III) is described. CTS I is model based and inverts the scalar total magnetic field $|\mathbf{B}|$. CTS II uses the vector $\mathbf{B}$ to determine the direction where the cable is located but inverts the distance similar to CTS I. CTS III finds the direction in the same way as CTS II, but calculates the final position via an intersection of lines.

3-1 Cable tracker system I

The total magnetic field of an infinite, static line source is given by Eq. (2-4). Each sensor with index $i = 1, 2, ..., n_s$ measures a local total magnetic field $|\mathbf{B}^i|$ and has an individual distance c_r^i to the cable. The sensors have a relative position $\mathbf{s}^i = (s_x^i, s_y^i, s_z^i)^T$, $i = 1, 2, ..., n_s$ to the center of the sensor array $\mathbf{s} = (s_x, s_y, s_z)^T$. The closest point on the cable from each individual sensor is denoted as $\mathbf{c}^i = (c_x^i, c_y^i, c_z^i)^T$. When the total sensor array length is small in comparison to the distance of the cable, we can approximate a cable position $\mathbf{c} = (c_x, c_y, c_z)^T$ relative to $\mathbf{s}$:

$$\mathbf{c} \approx \mathbf{c}^i, \quad i = 1, 2, ..., n_s \tag{3-1}$$

This assumption only holds for certain array setups. It depends on the relative position of the sensors to the cable and the sensor center. The separation between $\mathbf{c}$ and $\mathbf{c}^i$ can have a maximum distance of $|\mathbf{s}^i|$.
The approximated individual distance c_r^i between sensor and cable can be found with the Pythagorean theorem:

$$c_r^i \approx \sqrt{(s_x^i - s_x - c_x)^2 + (s_y^i - s_y - c_y)^2 + (s_z^i - s_z - c_z)^2}, \quad i = 1, 2, ..., n_s. \tag{3-2}$$

In combination with Eq. (2-4), a non-linear system of equations can be established:

$$\begin{cases} I\mu_0/(2\pi|\mathbf{B}^1|) - \sqrt{(s_x^1 - s_x - c_x)^2 + (s_y^1 - s_y - c_y)^2 + (s_z^1 - s_z - c_z)^2} & = 0 \\ I\mu_0/(2\pi|\mathbf{B}^2|) - \sqrt{(s_x^2 - s_x - c_x)^2 + (s_y^2 - s_y - c_y)^2 + (s_z^2 - s_z - c_z)^2} & = 0 \\ \vdots & \\ I\mu_0/(2\pi|\mathbf{B}^{n_s}|) - \sqrt{(s_x^{n_s} - s_x - c_x)^2 + (s_y^{n_s} - s_y - c_y)^2 + (s_z^{n_s} - s_z - c_z)^2} & = 0 \end{cases} \tag{3-3}$$

where the unknowns are c_x, c_y, c_z and I. The system of equations can be numerically solved by minimizing the least-squares residuals for each individual equation using the Levenberg-Marquardt algorithm. This algorithm is able to solve over-determined, non-linear systems of equations but has the disadvantage of only finding a local minimum which depends on an initial guess. If the initial guess is wrong, the final outcome may not be useful. A detailed description of the solver can be found in [41].

3-2 Cable tracker system II

In contrast to CTS I, CTS II does not look at scalar total field observations but rather at the vector of the magnetic field emanated by the cable. The initial coordinate system spanned by the unit vectors $\hat{\mathbf{e}}_x = (1,0,0)^T$, $\hat{\mathbf{e}}_y = (0,1,0)^T$ and $\hat{\mathbf{e}}_z = (0,0,1)^T$ can be transformed into a new coordinate system with basis $\hat{\mathbf{e}}'_x$, $\hat{\mathbf{e}}'_y$ and $\hat{\mathbf{e}}'_z$. The transformation parameters are chosen such that $\hat{\mathbf{e}}'_y$ is parallel to the cable.
At each sensor position $\mathbf{s}^i = (s_x^i, s_y^i, s_z^i)^T$, $i = 1, 2, ..., n_s$, the magnetic field vector $\mathbf{B}^i = (B_x^i, B_y^i, B_z^i)^T$ is measured. The magnetic field created by the source is circular around the cable and invariant along the cable. From this, it follows that the direction of the line source is perpendicular to every measured vector. Therefore, a vector which is perpendicular with respect to two non-collinar magnetic field vectors must be parallel to the line source.
The cable direction can be calculated for every possible sensor pair in the array via a cross product. The final direction is then averaged from the individual solutions:

$$\hat{\mathbf{e}}'_y = \frac{1}{\binom{n_s}{2}} \sum_{i=1}^{n_s} \sum_{j=i+1}^{n_s} \frac{\mathbf{B}^i \times \mathbf{B}^j}{|\mathbf{B}^i||\mathbf{B}^j|} \tag{3-4}$$

where $\binom{n_s}{2}$ is the binomial coefficient, which is required for averaging.
The unit vectors $\hat{\mathbf{e}}'_x$ and $\hat{\mathbf{e}}'_z$ can be chosen arbitrarily, as long as they are perpendicular to one another and to $\hat{\mathbf{e}}'_y$; a full basis is required which spans the new coordinate system. Calculating these two unit vectors can be done by first choosing an arbitrary unit vector (as long as it is not parallel to the cable), for example:

$$\hat{\mathbf{e}}_{random} = (0,0,-1)^T. \tag{3-5}$$

The other two vectors can be than calculated by:

$$\hat{\mathbf{e}}'_x = \hat{\mathbf{e}}'_y \times \hat{\mathbf{e}}_{random} \tag{3-6}$$

$$\hat{\mathbf{e}}'_z = \hat{\mathbf{e}}'_y \times \hat{\mathbf{e}}'_x. \tag{3-7}$$

In conclusion, three unit vectors $\hat{\mathbf{e}}'_x$, $\hat{\mathbf{e}}'_y$ and $\hat{\mathbf{e}}'_z$ spanning a Cartesian basis are derived. The vector $\hat{\mathbf{e}}'_y$ points along the cable.
Having derived the unit vectors of the new coordinate system, the 3×3 transformation matrix $\mathbf{T}$ can be established:

$$\mathbf{T} = \left(\hat{\mathbf{e}}'_x, \hat{\mathbf{e}}'_y, \hat{\mathbf{e}}'_z\right)^T. \tag{3-8}$$

Using the matrix $\mathbf{T}$, the sensor positions $\mathbf{s}^i$ and the field measurements $\mathbf{B}^i$ for each sensor i can be transformed:

$$\mathbf{s}^{i'} = \mathbf{T}^T \cdot \mathbf{s}^i, \quad \mathbf{B}^{i'} = \mathbf{T}^T \cdot \mathbf{B}^i, \quad i = 1, 2, ..., n_s, \tag{3-9}$$

where $\mathbf{s}^{i'} = (s_x^{i'}, s_y^{i'}, s_z^{i'})^T$ and $\mathbf{B}^{i'} = (B_x^{i'}, B_y^{i'}, B_z^{i'})^T$ denote vectors in the new system. The change in coordinate system has multiple advantages. Since the magnetic field is circular around the cable and is invariant along the cable, this leads to $B_y^{i'} = 0$. The sensor position $\mathbf{s}^{i'}$ can be shifted along the cable axis without changing the measurement. When $s_y^{i'}$ is set to zero, all sensors have the same reference point on the cable:

$$\widetilde{\mathbf{s}}^{i'} = (s_x^{i'}, 0, s_z^{i'})^T, \quad i = 1, 2, ..., n_s. \tag{3-10}$$

The initial 3D problem is reduced to 2D. The cable position $\mathbf{c}$ is now estimated in the new coordinate system and can be written as $\mathbf{c}' = (c'_x, c'_y, c'_z)^T$. An intermediate step is necessary where the relative cable position $\mathbf{c}^{i'}$ to each sensor is defined in cylindrical and Cartesian coordinates:

$$[\mathbf{c}^{i'}]_{cyl} = (c_r^{i'}, c_\theta^{i'}, c_y^{i'})^T, \tag{3-11}$$

$$\mathbf{c}^{i'} = = (c_x^{i'}, c_y^{i'}, c_z^{i'})^T = c_r^{i'} \cdot (\cos c_\theta^{i'}, 0, \sin c_\theta^{i'})^T, \quad i = 1, 2, ..., n_s. \tag{3-12}$$

where $c_y^{i'}$ is the axial coordinate which has the direction of $\hat{\mathbf{e}}'_y$. Due to the invariance of the system, we choose $c_y^{i'} = 0$ in accordance to Eq. (3-10). Using vector algebra we find the relation between $|\mathbf{c}'|$, $\widetilde{\mathbf{s}}^{i'}$ and $\mathbf{c}^{i'}$:

$$|\mathbf{c}'|^2 = |\widetilde{\mathbf{s}}^{i'}|^2 + |\mathbf{c}^{i'}|^2 + 2(\widetilde{\mathbf{s}}^{i'} \cdot \mathbf{c}^{i'}), \quad i = 1, 2, ..., n_s, \tag{3-13}$$

where $\widetilde{\mathbf{s}}^{i'}$ is known, and $\mathbf{c}^{i'}$ is determined using Eq. (3-12) with the individual azimuth angle $c_\theta^{i'}$ calculated by:

$$c_\theta^{i'} = \arccos \frac{\mathbf{B}^{i'} \cdot \hat{\mathbf{e}}'_z}{|\mathbf{B}^{i'}|}, \quad i = 1, 2, ..., n_s. \tag{3-14}$$

The individual cable distance $c_r^{i'}$ is determined from Eq. (2-4), the equation for a static line source:

$$c_r^{i'} = \frac{\mu_0 I}{2\pi |\mathbf{B}^{i'}|}, \quad i = 1, 2, ..., n_s. \tag{3-15}$$

The current I is unknown here. Using Eq. (3-12)-(3-15), a system of equations can be set up with I and $|\mathbf{c}'|$ as unknowns:

$$\begin{cases} 0 &= |\widetilde{\mathbf{s}}^{1'}|^2 + \left(\frac{\mu_0 I}{2\pi|\mathbf{B}^{1'}|}\right)^2 - \frac{\mu_0 I}{\pi|\mathbf{B}^{1'}|}\left(\widetilde{\mathbf{s}}^{1'} \cdot (\cos c_\theta^{1'}, 0, \sin c_\theta^{1'})^T\right) - |\mathbf{c}'|^2 \\ 0 &= |\widetilde{\mathbf{s}}^{2'}|^2 + \left(\frac{\mu_0 I}{2\pi|\mathbf{B}^{2'}|}\right)^2 - \frac{\mu_0 I}{\pi|\mathbf{B}^{2'}|}\left(\widetilde{\mathbf{s}}^{2'} \cdot (\cos c_\theta^{2'}, 0, \sin c_\theta^{2'})^T\right) - |\mathbf{c}'|^2 \\ &\vdots \\ 0 &= |\widetilde{\mathbf{s}}^{n'_s}|^2 + \left(\frac{\mu_0 I}{2\pi|\mathbf{B}^{n'_s}|}\right)^2 - \frac{\mu_0 I}{\pi|\mathbf{B}^{n'_s}|}\left(\widetilde{\mathbf{s}}^{n'_s} \cdot (\cos c_\theta^{n'_s}, 0, \sin c_\theta^{n'_s})^T\right) - |\mathbf{c}'|^2. \end{cases} \tag{3-16}$$

The system of equations is again solved by minimizing the residual least-squares using the Levenberg-Marquardt algorithm. With the current I, the relative cable position $\mathbf{c}^{i'}$ to each sensor can be calculated with respect to e'_x, e'_y and e'_z from Eq. (3-12). With the known sensor position $\widetilde{\mathbf{s}}^{i'}$, the cable position relative to the array center can be calculated. Averaging over all sensors, the cable position $\mathbf{c}'$ is given by:

$$\mathbf{c}' = \frac{1}{n_s}\sum_{j=1}^{n_s}(\widetilde{\mathbf{s}}^{j'} + \mathbf{c}^{j'}). \tag{3-17}$$

The cable position in the initial coordinate system is calculated from:

$$\mathbf{c} = \mathbf{T}\cdot\mathbf{c}' + \mathbf{s} \tag{3-18}$$

with $\mathbf{s}$ as the center of the sensor array. CTS II requires a minimum of two measurements for inverting the cable position.

3-3 Cable tracker system III

CTS III finds the position of the cable from intersecting lines. In accordance to Section 3-2, the sensor positions $\mathbf{s}^i$ and the measurements $\mathbf{B}^i$ are transformed via the transformation matrix $\mathbf{T}$ into a new coordinate system in which they are written as $\mathbf{s}^{i'}$ and $\mathbf{B}^{i'}$ using Eq. (3-9). This system is characterized by the unit vector $\hat{\mathbf{e}}'_y$ which is parallel to the cable. The unit vectors $\hat{\mathbf{e}}'_x$ and $\hat{\mathbf{e}}'_z$ are orthogonal to another and to $\hat{\mathbf{e}}'_y$. The sensors can be shifted along the cable until they have the same reference point on the cable and the new sensor positions are denoted as $\widetilde{\mathbf{s}}^{i'}$. The position of the cable $\mathbf{c}^{i'}$ in reference to each individual sensor position can be determined by Eq. (3-12). In this approach, the direction of the individual sensor positions $\hat{\mathbf{c}}^{i'}$ is sufficient, which is:

$$\hat{\mathbf{c}}^{i'} = (\cos c_\theta^{i'}, 0, \sin c_\theta^{i'})^T, \quad i = 1, 2, ..., n_s. \tag{3-19}$$

The individual azimuth angles $c_\theta^{i'}$ are determined with Eq. (3-14). This equation only depends on the transformed magnetic vectors $\mathbf{B}^{i'}$ which are measured. The location of the cable $\mathbf{c}'$ in the transformed coordinate system is determined by finding the intersection of lines $\mathbf{l}^i$, $i = 1, 2, ..., n_s$. A line $\mathbf{l}^i$ is defined by [42]:

$$\mathbf{l}^i = \widetilde{\mathbf{s}}^{j'} + t\hat{\mathbf{c}}^{j'}, \quad -\infty < t < \infty, \quad i = 1, 2, ..., n_s. \tag{3-20}$$

In the distortion free case, $\mathbf{l}^i$ intersects with the true cable position $\mathbf{c}'$. When the line is not intersecting with the cable position (for example due to noise), a squared perpendicular distance $D(\mathbf{c}'; \widetilde{\mathbf{s}}^{i'}, \hat{\mathbf{c}}^{i'})$ can be derived which describes the shortest distance between the line $\mathbf{l}^i$ and the true cable position $\mathbf{c}'$. It is of the form [42]:

$$D(\mathbf{c}'; \widetilde{\mathbf{s}}^{i'}, \hat{\mathbf{c}}^{i'}) = (\widetilde{\mathbf{s}}^{i'} - \mathbf{c}')^T \cdot (\mathbf{I} - \hat{\mathbf{c}}^{i'} \cdot \hat{\mathbf{c}}^{i'T}) \cdot (\widetilde{\mathbf{s}}^{i'} - \mathbf{c}'), \quad i = 1, 2, ..., n_s \tag{3-21}$$

where $\mathbf{I}$ is the 3×3 unity matrix. A total squared distance function $D(\mathbf{c}')$ sums over all $D(\mathbf{c}'; \widetilde{\mathbf{s}}^{i'}, \hat{\mathbf{c}}^{i'})$ [42]:

$$D(\mathbf{c}') = \sum_{j=1}^{n_s} D(\mathbf{c}'; \widetilde{\mathbf{s}}^{j'}, \hat{\mathbf{c}}^{j'}). \tag{3-22}$$

The cable position $\mathbf{c}'$ is unknown, however, we assume that the cable is at the location where the total squared distance function is minimal. Minimizing Eq. (3-22) involves differentiating the equation regarding to $\mathbf{c}'$ and set it equal to zero [42]:

$$\frac{dD(\mathbf{c}')}{d\mathbf{c}'} = 2\sum_{j=1}^{n_s}\left(\mathbf{I} - \hat{\mathbf{c}}^{j'} \cdot \hat{\mathbf{c}}^{j'T}\right)\mathbf{c}' - 2\sum_{j=1}^{n_s}\left(\mathbf{I} - \hat{\mathbf{c}}^{j'} \cdot \hat{\mathbf{c}}^{j'T}\right) \cdot \widetilde{\mathbf{s}}^{j'} = 0. \tag{3-23}$$

This equation can be written as a linear system of equations of the form [42]:

$$\mathbf{R} \cdot \mathbf{c}' = \mathbf{q} \tag{3-24}$$

with:

$$\mathbf{R} = \sum_{j=1}^{n_s}\left(\mathbf{I} - \hat{\mathbf{c}}^{j'} \cdot \hat{\mathbf{c}}^{j'T}\right) \tag{3-25}$$

$$\mathbf{q} = \sum_{j=1}^{n_s}\left(\mathbf{I} - \hat{\mathbf{c}}^{j'} \cdot \hat{\mathbf{c}}^{j'T}\right) \cdot \widetilde{\mathbf{s}}^{j'}. \tag{3-26}$$

The matrix $\mathbf{R}$ is 3×3 and $\mathbf{q}$ is a 3×1 vector. This system of equations has as many unknowns as equations. Using a solver for a linear matrix equation, like the *gesv* routine, gives the solution $\mathbf{c}'$ of Eq. (3-24). The cable position $\mathbf{c}$ in the initial coordinate system is derived from the solution in the transformed coordinate system $\mathbf{c}'$ and Eq. (3-18).

Chapter 4

Analyses of synthetic data

4-1 Convergence and array studies

In this chapter, the performance of cable trackers CTS I, CTS II and CTS III are tested on synthetic data with the aim to study their convergence behavior. Additionally, the influence of different sensor arrays on the accuracy of the tracked cable location is accessed. Four different cable setups (C1, C2, C3, C4) are considered which are shown in Figure 4-1. All setups work on the premise of a homogeneous domain of resistiviy $\rho = 0.3\,\Omega$m, a typical value for shallow sea water [39]. In C1, the cable is parallel to the x-axis, with an offset of 3 m in y-direction and in 2 m depth (i.e. z-direction). In C2, the cable is positioned in the same depth but rotated in the horizontal plane by 45°. The distance between the cable and the sensor array is similar to C1. In setup C3, the cable runs parallel to the y-axis, with offsets similar to C1. C4 considers a cable which has the same distance to the center of the CTS as the other three setups. The heading direction of the cable is same as C2, however, it is positioned directly below the center. More information about C1, C2, C3 and C4 is listed in Table 4-1.

Six different arrays consisting of five sensors are tested with a sensor center $\mathbf{s} = (0, 0, 0)$m. The sensor coordinates in reference to the CTS center $\mathbf{s}$ are itemized in Table 4-2 and graphed in Figure 4-2. The chosen arrays are not symmetric in every direction and as a result have a directional susceptibility. The setups are selected in such a manner that they extend in y-

Parameters	C1	C2	C3	C4
$(c_x[\text{m}], c_y[\text{m}], c_z[\text{m}])$	(0,3,2)	(2.12,2.12,2)	(3,0,2)	(0,0,3.6)
f_s[Hz]	31	31	31	31
I[A]	0.1	0.1	0.1	0.1
ρ[Ωm]	0.3	0.3	0.3	0.3
n_s	5	5	5	5

Table 4-1: Parameters of cable setup C1, C2, C3 and C4.

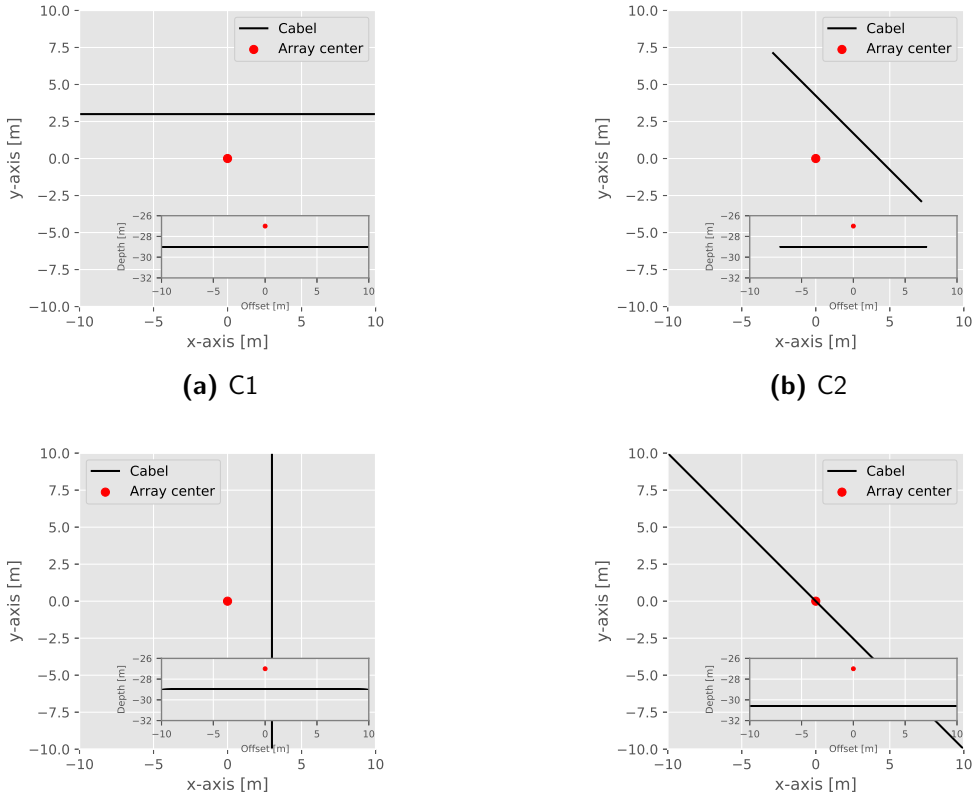

(a) C1 **(b)** C2

(c) C3 **(d)** C4

Figure 4-1: This figure shows four different cable setups (C1, C2, C3 and C4) and the center of the sensor array.

	$\mathbf{s}^1$[m]	$\mathbf{s}^2$[m]	$\mathbf{s}^3$[m]	$\mathbf{s}^4$[m]	$\mathbf{s}^5$[m]
Array 1	(0, 1, 0)	(0, 0.5, 0)	(0, 0, -0.5)	(0, -0.5, 0)	(0, -1, 0)
Array 2	(-0.25, 0.25, 0)	(-0.25, -0.25, 0)	(0, 0, 0.25)	(0, 0, -0.25)	(0.25, 0, 0)
Array 3	(0, 0, 0)	(0, 0.25, 0.25)	(0, 0.25, -0.25)	(0, -0.25, 0.25)	(0, -0.25, -0.25)
Array 4	(0.25, 0, 0)	(-0,25, 0.25, 0.25)	(-0.25, 0.25, -0.25)	(-0.25, -0.25, 0.25)	(-0.25, -0.25, -0.25)
Array 5	(0, 0, 0)	(0, 0.25, 0)	(0, 0.5, 0)	(0, -0.25, 0)	(0, -0.5, 0)
Array 6	(0, 0, 0)	(0, 0, 0.25)	(0, 0, 0.5)	(0, 0, -0.25)	(0, 0, -0.5)

Table 4-2: Sensor positions of Array 1-6.

	Start	End	Number steps
$c_{x,0}$	$-10\,\mathrm{m}$	$10\,\mathrm{m}$	5
$c_{y,0}$	$-10\,\mathrm{m}$	$10\,\mathrm{m}$	5
$c_{z,0}$	$0\,\mathrm{m}$	$60\,\mathrm{m}$	5
I_0	$0\,\mathrm{A}$	$2\,\mathrm{A}$	10

Table 4-3: Parameters for the grid search of initial guesses defined by the start and end values of each variable and the number of intermediate steps. In total, 1250 different initial values are tested.

and z-direction rather than in x-direction. The reason for this choice is that the sensitivity of a cable tracker system does not need to be the same in all directions. In general, prior knowledge about the location of the cable after installation exists. A survey can be designed in such a way that the vessel is sailing roughly along the cable. Therefore, the tracking system should be more sensitive to depth and offset than in the direction along the sailing line. The cable setups are chosen in a way that the influence of sensor array's geometries can be tested.

4-1-1 Cable tracker system I

Synthetic data is created for every array-cable-combination. Then, the inversion is applied multiple times with different initial guesses for the location $(c_{x,0}, c_{y,0}, c_{z,0})$ and current I_0 to study their influence on the estimated parameters and the convergence behaviour. The initial guesses are chosen systematically from a grid search. Detailed information about the grid search is displayed in Table 4-3. The solutions are shown in Table A-1 - A-4 of Appendix A-1. Which array is able to get the position of the specific cable setup is shown in Table 4-4. The table shows that some arrays perform superior and that some cable setups are more detectable than others. Array 2 and Array 4 detect all cable setups, because the sensors have a three dimensional layout. Array 5 and Array 6 are lines of sensors. These arrays are not able to properly detect any cable setup. It can be concluded that this inversion methods benefits from a sensor array which is spherical- or cubical-like. This behaviour might be caused by the assumption taken for CTS I. The relative cable position of each sensor is approximated as similar to the cable position relative to the sensor center. In general the system is well able to achieve a successful convergence.

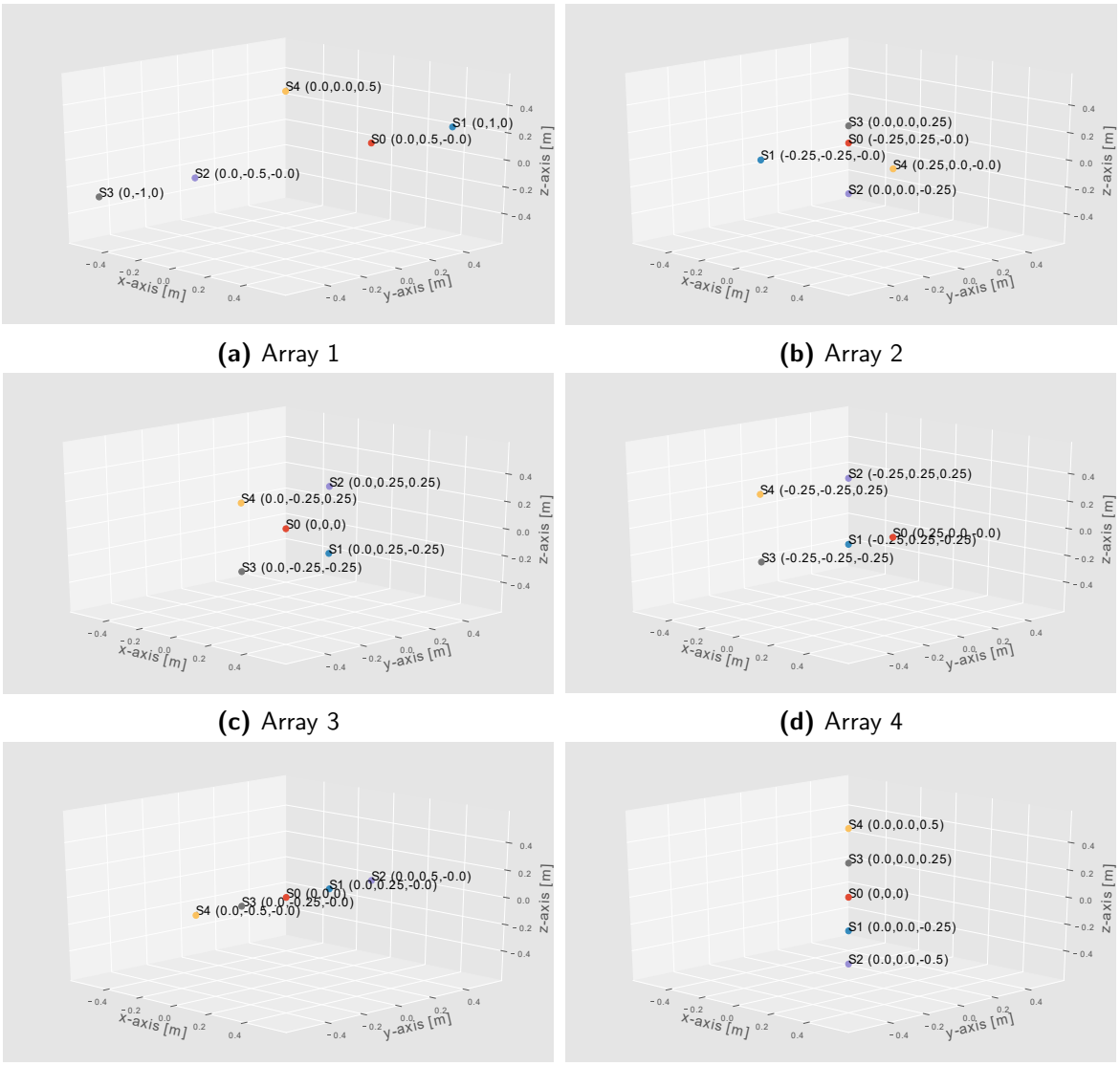

(a) Array 1 **(b)** Array 2

(c) Array 3 **(d)** Array 4

(e) Array 5 **(f)** Array 6

Figure 4-2: An array setup consist of five sensors $S_0, S_1, ..., S_4$ which are distributed in space. Six different array configurations are shown. Each sensor has its relative coordinates respect to the the array center at $(0, 0, 0)$

	C1	C2	C3	C4
Array 1	x			x
Array 2	x	x	x	x
Array 3	x			x
Array 4	x	x	x	x
Array 5				
Array 6				

Table 4-4: Capability of CTS I to detect different cable setups with a particular sensor array.

	C1	C2	C3	C4
Array 1	x	x	x	
Array 2	x	x	x	x
Array 3	x	x	x	x
Array 4	x	x	x	x
Array 5	x	x		
Array 6	x	x	x	x

Table 4-5: Capability of CTS II to detect different cable setups with a particular sensor array.

	C1	C2	C3	C4
Array 1	x	x	x	x
Array 2	x	x	x	x
Array 3	x	x	x	x
Array 4	x	x	x	x
Array 5	x	x		x
Array 6	x	x	x	

Table 4-6: Capability of CTS III to detect different cable setups with a particular sensor array.

4-1-2 Cable tracker system II

In the same manner as for CTS I, the performance of CTS II is assessed on synthetic data. Its convergence behavior is studied and possible sensor arrays are tested. The same cable setups C1, C2, C3 and C4 (c.f. Figure 4-1 and Table 4-1) and the same arrays (c.f. Table 4-2 and Figure 4-2) are considered as in Section 4-1-1. The inversion results of each cable sensor array pair is shown in Table A-5 - A-8 of Appendix A-1. Table 4-5 summarizes which array type can invert which cable setup. In general, all array types perform well. However, Array 6 cannot detect C3 because of the symmetry of the cable. All sensors measure the same magnetic field vector. Cable C4 cannot be detected by Array 1 and Array 5. The solutions of all sensor arrays are stable except for an initial current of $I_0 = 0\,\mathrm{A}$, when the wrong solution is found.

4-1-3 Cable tracker system III

In this section, the results of CTS III is analysed. Since this method relies on inverting a linear system which has as many unknowns as equations, only one solution exists (if one exists) and a convergence study is not required. Table A-9 - A-12 in Appendix A-1 shows the result of inverting the cable position C1-C4 with the individual sensor arrays. Table 4-6 shows which cable setup can be detected by which array. The cable position can be always determined except if all sensors have the same directional vector $\hat{\mathbf{c}}^i$. In those cases, an intersection of lines cannot be found. This is the case for Array 5 with C3 and Array 6 with C4.

4-2 Performance in noise disturbed domain

4-2-1 The noise disturbed domain

In the previous section, the convergence behaviour and possible sensor arrays have been evaluated. This section analysis the systems in a noise disturbed area. The model domain is sea water which has a resistivity of $\rho_w = 0.3\,\Omega$m and a relative permeability of $\mu_{r,w} = 1$. The data are modeled with the analytical solution of a varying line source (c.f. Eq. (2-5)) which is parallel to $\hat{\mathbf{e}}_x$, i.e. cable setup C1 is considered.
The signal in the cable has a frequency of 31 Hz and a strength of 0.25 A. We only look at sensor arrays which work with the respective CTS. CTS I is tested with Array 2 and Array 4 since these are the only arrays which are able to determine the location of all four cable setups. CTS II and CTS III are tested with Array 5 and Array 6 because of their simplicity and the ease of handling when mounted on survey platforms.
Different error and noise sources will disturb the data. In this study, these statistical terms are added to the magnetic channels after modeling. The earth magnetic field in the extremely low frequency band is below 0.1 nT [43]. Artificial noise, which can be caused by the operational vessel, will disturb the measurement. After analysing magnetic data measured from an offshore survey by Sensys with the FGM3D/100 sensor in the Baltic sea, the ambient noise is estimated with a standard deviation of 0.1 nT in 31 Hz. This value is subsequently applied on all sensors and directions individually. Additionally, the sensors have a relative error of $\pm 0.1\%$ according to [44]. After mounting the frame, the sensors will have an assumed positioning error of standard deviation 2.5 mm. During surveying, the sensor frame can tilt. We assume that the array is dipped by an unknown angle of standard deviation 1° which is the accuracy of a typical motion sensor like the ISA500 by *Impact Subsea* [45].
Since the error terms are random, this experiment is conducted multiple times (3000 iterations). The distributions are shown in Figure A-1-A-6 in Appendix A-2. The standard deviation σ and the mean μ from the distributions are summarized in Table 4-7 for each CTS and array.
Figure A-1-A-6 shows that the error terms are normally distributed. Therefore, it is reasonable to describe the performance of the systems in terms of mean and standard deviation. The CTSs with the associated sensor arrays have in average an inversion error which is smaller than 0.05 m. The standard deviation of the inversion is below 0.3 m. The only exception is CTS III with Array 5. This combination has a mean inversion error of 0.09 m for c_y and c_z.

4-2-2 Distance study

CTS I, CTS II and CTS III are tested for different horizontal and vertical offsets in the same environment as described previously, i.e. sea water with noise. The offset and cable depth is analyzed in $0 - 8$ m and the domain is discretized by 16×16 cells. In a setup where the cable is parallel to the x-axis, the vertical offset corresponds to a changing depth of the cable c_z and the horizontal offset to a changing c_y. A similar analysis is carried out for rotated arrays which have a different azimuth to the cable.

	Array	c_x [m]		c_y [m]		c_z [m]		I [A]	
		μ	σ	μ	σ	μ	σ	μ	σ
CTS 1	2	0.00	0.24	2.99	0.28	1.99	0.28	0.25	0.02
CTS 1	4	0.01	0.22	3.01	0.20	2.00	0.20	0.25	0.01
CTS 2	5	0.00	0.12	3.02	0.14	1.98	0.08	0.25	0.01
CTS 2	6	0.00	0.16	2.96	0.19	1.95	0.13	0.25	0.02
CTS 3	5	0.00	0.11	2.91	0.19	1.91	0.16	-	-
CTS 3	6	0.00	0.17	3.06	0.13	2.01	0.11	-	-
	True	0.00	-	3.00	-	2.00	-	0.25	-

Table 4-7: Performance of CTSs in detecting C1 in sea water with noise which is evaluated in terms of mean μ and standard deviation σ. The inherent histograms are Figure A-1-A-6 which are shown in Appendix A-2.

Cable tracker system I

CTS I is tested with Array 2 and 4. The results for C1 with an azimuth angle of 0° between cable and sensor frame are shown in Figure 4-3 and Figure 4-4. The figures show the absolute error between the mean inversion result and the true location and the standard deviation. Since both arrays have a 3D structure, their results are similar. The x-coordinate of the cable position c_x is inverted well in terms of the mean solution. However, this coordinate is not changing for different horizontal or vertical offsets in C1. In terms of mean, c_y and c_z have an absolute error of less than 1 m in a radius of 6 m around the cable. However, the standard deviation exceeds more than 1 m for a radius larger than 5 m in all three coordinate components.
Array 2 and 4 are also tested for different azimuth angels between cable and sensor frame. The results are shown in Figure A-7 - A-12 of Appendix A-2. The results show that the influence of different azimuth angles is small. The reason for this is that Array 2 and 4 are extending in all three spacial directions equally.

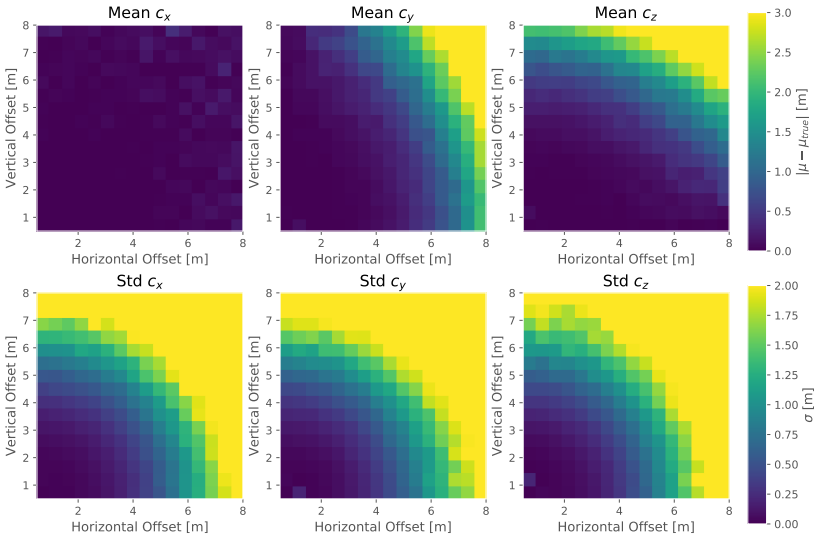

Figure 4-3: Inversion results of CTS I and Array 2 in noise disturbed sea water for different sensor positions to the cable. The first row displays the absolute error between the mean estimation and the true value. The second row shows the associated standard deviation.

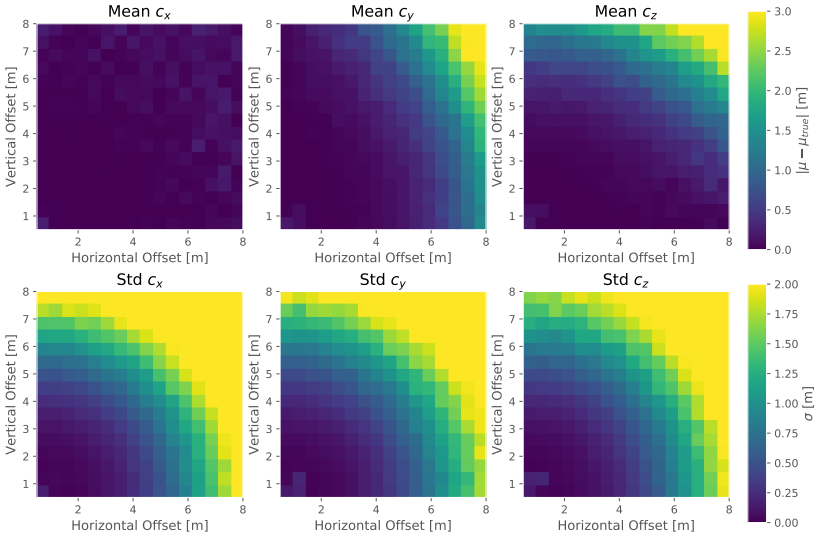

Figure 4-4: Inversion results of CTS I with Array 4 in noise disturbed sea water for different sensor array positions. The first row displays the absolute error between the mean estimation and the true position. The second row shows the associated standard deviation.

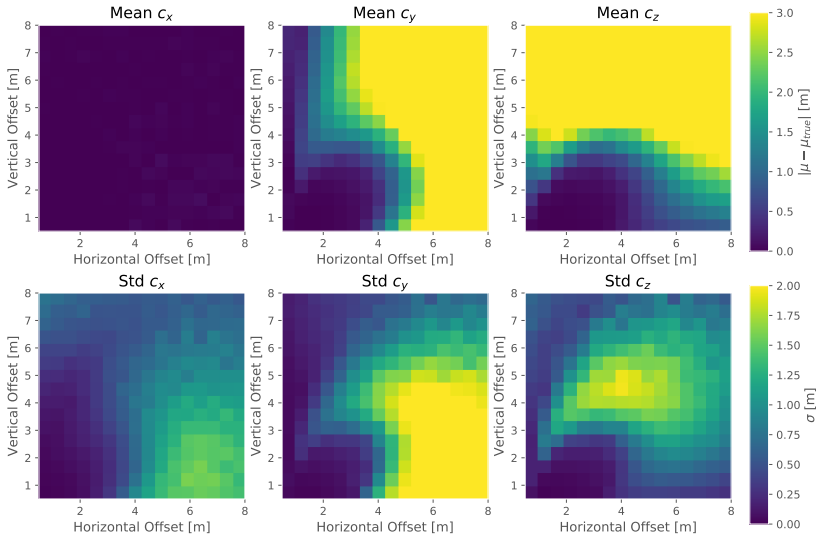

Figure 4-5: Inversion results of CTS II and Array 5 in noise disturbed sea water for different sensor positions to the cable. The first row displays the absolute error between the mean estimation and the true position. The second row shows the associated standard deviation.

Cable tracker system II

The results from CTS II with Array 5 are shown in Figure 4-5. The cable position c_x is well estimated. The mean absolute error is below 0.5 m and the standard deviation below 0.25 m. Beyond a radius of 4 m, the estimated c_y has an absolute error of more than 1.5 m. Inside this radius, the standard deviation of the inversion is below 0.75 m. The depth c_z is well estimated for vertical offsets less than 5 m with the standard deviation not exceeding 1 m.
The inversion results with Array 5 change for different azimuth angle between cable and sensor frame. Figure A-13 - A-15 in Appendix A-2 show the influence for different azimuth angles between Array 5 and the cable. Noticeable is that the area where the inversion succeeds is not changing shape but only becomes smaller. For azimuth angles below 22.5°, the loss of accuracy is insignificant. The results for CTS II with Array 6 are shown in Figure A-16 in Appendix A-2. Due to the symmetry of Array 5 and 6, the results are just rotated and interchanged between c_y and c_z. The benefits of using Array 6 is that it is independent of the azimuth angle between sensor frame and cable.

Cable tracker system III

CTS III is tested with Array 5. The results are shown in Figure 4-6. The average cable position of c_x is well estimated. However, for distances larger than 4 m, the standard deviation is increasing to more than 1 m. The estimation of component c_y and c_z stays especially good for increasing vertical offset. For horizontal offset larger than 5 m, the accuracy of determining c_y and c_z is decreasing rapidly.

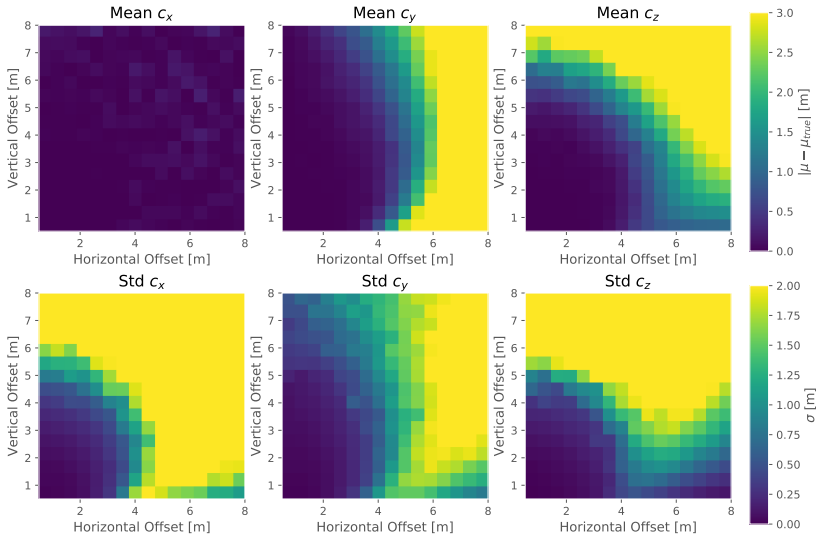

Figure 4-6: Inversion results of CTS III and Array 5 in noise disturbed sea water for different sensor positions to the cable. The first row displays the absolute error between the mean estimation and the true position. The second row shows the associated standard deviation.

The performance of Array 5 depends on the azimuth between cable and sensor frame. The results for different azimuth angles is shown in Figure A-17 - A-19 in Appendix A-2. For increasing azimuth angles, the detecting range is decreasing. For azimuth angels less than 45°, the inversion outcomes are almost unchanged. The results of CTS III with Array 6 are shown in Figure A-20. The findings are similar to Figure 4-6, which shows the results of CTS II with Array 5, but rotated and interchanged for c_y and c_z.

4-2-3 Influence of sensor separation

In the previous sections, different array configurations are tested where the separation distance between the sensors is 0.25 m. In this section, CTS I, CTS II and CTS III are tested for different sensor separations. The same sensor arrays as in the previous section are considered. The model domain is sea water with noise. The cable setup is C1. The results are shown in Figure 4-7. Separation distances of below 0.4 m negatively influences the inversion accuracy for all CTSs and Arrays, whereby the mean estimation deviates from the true solution and the standard deviation increases. When the sensor separation distances is more than 0.4 m, however, the inversion results do not get more accurate. Neither the mean estimation nor the standard deviation significantly improves.

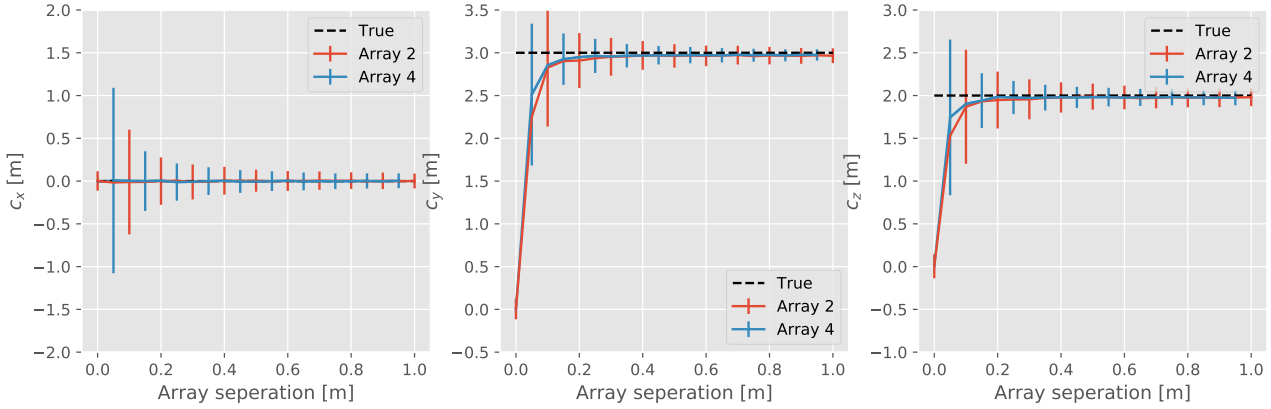

(a) CTS I

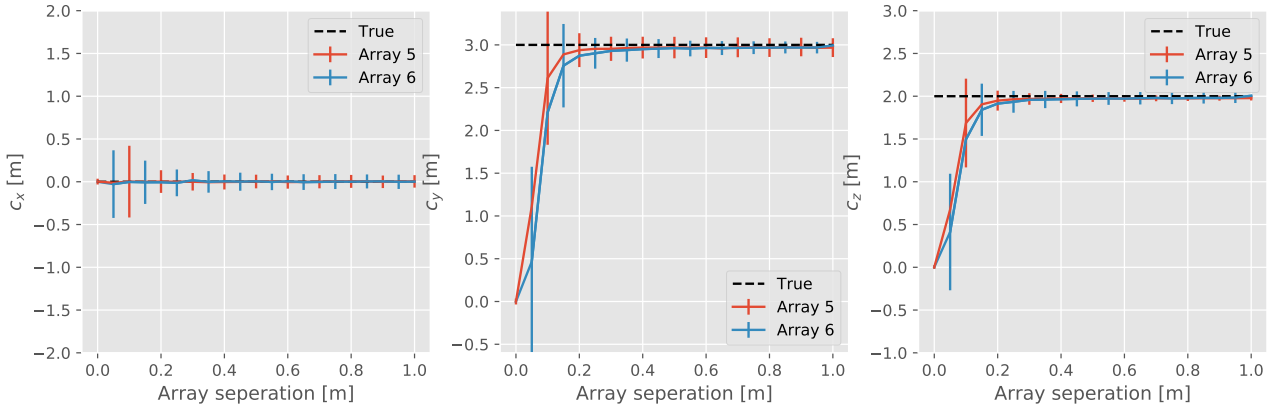

(b) CTS II

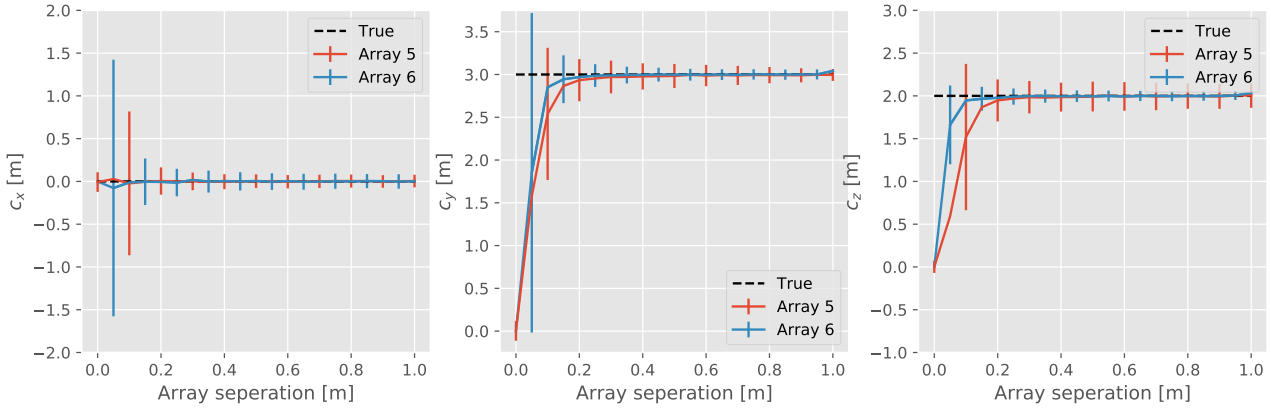

(c) CTS III

Figure 4-7: Shown is the influence of different sensor separation distances for CTS I with Array 2 and 4 and for CTS II-III with Array 5-6 in a noise disturbed sea water environment. The modeled cable setup is C1.

4-2-4 Influence of dipped cable

In the previous sections, only horizontal cables without dip are considered. In this paragraph, cable setup C1 is analyzed in sea water with noise for different dip angles of $0 - 60°$. The results for CTS I, CTS II and CTS III are presented with the same sensor arrays as in the previous sections. The dip of a cable can be also interpreted as a tilted sensor array relative to a horizontal cable for a homogeneous domain. The results for CTS I, CTS II and CTS III are presented in Figure 4-8.
The influence of a tilted cable on the inversion results of CTS I for both Array 2 and 4 is small. For dip angels below 40°, the mean estimated cable location for CTS II and III follows the true position. However, for Array 5, the standard deviation of the inversion is steadily increasing for both CTSs. CTS II with Array 6 and CTS III with Array 5 loos accuracy for dip angles larger than 40° which manifests in a wrong mean estimation and increasing standard deviation.

Currently, power cables are laid out only on the continental shelf which is characterized by a flat sea topography of a dip angle rarely larger than 1° [46]. Thereby, the cable dip angle relative to the sensor array should be well in the limit for CTS I-III. The dip angle of the cable may exceed the limit at connections to the shore or offshore infrastructures. However, at those sections the cable cannot be approximated as an infinite, straight cable which is an assumption for the expected symmetry of the magnetic field created by the current in the cable. The sensor array, on the other hand, may tilt by larger angles. When the array is dipped by less than 40°, the accuracy of the inversion is not significantly reduced.
In this section, the homogeneous model domain is sea water. When a layered earth is considered, boundary effects can influence the field which means that a tilted sensor array is not equal to a tilted cable.

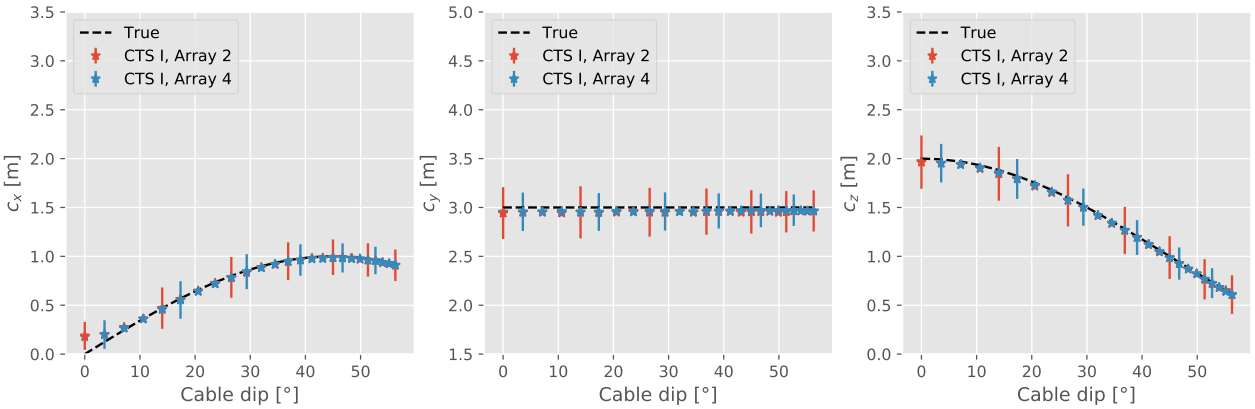

(a) CTS I

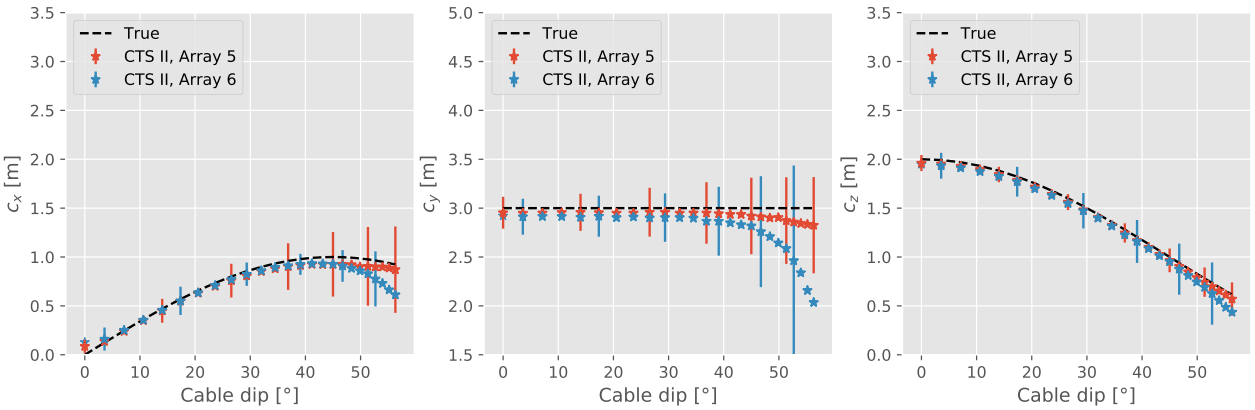

(b) CTS II

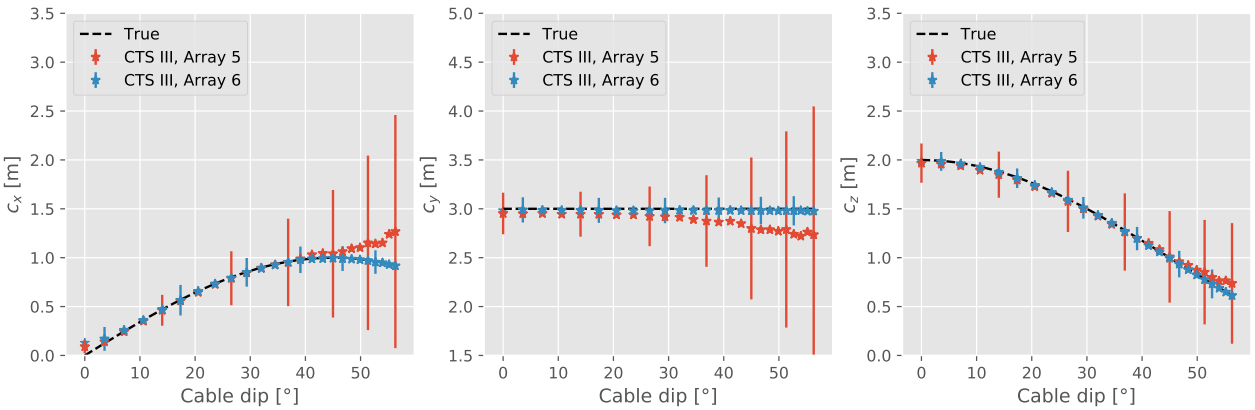

(c) CTS III

Figure 4-8: Shown is the influence of a tilted cable for CTS I with Array 2 and 4 and for CTS II-III with Array 5-6. The modeled cable setup is C1.

4-2-5 Influence of tone frequency

An electromagnetic field, propagating in sea water, will attenuate due to the conductive of the environment. The attenuation factor is the skin depth δ which is defined as the distance where the signal amplitude has reduced by a factor of $1/e$. The skin depth is the inverse of the propagating constant γ: $\delta = 1/\gamma$. Figure A-21 in Appendix A-2-3 shows the skin depth relative to frequency for soil and sea water. With increasing frequency, the skin depth is decreasing and the EM field attenuates faster. The attenuation curve for different frequencies of a field produced by a line source is shown in Figure 2-3a. The influence of tone frequency on inversion is shown in Figure 4-9. The relative depth between sensor array and cable is 2 m and the horizontal offset is 3 m, which is cable setup C1. The model domain is homogeneous sea water with noise. CTS I and II loose accuracy in predicting the cable position with increasing frequency. The loss in accuracy becomes significant for tone frequencies higher than 40 Hz. CTS I and II rely on a model which is based on a static line source. For larger tone frequencies, the error due to the approximation of the cable as a static source increases which results in an increasing inversion error. CTS III is not based on a model and the inversion is independent of the frequency. However, with increasing frequency the signal to noise ratio decreases because of the weaker signal. This effect is not significant for the chosen noise source, the distance between sensors and cable, and the frequency range which is under 500 Hz.

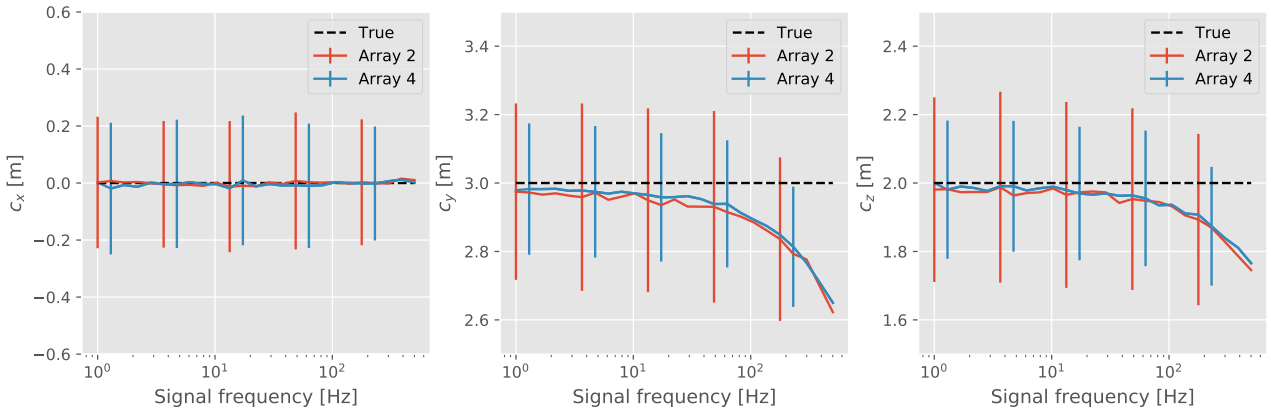

(a) CTS I

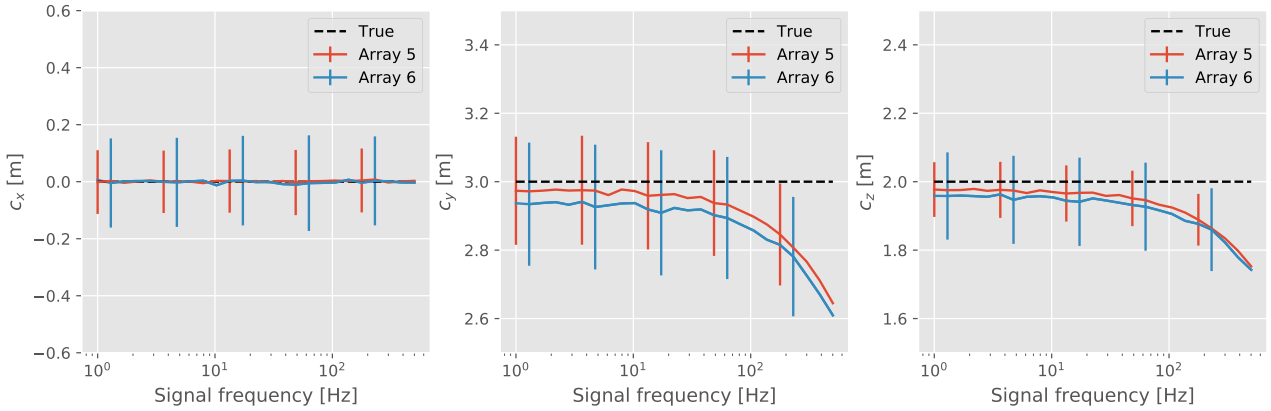

(b) CTS II

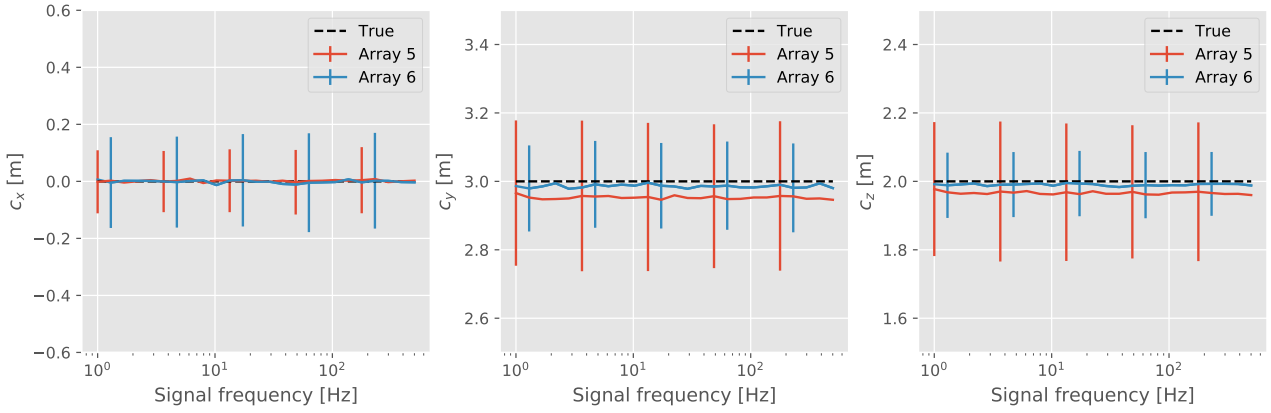

(c) CTS III

Figure 4-9: Shown is the influence of tone frequency injected in the cable for CTS I with Array 2 and 4 and for CTS II-III with Array 5-6. The modeled cable setup is C1.

4-3 Influence of soil and air

In Section 2-2, a numerical model for a three-layered earth is presented. The layers used are air ($\rho_a = 2 \times 10^{20}\,\Omega$m, $\mu_{r,a} = 1$, $\epsilon_{r,a} = 1$), sea water ($\rho_w = 0.3\,\Omega$m, $\mu_{r,w} = 1$, $\epsilon_{r,w} = 85$) and seabed with marine sediments ($\rho_s = 1\,\Omega$m, $\mu_{r,s} = 1$, $\epsilon_{r,s} = 23$). In this section, the influence of a layered earth is studied without noise. Four different environments are studied here; A homogeneous sea water domain, a two-layer model consisting of sea water and marine soil, a two-layer model consisting of sea water and air, and the three-layer model mentioned above. A two-layer model is created by using the three-layer model where two layers have the same resistivity and permeability. All models are permittivity independent because of the low frequency assumption. CTS I is tested with Array 2, and CTS II and III with Array 5. The cable setup is parallel to the x-axis. c_y relates to the horizontal offset and c_z to the vertical offset. The cable position $c_x = 0\,$m. The tone frequency is 31 Hz.

4-3-1 Water model

Figure 4-10 shows the inversion results of CTS I-III in homogeneous sea water relative to vertical and horizontal offset. Shown is the absolute error between the inverted and the true cable position. CTS I and II loose accuracy with increasing horizontal and vertical offset because both systems do not account for the conductivity of the sea water. CTS III does not show an error because it is not based on a biased model.

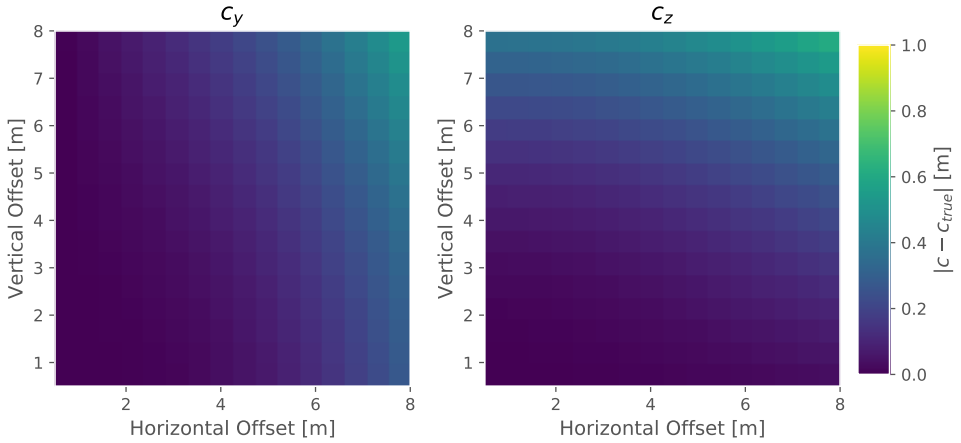

(a) CTS I

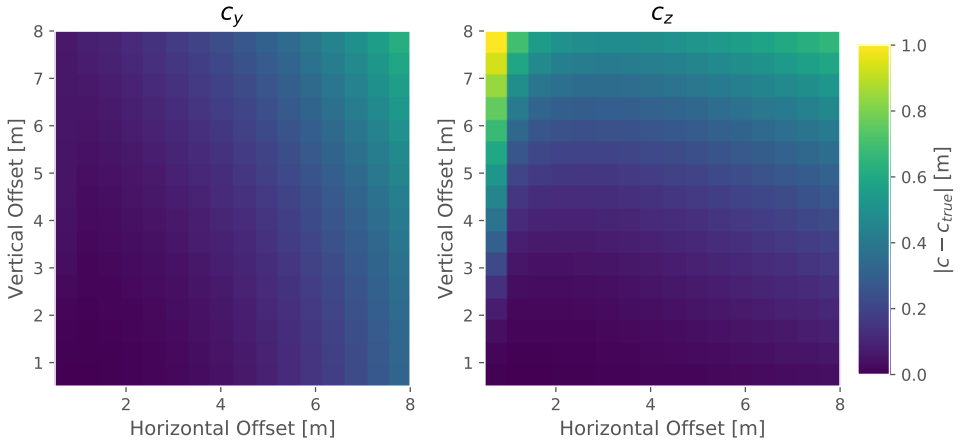

(b) CTS II

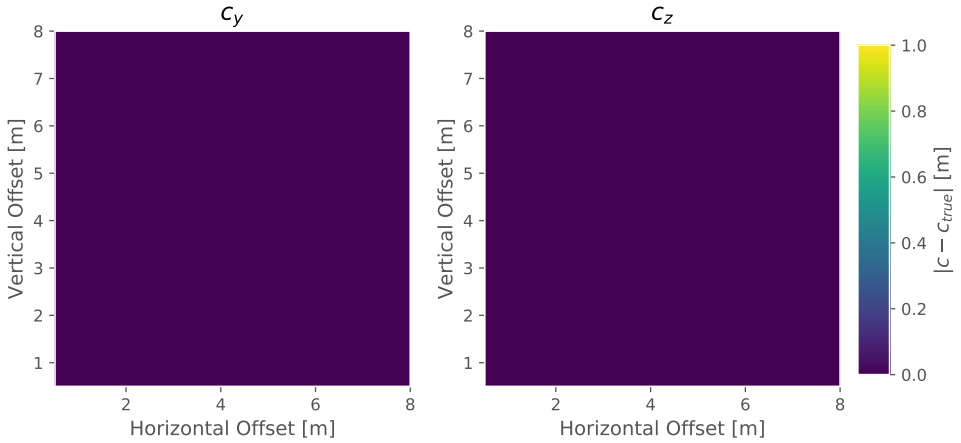

(c) CTS III

Figure 4-10: Results of inverting for a cable in sea water (without noise) for CTS I with Array 2 and CTS II-III with Array 5.

4-3-2 Soil-water model

In this section, the influence of the seafloor is examined. A model consisting of a sea water half-space and a marine soil half-space is considered. The cable is buried in 1 m depth in the soil and the sensors are in the water column. The results for CTS I, II and II are shown in Figure 4-11. CTS I can determine the horizontal and vertical position of the cable with an absolute error of less than 0.3 m for the full investigation depth and offset. The error patterns are changing when compared to the homogeneous sea water results. The soil layer has a larger influence on the accuracy of CTS II than on CTS I. The horizontal position c_y of the cable, inverted with CTS II, can be obtained with an absolute error of less than 0.5 m in a radius of 7 m around the cable. The accuracy in determining the depth c_z reduces when the vertical offset between the sensor array and the cable is much larger than the horizontal offset. CTS III looses accuracy in inverting c_y when the horizontal offset is larger than the vertical offset. The system can invert the depth of the cable with an absolute error of less than 0.4 m in a radius of 4 m around the cable.

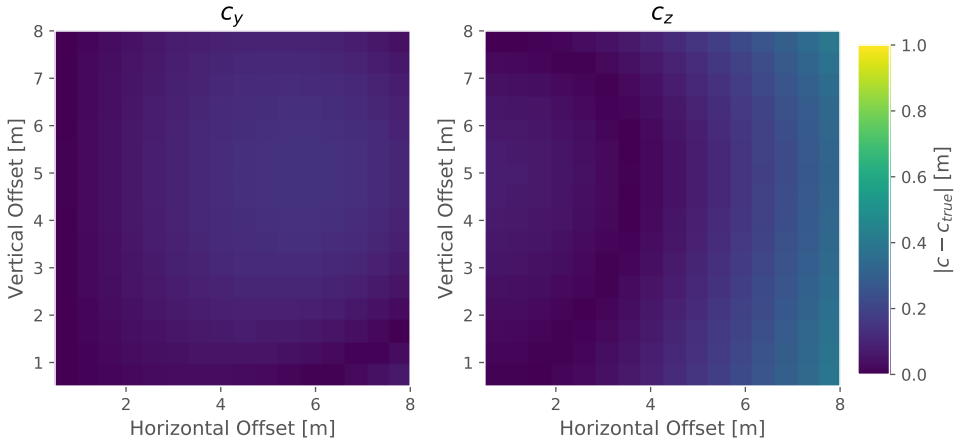

(a) CTS I

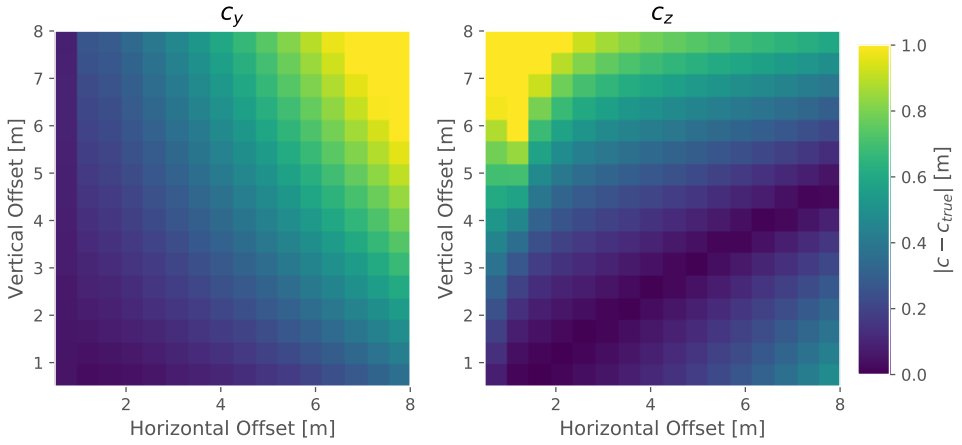

(b) CTS II

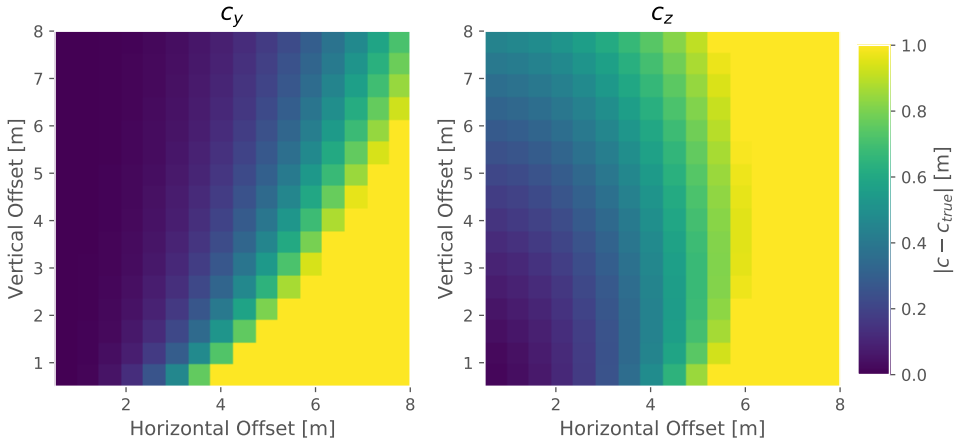

(c) CTS III

Figure 4-11: Inversion results for CTS I with Array 2 and CTS II-III with Array 5. The model domain is sea water with a marine soil half-space and without noise.

4-3-3 Water-air model

This section discusses the influence of the sea surface by modeling a domain which consists of an air and a sea water half-space. The cable is 29 m below the sea level. The sensor array is between the cable and the sea surface, much like it would be if towed during an actual survey. Inversion results for different horizontal and vertical offsets are shown in Figure 4-12. CTS I looses accuracy in inverting for c_y for distances larger than 7 m where the absolute error between the inverted and the true position exceeds 0.5 m. The inversion accuracy of c_z mainly reduces for increasing vertical offsets. When the vertical distance between sensor array and cable is larger than 6 m, the absolute error is more than 0.3 m. CTS II inverts the horizontal and vertical cable position with an absolute error of less than 0.4 m for the entire $8\,\text{m} \times 8\,\text{m}$ model domain. The absolute error patterns caused by the sea surface are similar to the absolute error patterns caused by the seafloor for CTS III. However, the absolute errors are smaller for the sea-air model, i.e. the sea surface interface has a smaller influence on CTS III than the seafloor interface. The horizontal cable position c_y can be determined with an absolute error of less than 0.5 m up to a horizontal offset of 4 m. The cable depth can be determined for distances which are not larger than 7 m with an absolute error of less than 0.4 m.

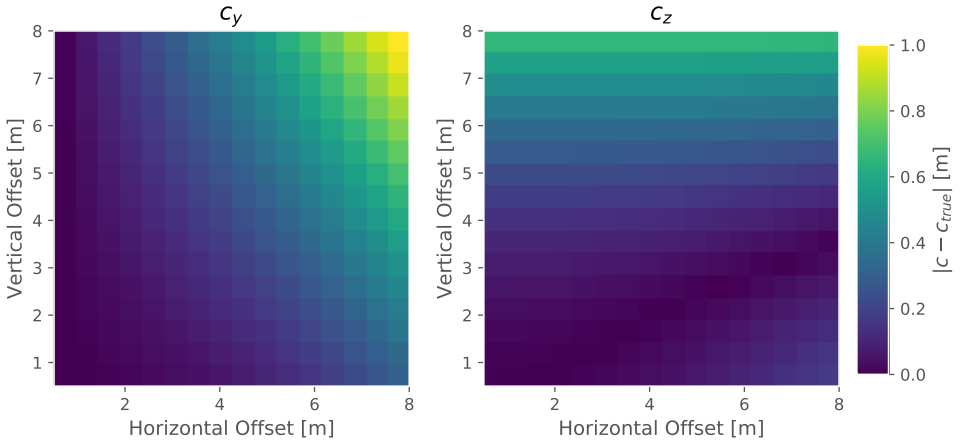

(a) CTS I

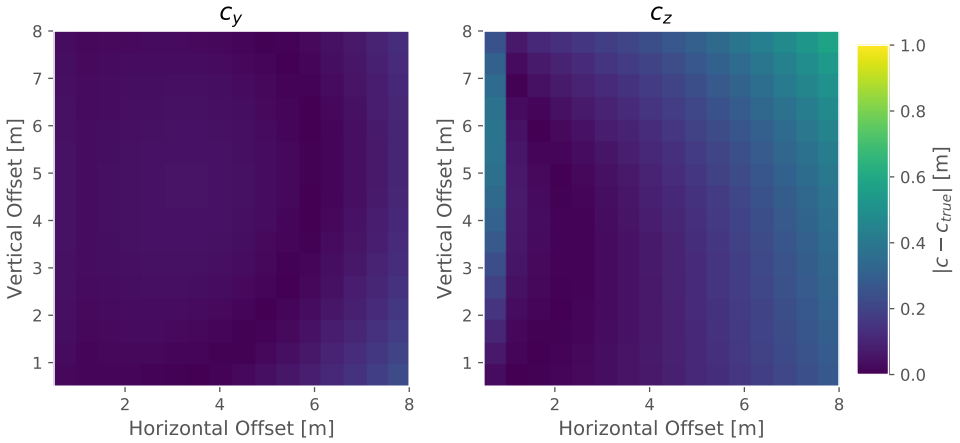

(b) CTS II

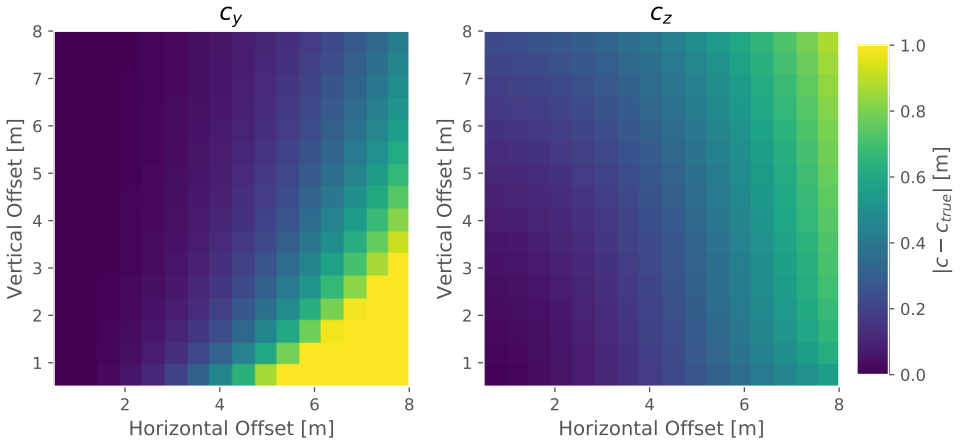

(c) CTS III

Figure 4-12: Inversion results for CTS I with Array 2 and CTS II-III with Array 5. The model domain is sea water with an air half-space on top and without noise.

4-3-4 Soil-water-air model

In the previous sections, the influence of sea water, the sea bottom and air is discussed separately. The conductivity of water biases CTS III less than CTS I and II. The interaction of the EM field with the soil-water boundary reduces accuracy in particular for CTS II and III. The air layer affects CTS I and III more than CTS II. Figure 4-13 shows the inversion results in the three-layer earth with the layers air, sea water and seafloor. The results show some patterns which are similar to patterns recognized from the inversions of the homogeneous sea water and the two-layer models. In general, the inversion results from the three-layer model are more accurate than the results from the soil-water model only. It appears the air half-space counterbalances certain boundary effects from the seafloor. CTS II and III are more influenced by a layered earth than CTS I. The strength and the direction of the EM field are influenced by boundaries. This causes a bigger error for CTS II and III than CTS I, since models II and III rely on all three components of the magnetic field, while CTS I inverts the total, scalar magnetic field.
The study of the three-layered earth model gives some insight in how the cable tracker systems will perform in an offshore measurement campaign. A new inversion scheme might be necessary to include the influences of the marine soil and the air half-space. This new inversion scheme requires more input parameters than the schemes introduced in this project. In particular, the depth and the conductivity of the sea layer, and the conductivity of the marine soil needs to be known. While the conductivity of the sea layer can be measured accurately with a conductivity probe, the conductivity of the marine soil cannot be measured accurately in-situ.

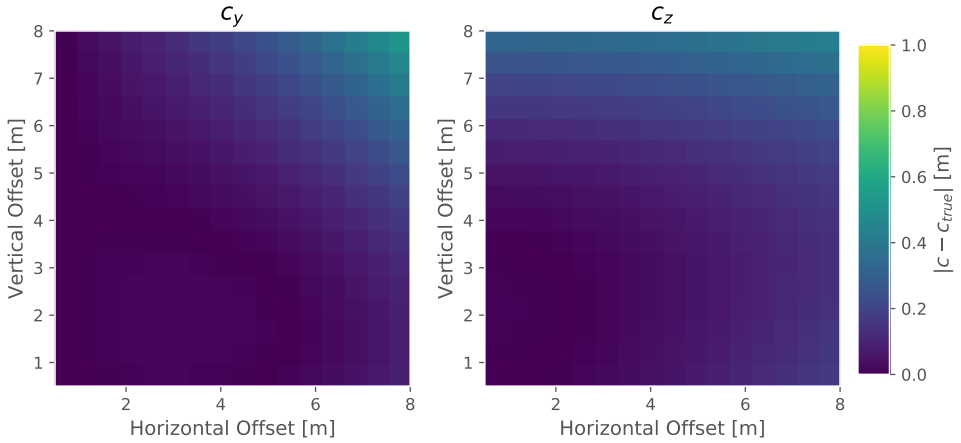

(a) CTS I

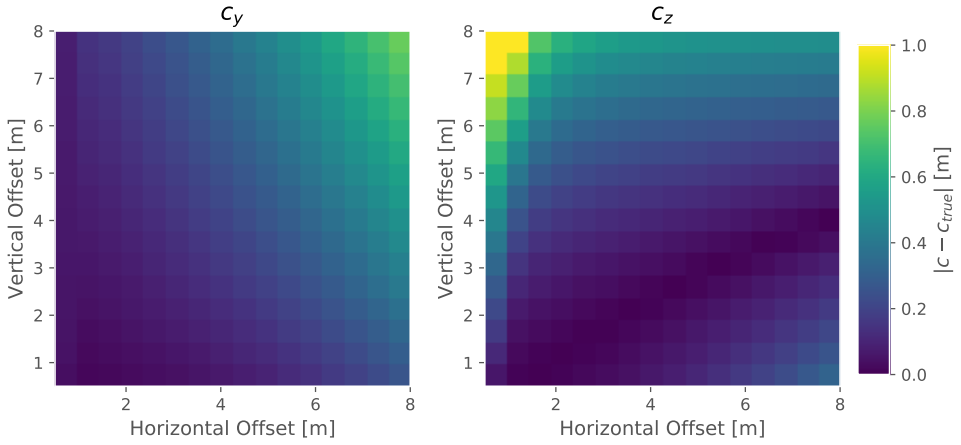

(b) CTS II

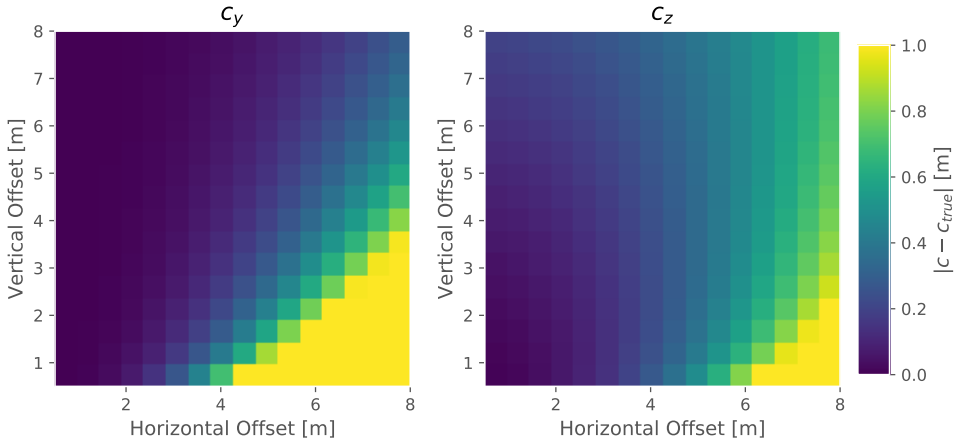

(c) CTS III

Figure 4-13: Results of inverting for a cable in a three-layered earth for CTS I with Array 2 and CTS II-III with Array 5.

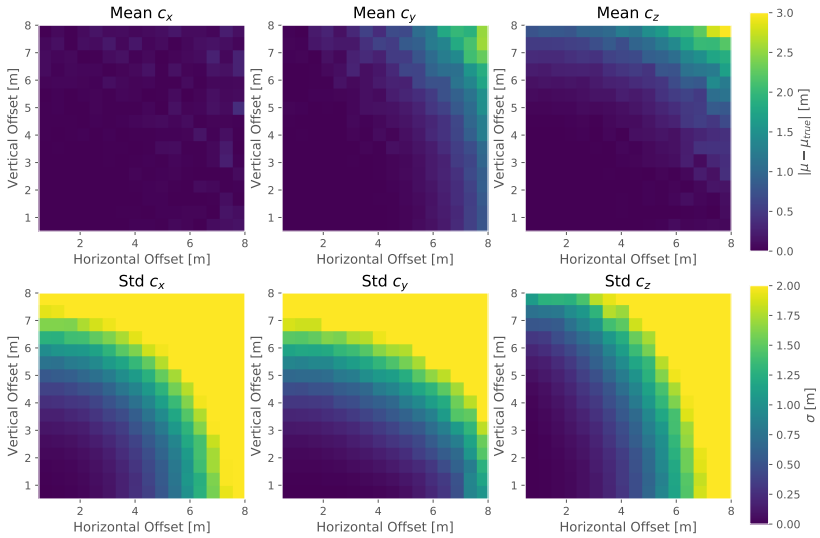

Figure 4-14: The inversion results of CTS I^m are shown with Array 2 in noise disturbed sea water for different sensor positions to the cable. The first row displays the absolute error between the mean estimation and the true value. The second row shows the associated standard deviation.

4-4 Cable tracker system I and II with known current

Several assumptions have been made before developing inversion algorithms for cable tracking. In most cases, the current of the signal in the cable is unknown. CTS I-III are designed based on this assumption. However, the current can often be approximated from the current of the injected tone, the resistance of the cable, and the cable length between the point where the tone is injected and the section which is surveyed.
CTS III is not model based and is independent of the knowledge of the current. Similar to Section 4-2-2, CTS I with Array 2 and CTS II with Array 5 are evaluated for performance in sea water with noise but now for a known tone strength I. The systems are abbreviated as CTS I^m and CTS II^m. The results for CTS I^m are displayed in Figure 4-14 and for CTS II^m in Figure 4-15.
The inversion results of CTS I^m slightly improve due to the known current by comparison to the results from CTS I (c.f. Figure 4-3). This is visible in a more accurate estimation of the mean inverted cable position. The standard deviation does not change significantly. The range where the absolute error between the mean inverted position and the true position is below 1 m and the standard deviation is below 1 m is in a radius of 5 m.
Comparing CTS II^m with CTS II (c.f. Figure 4-5) reveals that knowing the current significantly improves the inversion results of CTS II. The depth of the cable c_z is well estimated for a distance of 8 m with a standard deviation of under 1 m. When the sensor array and the cable are separated by a distance of more than 4 m, the mean inverted horizontal cable position c_y has an absolute error of more than 2 m and the standard deviation is larger than 1 m.

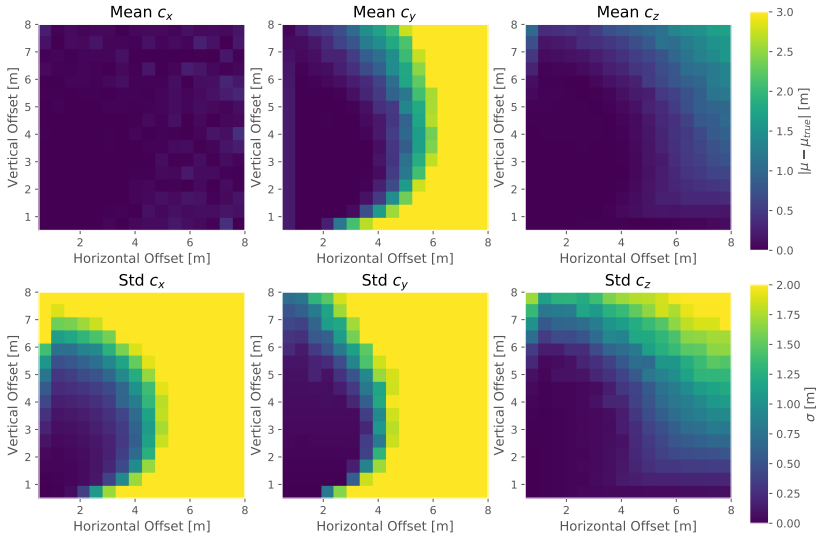

Figure 4-15: The inversion results of CTS II^m are shown with Array 5 in noise disturbed sea water for different sensor positions to the cable. The first row displays the absolute error between the mean estimation and the true value. The second row shows the associated standard deviation.

Chapter 5

Prototype

A prototype has been developed which has been used in a field survey with the aim of detecting and locating the relative position of a test cable. The prototype consists of an array of five synchronized 3-axis fluxgate magnetometers (in total 15 channels) and a 3-axis motion sensor.

5-1 Magnetic sensors and motion sensor

5-1-1 Hardware setup

The direction and strength of the magnetic field is measured with five 3-axis fluxgate magnetometers (FGM3D/100 by *Sensys*). The systems technical parameters can be found in [44]. A relative measuring error of $< 0.1\%$ and a range of $\pm 10\,000\,\mathrm{nT}$ are stated. The sample frequency used during the testing of the prototype is 1000 Hz and the maximum frequency of a continuous signal which can therefore still be reliably sampled according to the sampling theorem is 500 Hz.
For detecting the absolute orientation of the sensor array, we use the BNO055 motion sensor by BOSCH. This device consists of a triaxial gyroscope, accelerometer and magnetic compass sensor. Using a built-in fusion algorithm processed on an Arduino micro controller, the data are merged to calculate the absolute orientation of the device in a global coordinate system. The system is spanned by magnetic North $\hat{\mathbf{e}}_N$, East $\hat{\mathbf{e}}_E$ and the gravitational vector $\hat{\mathbf{e}}_g$. The orientation is given in Euler angles ($\Phi \in [-180°, 180°]$, $\Psi \in [-180°, 180°]$ and $\Theta \in [-90°, 90°]$) relative to the global coordinate system. The data output rate of the processed data is around 100 Hz. The manufacturer does not supply an accuracy for the processed orientation, though, the accuracy of each subsystem sensor are stated in [47].

5-1-2 Software setup

The magnetic and orientation data are transferred via Ethernet using an *User Datagram Protocol* (UDP) connection to a laptop computer which records and monitors the data using

an application written in Python 3.4. Two independent measuring systems are used which are not time-synchronized. When the laptop receives and stores a data package, it adds a computer time stamp which is used for synchronizing both data types. Since the amount of motion is limited during the field tests, further time synchronization or sample rate matching is not considered necessary. The data is stored as a time series to ASCII files for processing and analysis.

Before the data can be inverted, they need to be processed. Two different schemes for processing the magnetic time series have been used and these are explained in detail and compared against each other in the following sections. After processing, the magnetic response of the cable at the frequency of interest is obtained from the time series which have been measured. Every sensor measures three axes, which gives 15 magnetic field parameters in total for an array of five sensors. These 15 parameters are the input for the inversion codes from which the location of the cable is calculated. The current status is that the processing schemes are not carried out in real time, i.e., the data are first recorded. After the measurement is finished, the data are processed and inverted. The data from a single measurement can be processed and inverted as a whole. This is done when the sensor array is static and stable during the recording. The method can be used with and without motion sensor. If the BNO055 is not used, the cable position is inverted in a local coordinate system with the axis of the magnetometers as reference. When the sensor array is moving through the duration of the measurement, windowing is applied and each data set is processed and inverted separately. The appropriate length of the window depends on several factors which are survey speed, sample frequency and frequency of injected tone.

5-2 Processing

When five sensors are used, 15 channels measure magnetic components at five different positions and in three directions. The channels are separately processed to obtain the magnetic field strength at the frequency of interest ($f_s = 31\,\text{Hz}$), which is the dominant frequency of the block function of the injected signal. In this section, we describe two different processing schemes and compare them afterwards.

5-2-1 Processing based on band-pass filtering

The first processing scheme operates in time domain. A bandpass filter with a narrow bandwidth (1 Hz) around the frequency of interest is applied. The filtered data consist of the signal emanated by the test cable and residual noise. The desired signal is a sine curve with the frequency of interest. Its amplitude A can be determined from the variance σ^2 [48]:

$$A = \sqrt{2\sigma^2}. \tag{5-1}$$

The bandpass filter which is used in this project is a standard Butterworth filter with low and high cutoff frequencies of $f_c \pm 0.5\,\text{Hz}$ and order 6. The order is chosen in such a manner that a good compromise between complexity of the filter design and attenuation beyond the cutoff frequency is achieved. The benefit of using a Butterworth filter is its frequency response,

which is as flat as mathematically possible in the frequency band passed. In other words, it does not have ripples [49]. According to [50], down sampling is required if the sampling frequency is much higher than the cut-off frequencies of the band pass filter, as it is the case here. Before filtering, the sampling frequency is reduced by a factor of 10 to 100 Hz. The filtered time series are therefore sufficiently sampled to resolve a maximum frequency of 50 Hz without aliasing. The frequency response of the designed filter is shown in Figure 5-1.

Filter design discussion

The Butterworth filter is an Infinite Impulse Response (IIR) filter which is designed for steady-state operations (i.e. large number of samples). This type of filters performs poorly when a small number of samples are processed due to the transient effect when the frequency response of the filter depends on the number of data samples [51]. A simple way of manipulating a short data set to obtain the steady-state behaviour is to duplicate and append it multiple times where every second duplication is additionally reversed. The artificially extended time series will suffer less from transient effects. Using these techniques, recordings of above 0.5 s (500 samples) can be processed.

Another type of filters which might be worth to investigate in more detail are the Finite Impulse Response (FIR) filters. Contrary to an IIR filter, the response of a FIR filter has a finite response. A FIR filter is always stable which gives flexibility in designing a filter of certain characteristics. Additionally, it has a linear phase which means that the group delay of the signal is almost constant. Finally, it does not suffer from transient effects. It is faster in processing data sets of small sample number. However, a higher order FIR filter is required in comparison with an IIR filter to achieve a similar filter response [52].

5-2-2 Processing in frequency domain

The signal strength of the center frequency f_s can be obtained from the Power Spectrum (PS) which has the unit T^2 and describes the power at frequency f of a random, deterministic time series as a statistical average [53]. The PS can be estimated from a finite measurement using *welch's* method [54]. In this method, the time series is split into multiple sections. On each section, a windowed discrete Fourier transformation (DFT) is performed. The squared average over all transformed sections estimates the PS. Windowing is used to get the desired frequency resolution and to reduce noise. A window function is also required to reduce edge effects. It is common practice to apply a fast Fourier transformation (FFT) for calculating the DFT and we have done so here. The window function we apply is a Hanning function with half overlapping windows, a common choice for data with random characteristics [55]. The window length is 1000 samples which yields a frequency resolution of $df = 1$ Hz. The speed of the FFT will increase if 1024 samples are used because the FFT method is optimized for 2^n samples [56]. Therefore, we add 24 zero samples to each window (zero padding). This does not change the resolution but increases the number of frequency bins. The square root of the power at our sought-after frequency of 31 Hz gives the amplitude of the dominant frequency of the block function.

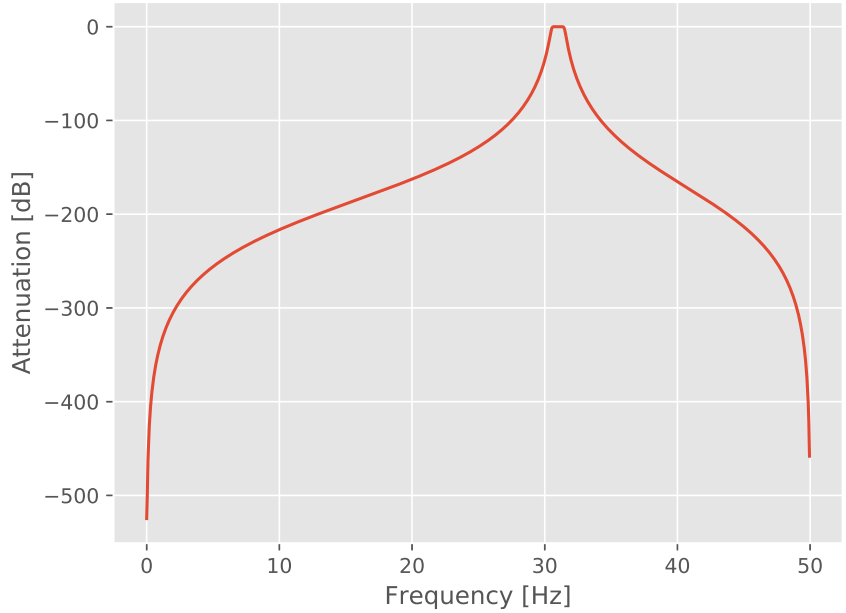

Figure 5-1: Frequency response of the applied Butterworth filter after down sampling the sampling frequency to 100 Hz.

5-2-3 Comparison

Both processing schemes are tested on actual data recorded during the field test. Five sensors (S0, S1, ..., S4) in a fixed frame measure the ambient magnetic field including the signal that is emanated by a cable that carries a block signal of dominant frequency 31 Hz. The survey and its results are described in more detail in Section 6. We will, however, briefly use some of the results from the field test to analyse the response of each of the two filter methods.
Processing is applied on an exemplary measured set of time-series. Table 5-1 shows the total magnetic response at 31 Hz for the individual sensors, obtained with the time-domain and frequency-domain scheme. Sensor S0 is closest to the cable and shows the strongest field strength and S4 is furthest away with the smallest field strength. The decrease in measured field strength with distance from the cable can be seen in both processing schemes. The obtained amplitudes with the time-domain scheme are slightly higher than with the frequency-domain scheme. Nevertheless, the ratio of both results for each sensor is constant 0.76 and we conclude that both schemes perform equally well. Except from a scaling factor, the processed measurements are the same.
The simple implementation of both processing schemes relies mainly on the Python package *scipy* and the script is not optimized for computational speed. In an average over 1000 iteration, the time-domain method takes 0.026 s to process all 15 magnetic channels. The frequency-domain processing is around four times faster when performing the same task since it only takes 0.006 s to process the same data set. The reduced processing time might be important in future implementation of the processing scheme in dynamic measurements.

Sensor	$\lvert\mathbf{B}\rvert$ [nT] Time-domain	Frequency-domain	Ratio
S0	1.62	1.24	0.76
S1	1.58	1.21	0.76
S2	1.52	1.16	0.77
S3	1.41	1.07	0.76
S4	1.33	1.01	0.76

Table 5-1: Processing results of an exemplary measurement with five sensors. The obtained values can be used for the inversion scheme. Additionally, the ratio between the processing results in time-domain and frequency-domain is shown.

Chapter 6

Measurement on a field cable

The prototype has been tested on a field cable. Two surveys have been conducted in a static set up. The first survey tests the CTS performance without the motion sensor and studies the inversion accuracy relative to offset. The second measurement campaign tests the implementation including the motion sensor. Involving data from the motion sensor, measurements in a relative frame can be converted into measurements in global reference system.

6-1 Cable setup and measuring environment

For testing the prototype, a field cable is installed in a field that has been verified to be little electromagnetic disturbed in the frequency range of interest from noise measurements. The object of detection is a thin, unshielded and unburied stranded copper wire of 3 mm diameter. The cable is laid out in approximately the shape of the letter U of size 100 m × 15 m with the parallel sides being the small sides. The static measurement is conducted at the center of the long side to reduce the interference effects that come from the side of the U-cable. This setup approximates a line source. The circuit is closed at the opposite side via a ground connection between the ends of each of the short cable sections. As electrodes, two steel rods are used. A square wave signal is applied to the cable. The chosen dominant frequency is 31 Hz and a voltage of 10 V is used. The total resistance of the circuit is measured as 85 Ω and the calculated current in the circuit is 0.12 A.

6-1-1 Sensor setup

A vertical sensor array (Array 6) is tested with individual sensor spacing of 0.25 m. The lowest sensor is 0.6 m above the ground. The frame is installed relative to the cable in such a way that the x-axes of the sensors are parallel to the cable and the z-axes show downward. The noise level at the site is 0.01 nT which is determined from noise measurements at 31 Hz. An image of the survey site and setup is shown in Figure 6-1. The typical spectrum of a

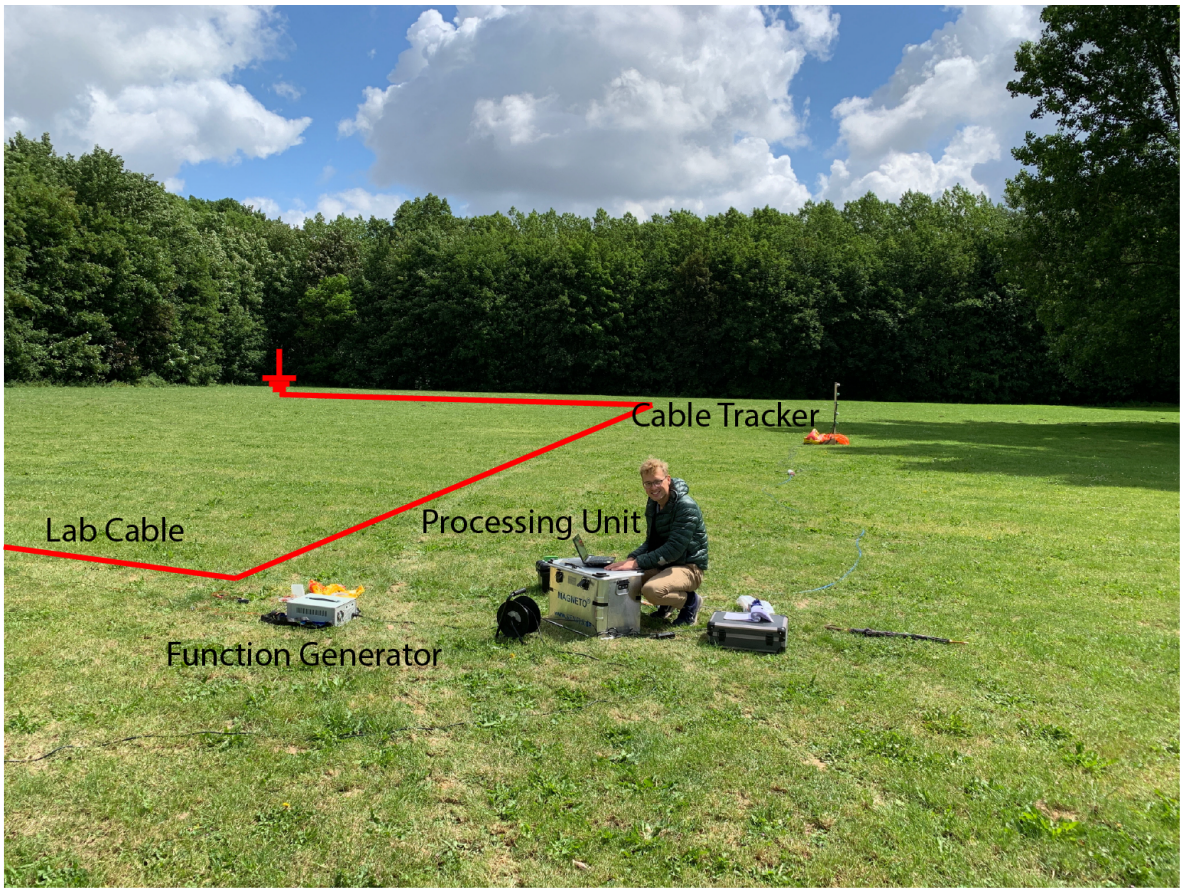

Figure 6-1: Shown is the survey site where the cable tracker prototype is tested for detecting a laid out field cable.

measurement with active cable is shown in Figure 6-2. The peak at 31 Hz is the dominant frequency of the injected square wave signal. The odd multiples (93 Hz, 155 Hz, ...) of the dominant frequency are also visible but with much smaller amplitudes. The peaks at 50 Hz and its odd multiples (150 Hz, 250 Hz, ...) are caused by surrounding power lines as well as the generator used to power all electronics during the measurement.

6-2 Offset study without motion sensor

For the static measurement campaign, recordings of 20 s are taken at incremental horizontal offsets. Each recording is processed in its entirety using the time domain processing scheme. The inversion results are shown in Figure 6-3a. The relative errors in reference to the expected cable position are shown in Figure 6-3b. A relative error for c_x cannot be given because the expected value is zero. CTS II can invert the position of the cable for offsets smaller than 2 m with a relative error of below 40 %. For larger offsets, the inversion results are further off and divert from the expected solution to such a degree as to be unusable. CTS III inverts the cable position with a relative error of less than 20 % for an offset of $1-3$ m. Beyond 3 meter offset, c_y can be still inverted with a relative error of less than 20 %.

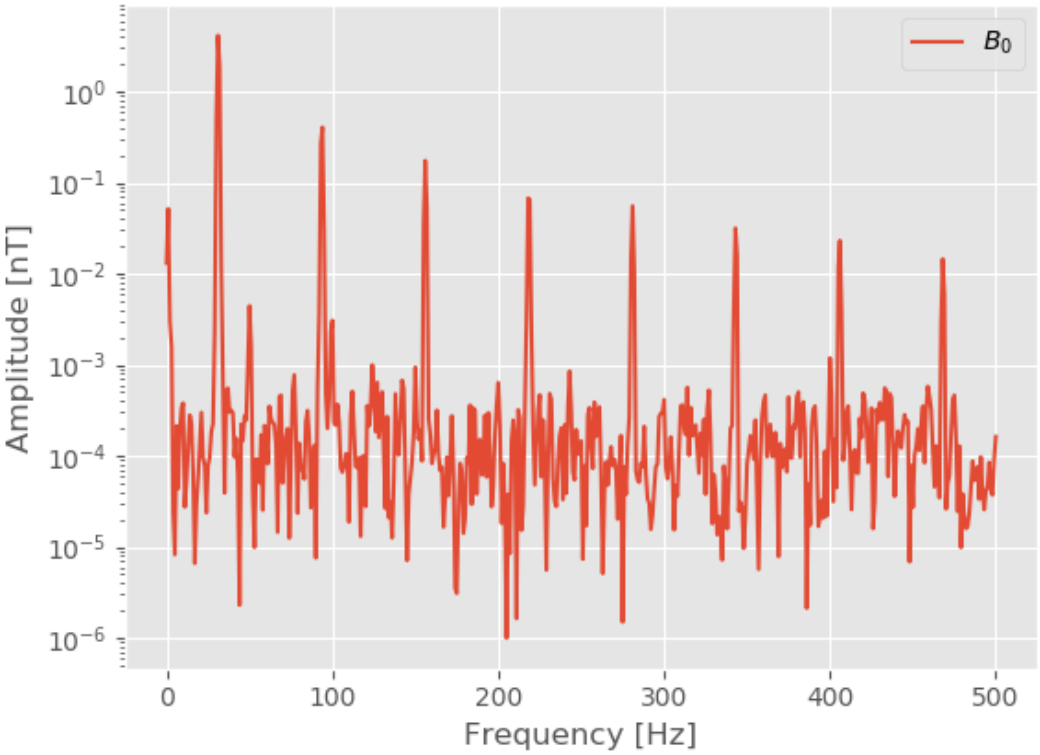

Figure 6-2: Shown is an exemplary spectrum of a measurement with active cable.

However, the relative error of c_z exceeds 40 %. At 8 m offset, the inversion for c_x is off by 2 m from the expected cable position. For offsets smaller than 1 m, the relative error of the inversion is increasing. CTS I is not tested because in Section 4-1 we show that this system does not work with a vertical sensor array.
The cable distance relative to the sensor frame is known with an accuracy of approximately 5 cm. Cable heading, however, is more difficult to assess in the field. When the sensor axes are not aligned with the cable heading as expected, a significant systematic error occurs for finding the true cable position in the reference system of the sensors. An unintended minor rotation of the sensor frame where the axis of the sensors does not align with the desired direction may occur especially for larger offsets. The results from Figure 6-3 show how the CTSs perform in general but cannot be used to state an exact accuracy of the systems. Data from a motion sensor will be required for an improved measuring setup. This will be discussed in more detail in the next section.

CTS II looses accuracy for offsets larger than 2 m. This behaviour is analyzed by comparing the inverted current and the inverted distance. The inverted current I, the inverted distance c_r and the ratio I/c_r as well as the expected values are plotted in Figure A-22 of Appendix A-3. The expected current is derived from the circuit resistivity and the input voltage. The inverted current and the distance are deviating from the expected values with increasing offsets. However, the inverted ratio I/c_r is close to the expected ratio. We conclude, therefore, that CTS II is inverting for the ratio of the current and the distance rather than current and distance separately. When we add the known current to CTS II and recompute the results, the system is named CTS II^I. The inversion is closer to the inversion results from CTS III as shown in Figure A-23 of Appendix A-3.

6-3 Sensor array orientation study with motion sensor

The results of the initial field test reveal that it is difficult to accurately determine the true orientation and position of the test cable relative to the cable tracker array. A motion sensor is added to the magnetic field measurement for detecting the orientation of the sensor array relative to North, East and gravity. The heading of the cable is measured in the same global coordinate system with the motion sensor before starting the survey. This makes it possible to correct for misalignment between the arrays' actual and expected orientation.
In this measurement campaign, measurements of 20 s are recorded for different rotations of the sensor array around the z-axis at an offset of 2 m to the cable. The array's bottom sensor is 0.6 m above the ground. At a rotation angle of 0°, the x-axis of the sensor is parallel to the cable and the y-axis is perpendicular. For each recording, the array is rotated by approximately 45°. A single recording is processed all together without windowing. The inversions are carried out excluding and including the motion sensor data. The results are shown in Figure 6-4. When the data from the motion sensor is not used (CTS II and CTS III), the relative position of the cable to the sensor is changing relative to the rotation of the array. This has an effect on c_x and c_y. The effect on c_z is small since the sensor array is only rotated around the z-axis which shows roughly parallel to gravity. When the motion sensor data is applied to the cable tracker systems, denoted as CTS II^m and CTS III^m, the

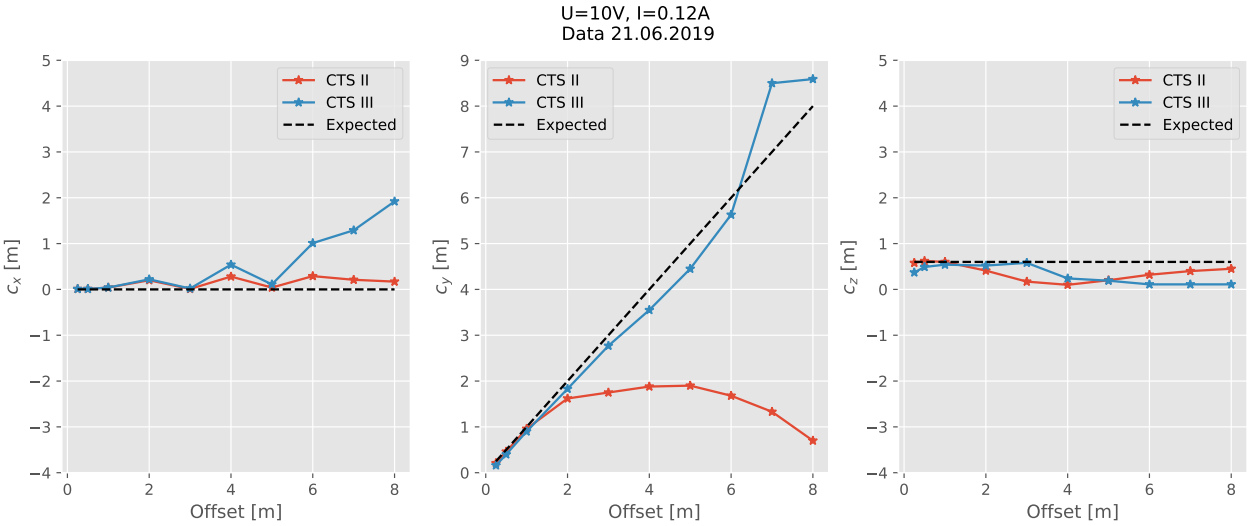

(a) Inversion results with CTS II and CTS III

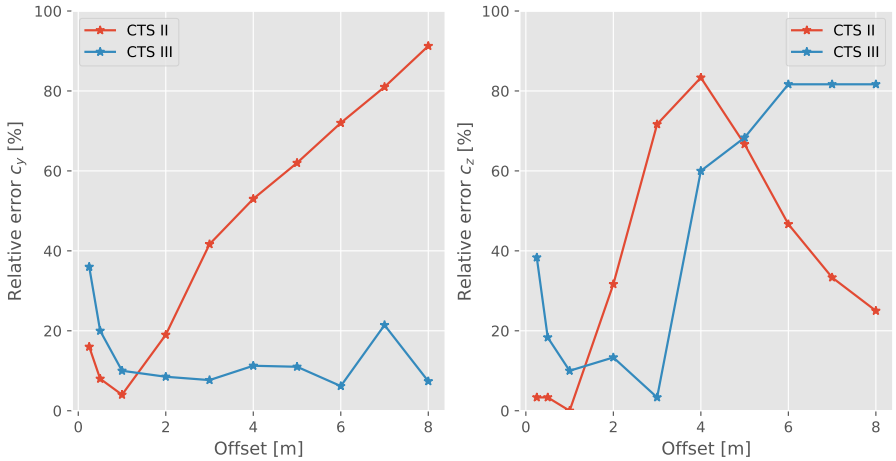

(b) Relative error of inversion results with CTS II and CTS III. The relative error of c_x cannot be calculated.

Figure 6-3: Shown are the inversion results with CTS II and CTS III in a field experiment on a field cable.

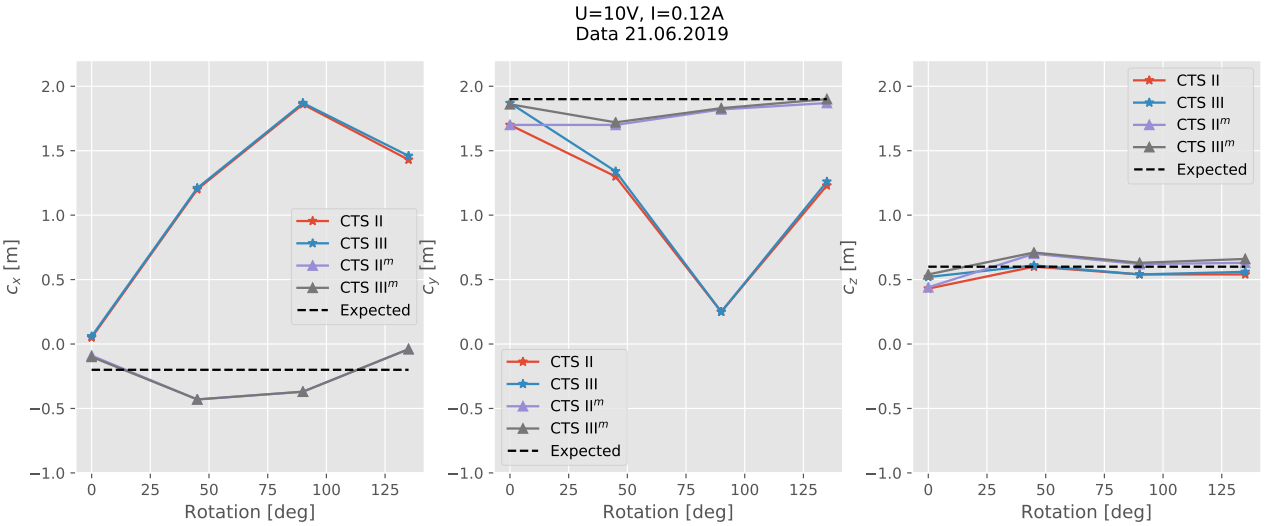

Figure 6-4: Different relative orientations of the sensor array to the field cable are studied. CTS II and CTS III show the relative inversion results without including the data from a motion sensor. CTS II^m and CTS III^m include this information.

inverted cable position can be given in a global reference system which is independent of the orientation of the sensor array.

When the survey was carried out, we encountered difficulties with the motion sensor. Calibrating the BNO055 requires a certain motion scheme of the sensor which is carried out before a measurement. Feedback is given when the system is calibrated. Unfortunately, during many recordings an initially calibrated sensor switched its status to non-calibrated. The data set which is presented in this section, however, did not encounter calibration problems when recorded.

Chapter 7

Conclusion

Submarine power cables are an important part of modern-day electrical infrastructure. After installation, their position on or in the seabed is usually known with low accuracy only. Additionally, sedimentary and tidal movements, and external influences can shift the cable during its lifespan. The power cable position needs to be accurately known to assure quick repair times in case of failure. Submarine cables are usually buried in the seabed to protect it from external damage, especially in low water depths. The cable depth needs to be determined to detect if a cable runs the risk of becoming exposed, which may need counter-measures such as reburial or rock dumping, to prevent damage once exposed. Cable tracking systems are required for detecting the position of submarine power cables. Different devices are available on the commercial market for this task. All systems known to the author, however, are limited in terms of positioning accuracy and detection range. This report presents novel algorithms for detecting and inverting the passive electromagnetic field created by an injected signal in the cable allowing the location of the object to be determined.

7-1 Algorithms

Three methods are developed for finding the cable position from magnetic data. CTS I is a model-based approach which inverts for a static line source in Cartesian coordinates.
CTS II finds the orientation of the cable first. Using coordinate transformations and by taking advantage of the symmetry of the created magnetic field, the initial 3D problem can be reduced to a 2D problem. With a model based inversion assuming a static line source, the cable position is found. Inverse transformation gives the solution in the initial coordinate system.
CTS III relies on a similar coordinate transformation as CTS II and the problem is also reduced to 2D. In CTS III, the cable position is determined by finding the intersection of multiple vectors in a least-square manner.

7-2 Evaluating the algorithms

CTS I-III has been evaluated for different sensor array configurations on synthetic data where the array is placed in homogeneous sea water that contains noise. Each algorithm has sets of circumstances and configurations in which it performs better or worse than the other systems. Where CTS II and III are less influenced by sensor array type, CTS I requires special sensor arrays which extend in all three directions. These types of arrays are not suitable for many survey setups where streamlining and a compact layout of the sensors is a condition. CTS II and III can be used with vertical and horizontal sensor arrays which makes them easy to implement on underwater vehicles or rigidly mounted on a survey vessel. However, the sensitivity with respect to the vertical and horizontal offset to the cable depends on the array and CTS algorithm used.
All three CTS algorithms can be used on dipped cables (or on a tilted sensor frame) as long as the dip angle does not exceed 40°. Increasing the separation between the sensors does not increase the inversion result after a threshold of 0.4 m is passed. Signal (tone) frequency does not influence CTS III, while CTS I and II loose accuracy for frequencies larger than 40 Hz. The sea surface and the sea bottom have an impact on the inversion accuracy. CTS II and III are especially influenced by this because they rely on Bx, By and Bz which are changing independently. The absolute error caused by the layered earth can exceed 1 m. The current of the signal in the cable is usually either unknown or known only approximately. When the current is known, CTS I and especially CTS II improve. CTS III is independent of this added information since it does not used the current as a parameter in its inversion.

From the theoretical performance tests, we conclude that CTS I works superior over CTS II and III. CTS I can detect the cable position at a distance of 6 m with a standard deviation of 1 m in noise disturbed sea water. However, it is limited by the sensor array. CTS III works for almost any sensor array and has a practical sensing range of 5 m. The object of this project, developing a submarine power cables tracker system with sensing range of 5 m with a standard deviation of less than 1 m, is, therefore, achieved on synthetic data with noise, modeled in sea water. When adding the influence of the sea surface and sea bottom in synthetic analysis, the systems might exceed the required limits.
A prototype has been developed which consists of five three-axis fluxgate magnetometers and a motion sensor. CTS II and III have been tested on a field cable with a vertical sensor array. The results show that, using the given equipment, the cable position can be found. With the aid of a motion sensor, the inverted position can be transformed from a local into a global reference system. The survey design, which has been used, is not sophisticated enough to give a reliable estimation of the accuracy of the prototype.

7-3 Recommendations for future research

Further studies need to be conducted for finalizing a system. First, the influence of soil and sea surface needs to be examined in more depth. In order to arrive at a practically applicable tool, more extensive field testing will also need to be carried out. This includes measurements on land (where different sensor arrays and relative positions to the cable can be easily tested)

and offshore trials. A positioning system needs to be included which does not only measure the relative orientation of the sensor frame but also the global position. For land measurements, the combination of a motion sensor with a Global Positioning System (GPS) is recommended. This will give high-accuracy (in the order of several cm) positions for both cable and sensor array against which the inversion outcomes can be compared. For offshore measurements, an additional USBL system is required which gives the relative position of the sensor frame to the vessel. The low accuracy of USBL systems (0.2-1m) will make drawing accurate conclusions from such measurements difficult, so it is imperative that model behaviour can be predicted as accurately as possible before sea trials.

Currently, the system has been used only in performing static measurements. Real time processing needs to be included for finding the position of the cable during actual survey works. This is a vital step to take in developing a functional tool as it allows the skipper of the survey vessel to follow the cable during measurements, assuring that the sensors stay in detection range during the survey works. Finally, a graphical user interface needs to be developed which is helpful for improved field measurements and to give a quick overview of system performance, ambient noise and solution accuracy during field measurements.

Bibliography

[1] European Subsea Cables Association, *Submarine Power Cables*, 2013. [Online]. Available: https://www.escaeu.org/articles/submarine-power-cables/.

[2] Nexans, *Nexans project briefing - NorNed submarine high-voltage link*, 2008. [Online]. Available: https://www.nexans.nl/eservice/Netherlands-nl_NL/navigatepub_199872_-17851/Official_opening_of_the_NorNed_cable_today.html.

[3] W. Andrew, *HVDC vs. HVAC cables for offshore wind*, 2011. [Online]. Available: http://newenergyupdate.com/wind-energy-update/hvdc-vs-hvac-cables-offshore-wind.

[4] M. Jagau and M. Patt, "Reactive Power Operation of a Single Phase AC-AC DAB Converter," in *International Exhibition and Conference for Power Electronics, Intelligent Motion, Renewable Energy and Energy Management*, VDE, 2017, pp. 1–4, ISBN: 3800744244.

[5] General Cable, *NSW Power Brochure*, Casanova, 2017. [Online]. Available: http://nsw.de/Portals/0/Blobs/1221/NSW_Power-Brosch%C3%BCre_11_2017_Screen.pdf?ver=2017-11-23-122105-890.

[6] T. Worzyk, *Submarine Power Cables: Design, Installation, Repair, Environmental Aspects*. 2009, ISBN: 9783642012693. DOI: 10.1007/978-3-642-01270-9.

[7] Subsea Cables UK, *Submarine Power Cables Ensuring the lights stay on!* 2019. [Online]. Available: https://www.escaeu.org/articles/submarine-power-cables/.

[8] H. B. G. Casimir and J. Ubbink, "The Skin Effect. I. Introduction. The current distribution for various configurations," *Philips' technical review*, vol. 28, pp. 271–283, 1967.

[9] H. Thomas, A. Marian, A. Chervyakov, S. Stückrad, D. Salmieri, and C. Rubbia, "Superconducting transmission lines - Sustainable electric energy transfer with higher public acceptance?" *Renewable and Sustainable Energy Reviews*, vol. 55, pp. 59–72, 2016, ISSN: 18790690. DOI: 10.1016/j.rser.2015.10.041.

[10] G. Templeton, *World's first superconducting power line pavages the way for billions of dollars in savings, more nuclear power stations*, 2014. [Online]. Available: https://www.extremetech.com/extreme/182278-the-worlds-first-superconducting-power-line-paves-the-way-for-billions-of-dollars-in-savings.

[11] A. Raja, B. Vissouvanadin, T. Vu, G. Teyssedre, and N. Sinisuka, "Space Charge Measurement on XLPE Cable for HVDC Transmission using PEA Method," *Procedia Technology*, vol. 11, no. Iceei, pp. 327–333, 2014. DOI: 10.1016/j.protcy.2013.12.198.

[12] M. E. Kordahi, S. Shapiro, and G. Lucas, "Global Trends in Submarine Cable System Faults," *SubOptic 2010*, vol. 1, pp. 1–8, 2010. [Online]. Available: https://suboptic.org/resources/suboptic-2010/.

[13] A. Forbes, "Submarine cables: the handbook of law and policy," *Australian Journal of Maritime & Ocean Affairs*, pp. 162–163, 2015, ISSN: 1836-6503. DOI: 10.1080/18366503.2014.964389.

[14] R. Bannon, "Remotely operated vehicles evolution for maintenance and repair of fiber optic systems," *IEEE Conference and Exhibition*, vol. 1, pp. 489–496, 2002. DOI: 10.1109/oceans.2000.881304.

[15] L. Carter, D. Burnett, S. Drew, G. Marle, L. Hagadorn, D. Bartlett-McNeil, and N. Irvine, "Submarine Cables and the Oceans - Connecting the World," *UNEP-WCMC Biodiversity Series*, vol. 31, 2009. [Online]. Available: http://www.iscpc.org/publications/icpc-unep_report.pdf.

[16] T. Szyrowski, S. K. Sharma, R. Sutton, and G. A. Kennedy, "Developments in subsea power and telecommunication cables detection: Part 1 - Visual and hydroacoustic tracking," *Underwater Technology*, vol. 31, no. 3, pp. 123–132, 2013, ISSN: 17560543. DOI: 10.3723/ut.31.123.

[17] M. Asif and M. Rizal, "An Active Contour and Kalman Filter for Underwater Target Tracking and Navigation," in *Mobile Robots: towards New Applications*, 2012, pp. 373–392. DOI: 10.5772/4699.

[18] J. C. Isaacs and R. Goroshin, "Automated cable detection in sonar imagery," *IEEE International Conference on Systems, Man and Cybernetics*, vol. 1, pp. 20–23, 2009, ISSN: 1062922X. DOI: 10.1109/ICSMC.2009.5346577.

[19] T. G. Leighton and R. C. Evans, "The detection by sonar of difficult targets (including centimetre-scale plastic objects and optical fibres) buried in saturated sediment," *Applied Acoustics*, vol. 69, no. 5, pp. 438–463, 2008, ISSN: 0003682X. DOI: 10.1016/j.apacoust.2007.05.002.

[20] E. Kozaczka, G. Grelowska, S. Kozaczka, and W. Szymczak, "Detection of Objects Buried in the Sea Bottom with the Use of Parametric Echosounder," *Archives of Acoustics*, vol. 38, pp. 99–104, 2013, ISSN: 0137-5075. DOI: 10.2478/aoa-2013-0012.

[21] T. Szyrowski, S. K. Sharma, R. Sutton, and G. A. Kennedy, "Developments in subsea power and telecommunication cables detection: Part 2 - Electromagnetic detection," *Underwater Technology*, vol. 31, no. 3, pp. 133–143, 2013, ISSN: 17560543. DOI: 10.3723/ut.31.133.

[22] S. Cowls and S. Jordan, "The enhancement and verification of a pulse induction based buried pipe and cable survey system," *Oceans '02 MTS/IEEE*, vol. 1, pp. 508–511, 2003. DOI: 10.1109/oceans.2002.1193320.

[23] K. Asakawa, J. Kojima, Y. Kato, S. Matsumoto, and N. Kato, "Autonomous underwater vehicle AQUA EXPLORER 2 for inspection of underwater cables," in *Proceedings of the 2000 International Symposium on Underwater Technology*, vol. 1, 2000, pp. 242–247, ISBN: 0780363787. DOI: 10.1109/UT.2000.852551.

[24] J. Kojima, Y. Kato, K. Asakawa, and N. Kato, "Experimental results of Autonomous Underwater Vehicle 'AQUA EXPLORER 2' for inspection of underwater cables," *IEEE Oceanic Engineering Society*, vol. 1, pp. 508–511, 2002. DOI: 10.1109/oceans.1998.725656.

[25] Innovatum, *Submarine Cable & Pipeline Tracking Specialists*, 2019. [Online]. Available: http://www.innovatum.co.uk/.

[26] T. Szyrowski, "An intelligent, fast-acquisition remote sensing system for locating and measuring burial of subsea power and telecommunication cables," PhD thesis, 2017.

[27] S. Takagi, J. Kojima, and K. Asakawa, "DC cable sensors for locating underwater telecommunication cables," *IEEE The Costal Ocean - Prospects for the 21st Century*, vol. 1, pp. 339–344, 1996. DOI: 10.1109/oceans.1996.572765.

[28] T. Szyrowski, S. K. Sharma, R. Sutton, and G. A. Kennedy, "Subsea cable tracking in an uncertain environment using particle filters," *Journal of Marine Engineering and Technology*, vol. 1, pp. 19–31, 2015, ISSN: 20568487. DOI: 10.1080/20464177.2015.1022381.

[29] Evo Logics, *S2C R 48/78 USBL communication and positioning device*, 2018. [Online]. Available: https://evologics.de/acoustic-modem/48-78/usbl-serie.

[30] D. Halliday, J. Walker, and R. Resnick, *Fundamentals of physics*. John Wiley & Sons, 2013, ISBN: 111823071X.

[31] D. J. Griffiths, *Introduction to electrodynamics*. Prentice Hall, 2010, ISBN: 013805326X. DOI: 10.1119/1.4766311.

[32] B. N. Taylor, P. J. Mohr, and M. Douma, *The NIST Reference on constants, units, and uncertainty*, 2007. [Online]. Available: https://physics.nist.gov/cuu/Units/.

[33] B. Ricketti, "Magnetostatics and the Biot-Savart Law," Heriot-Watt University, Edinburgh, UK, Tech. Rep., 2015.

[34] W. Von Aulock, "Propagation of electromagnetic fields in sea water," Dep. of Navy, Bur. of Ships, Washington, DC, Tech. Rep., 1948.

[35] A. S. Inan, A. C. Fraser-Smith, and O. G. Villard Jr, "ULF/ELF electromagnetic fields generated along the seafloor interface by a straight current source of infinite length," *Radio Science*, vol. 21, no. 3, pp. 409–420, 1985.

[36] J. R. Wait, "Electromagnetic fields of current-carrying wires in a conducting medium," *Canadian Journal of Physics*, vol. 30, no. 5, pp. 512–523, 1952, ISSN: 0008-4204.

[37] L. O. Løseth, H. M. Pedersen, B. Ursin, L. Amundsen, and S. Ellingsrud, "Low-frequency electromagnetic fields in applied geophysics: Waves or diffusion?" *Geophysics*, vol. 71, no. 4, W29–W40, 2006, ISSN: 0016-8033. DOI: 10.1190/1.2208275.

[38] J. Hunziker, J. Thorbecke, and E. Slob, "The electromagnetic response in a layered vertical transverse isotropic medium: A new look at an old problem," *Geophysics*, vol. 80, no. 4, F1–F18, 2015, ISSN: 0016-8033. DOI: 10.1190/geo2013-0412.1.

[39] D. Gubbins and E. Herrero-Bervera, *Encyclopedia of geomagnetism and paleomagnetism*. Springer Science & Business Media, 2007, ISBN: 1402044232.

[40] M. E. Hobbs, M. S. Jhon, and H. Eyring, "The dielectric constant of liquid water and vairous forms of ice according to significant structure theory," *Proceedings of the National Academy of Sciences*, vol. 56, pp. 31–38, 1966, ISSN: 0027-8424. DOI: 10.1073/pnas.56.1.31.

[41] H. W. Ho and S. C. Wong, "A Levenberg-Marquardt iterative solver for least-squares problems," *Communications in Numerical Methods in Engineering*, vol. 21, no. 6, pp. 327–335, 2005, ISSN: 10698299. DOI: 10.1002/cnm.757.

[42] J. Traa, *Least squares intersection of lines*, 2015. [Online]. Available: https://docplayer.net/21072949-Least-squares-intersection-of-lines.html.

[43] C. Constable, "Earth's Electromagnetic Environment," *Surveys in Geophysics*, vol. 37, pp. 27–45, 2016, ISSN: 15730956. DOI: 10.1007/s10712-015-9351-1.

[44] Sensys, *Sensys FGM3D Matrix of Technical Parameters*. [Online]. Available: https://sensysmagnetometer.com/products/sensors-recorder/fgm3d-magnetometer/.

[45] Impact Subsea, *ISA500*, 2019. [Online]. Available: http://www.impactsubsea.co.uk/isa500/.

[46] M. Ardelean and P. Minnebo, "HVDC submarine power cables in the world," Tech. Rep., 2015. DOI: 10.2790/023689.

[47] B. Sensortec, "BNO055: Intelligent 9-axis absolute orientation sensor," Tech. Rep., 2016. [Online]. Available: https://www.robot-electronics.co.uk/files/BNO055.pdf.

[48] A. Nastase, *How to derive the RMS Value of a Sine Wave with a DC Offset*, 2012. [Online]. Available: https://masteringelectronicsdesign.com/how-to-derive-the-rms-value-of-a-sine-wave-with-a-dc-offset/.

[49] M. Bansal, "Performance evaluation of Butterworth Filter for Signal Denoising," *International Journal of Electronics & Communication Technology*, vol. 1, no. 1, pp. 59–62, 2010.

[50] B. C. Veen, *Very Low Frequency Filtering: Do it Right Using Downsampling*, 2015. [Online]. Available: https://allsignalprocessing.com/very-low-frequency-filtering/.

[51] J. Jeedella, H. Al-Ahmad, R. Shubair, and M. Al-Mualla, "Design of IIR filters for a limited number of samples with optimum dynamic frequency responses," in *IEEE International Symposium on Signal Processing and Information Technology (ISSPIT)*, IEEE, 2009, pp. 430–435, ISBN: 1424459508.

[52] R. Pal, "Comparison of the design of FIR and IIR filters for a given Specification and removal of phase distortion from IIR filters," in *2017 International Conference on Advances in Computing, Communication and Control (ICAC3)*, IEEE, 2017, pp. 1–3, ISBN: 1538638525.

[53] P. Stoica and R. L. Moses, *Spectral analysis of signals*. Pearson Prentice Hall Upper Saddle River, NJ, 2005.

[54] O. M. Solomon Jr, "PSD computations using Welch's method," *NASA STI/Recon Technical Report N*, vol. 92, 1991.

[55] Crystal Instruments, *Advanced Dynamic Signal Analysis*, 2009. [Online]. Available: https://www.crystalinstruments.com/dynamic-signal-analysis-basics.

[56] J. W. Cooley, P. A. W. Lewis, and P. D. Welch, "The application of the fast Fourier transform algorithm to the estimation of spectra and cross-spectra," *Journal of sound and vibration*, vol. 12, no. 3, pp. 339–352, 1970, ISSN: 0022-460X.

Appendix A

Figures

A-1 Convergence and array studies

A-1-1 Cable tracker system I

	Estimate (c_x, c_y, c_z, I)	c_r	Occurrence %
Array 1	(-0.40, 2.94, 1.95, 0.098)	3.55	43
	(0.40, 2.94, 1.95, 0.098)	3.55	43
	(0.00, 2.98, 1.95, 0.099)	3.56	14
Array 2	(0.02, 2.97, 1.97, 0.099)	3.56	96
	(-0.07, 0.03, 0.01, 0.008)	0.08	4
Array 3	(0.33, 2.95, 1.97, 0.098)	3.56	36
	(+0.33, 2.95, 1.97, 0.098)	3.56	36
	(0.00, 2.98, 1.98, 0.099)	3.58	28
Array 4	(0.00, 2.96, 1.97, 0.098)	3.56	96
	(-0.12, 0.03, 0.02, 0.009)	0.12	4
Array 5	(*, 2.93, *, 0.098)	*	97
	(*, 4.32, *, 0.119)	*	3
Array 6	(*, *, 1.98, 0.099)	*	100

Table A-1: Results of convergence and array study for CTS I and cable setup C1. Inversion parameters which cannot be consistently found are market with a star.

	Estimate	Occurrence %
Array 1	(0.00, 2.99, 2.99, 0.12)	100
Array 2	(2.01, 2.17, 1.91, 0.097)	98
	(-0.06, 0.02, 0.01, 0.008)	2
Array 3	(-1.51, 2.78, 2.63, 0.114)	34
	(1.51, 2.78, 2.63, 0.114)	34
	(0.00, 3.22, 3.04, 0.122)	32
Array 4	(1.99, 2.15, 1.91, 0.097)	98
	(0.12, 0.02, 0.02, 0.001)	2
Array 5	(*, 4.14, *, 0.319)	100
Array 6	(*, *, 1.98, 0.099)	100

Table A-2: Results of convergence and array study for CTS I and cable setup C2. Inversion parameters which cannot be consistently found are market with a star.

	Estimate	Occurrence %
Array 1	(*, 0.00, 5.42, 0.15)	100
Array 2	(3.01, 0.00, 2.04, 0.101)	97
	(0.05, 0.00, 0.001, 0.01)	3
Array 3	(*, 0.00, *, 0.18)	100
Array 4	(3.00, 0.00, 2.04, 0.100)	97
	(0.09, 0.00, 0.02, 0.011)	3
Array 5	(*,*,*,*,*)	100
Array 6	(*, *, 1.98, 0.099)	100

Table A-3: Results of convergence and array study for CTS I and cable setup C3. Inversion parameters which cannot be consistently found are market with a star.

	Estimate	Occurrence %
Array 1	(0.00, 0.00, 3.46, 0.098)	100
Array 2	(0.00, 0.01, 3.56, 0.099)	100
Array 3	(0.00, 0.00, 3.56, 0.098)	100
Array 4	(0.03, 0.12, 3.55, 0.098)	98
	(0.00, 0.00, 0.04, 0.011)	2
Array 5	(*, 0.00, *, 0.14)	100
Array 6	(*, *, 3.485, 0.098)	100

Table A-4: Results of convergence and array study for CTS I and cable setup C4. Inversion parameters which cannot be consistently found are market with a star.

A-1-2 Cable tracker system II

	Estimate	Occurrence %
Array 1	(0.00, 2.98, 1.98, 0.099)	89
	(*, *, *, 0.001)	11
Array 2	(0.00, 2.97, 1.98, 0.099)	89
	(0, 0.19, 0.12, 0.000)	11
Array 3	(0.00, 2.97, 1.98, 0.098)	89
	(0, 0.26, 0.18, 0.000)	11
Array 4	(0.00, 2.97, 1.98, 0.099)	89
	(0, 0.26, 0.18, 0.000)	11
Array 5	(0.00, 2.97, 1.98, 0.099)	89
	(0, 0.26, 0.18, 0.000)	11
Array 6	(0.00, 2.97, 1.98, 0.099)	89
	(0, 0.29, 0.2, 0.000)	11

Table A-5: Results of convergence and array study for CTS II and cable setup C1. Inversion parameters which cannot be consistently found are market with a star.

	Estimate	Occurrence %
Array 1	(2.11, 2.11, 1.98, 0.099)	89
	(*, *, *, 0.000)	11
Array 2	(2.10, 2.10, 1.98, 0.099)	89
	(0.16, 0.16, 0.15, 0.000)	11
Array 3	(2.10, 2.10, 1.99, 0.099)	89
	(0.22, 0.22, 0.01, 0.003)	11
Array 4	(2.10, 2.10, 1.99, 0.099)	89
	(0.22, 0.22, 0.01, 0.003)	11
Array 5	(2.10, 2.10, 1.98, 0.099)	89
	(0.15, 0.15, 0.14, 0.000)	11
Array 6	(2.10, 2.10, 1.98, 0.099)	89
	(0.21, 0.21, 0.20, 0.001)	11

Table A-6: Results of convergence and array study for CTS II and cable setup C2. Inversion parameters which cannot be consistently found are market with a star.

	Estimate	Occurrence %
Array 1	(2.97, 0.00, 1.98, 0.099)	89
	(0.38, 0.00, 0.19, 0.011)	11
Array 2	(2.97, 0.00, 1.98, 0.099)	89
	(0.08, 0.00, 0.24, 0.000)	11
Array 3	(2.97, 0.00, 1.98, 0.099)	89
	(0.19, 0.00, 0.12, 0.000)	11
Array 4	(2.97, 0.00, 1.98, 0.099)	89
	(0.32, 0.00, 0.00, 0.000)	11
Array 5	(*, *, *, *)	100
Array 6	(2.97, 0.00, 1.98, 0.099)	89
	(0.29, 0.00, 0.20, 0.001)	11

Table A-7: Results of convergence and array study for CTS II and cable setup C3. Inversion parameters which cannot be consistently found are market with a star.

	Estimate	Occurrence %
Array 1	(0.00, 0.00, 0.00, 0.011)	100
Array 2	(0.05, 0.05, 3.56, 0.099)	89
	(0.03, 0.03, 0.01, 0.000)	11
Array 3	(0.10, 0.10, 3.56, 0.099)	89
	(0.00, 0.00, 0.00, 0.000)	11
Array 4	(2.97, 0.00, 1.98, 0.099)	89
	(0.32, 0.00, 0.00, 0.000)	11
Array 5	(0, 0, 0, 0)	100
Array 6	(0.00, 0.00, 3.57, 0.099)	89
	(0.00, 0.00, 0.01, 0.000)	11

Table A-8: Results of convergence and array study for CTS II and cable setup C4.

A-1-3 Cable tracker system III

	Estimate
Array 1	(0.00,3.00,2.00,*)
Array 2	(0.00,3.00,2.00,*)
Array 3	(0.00,3.00,2.00,*)
Array 4	(0.00,3.00,2.00,*)
Array 5	(0.00,3.00,2.00,*)
Array 6	(0.00,3.00,2.00,*)

Table A-9: Results of convergence and array study for CTS III and cable setup C1. Inversion parameters which cannot be consistently found are market with a star.

	Estimate
Array 1	(2.12,2.12,2.00,*)
Array 2	(2.12,2.12,2.00,*)
Array 3	(2.12,2.12,2.00,*)
Array 4	(2.12,2.12,2.00,*)
Array 5	(2.12,2.12,2.00,*)
Array 6	(2.12,2.12,2.00,*)

Table A-10: Results of convergence and array study for CTS III and cable setup C2. Inversion parameters which cannot be consistently found are market with a star.

	Estimate
Array 1	(3.00,0.00,2.00,*)
Array 2	(3.00,0.00,2.00,*)
Array 3	(3.00,0.00,2.00,*)
Array 4	(3.00,0.00,2.00,*)
Array 5	(0.00,0.00,0.00,*)
Array 6	((3.00,0.00,2.00,*)

Table A-11: Results of convergence and array study for CTS III and cable setup C3. Inversion parameters which cannot be consistently found are market with a star.

	Estimate
Array 1	(0.00,0.00,3.60,*)
Array 2	(0.00,0.00,3.60,*)
Array 3	(0.00,0.00,3.60,*)
Array 4	(0.00,0.00,3.60,*)
Array 5	(0.00,0.00,3.60,*)
Array 6	(0.00,0.00,0.00,*)

Table A-12: Results of convergence and array study for CTS III and cable setup C4. Inversion parameters which cannot be consistently found are market with a star.

A-2 Performance in noise disturbed domain

A-2-1 The artificial marine environment

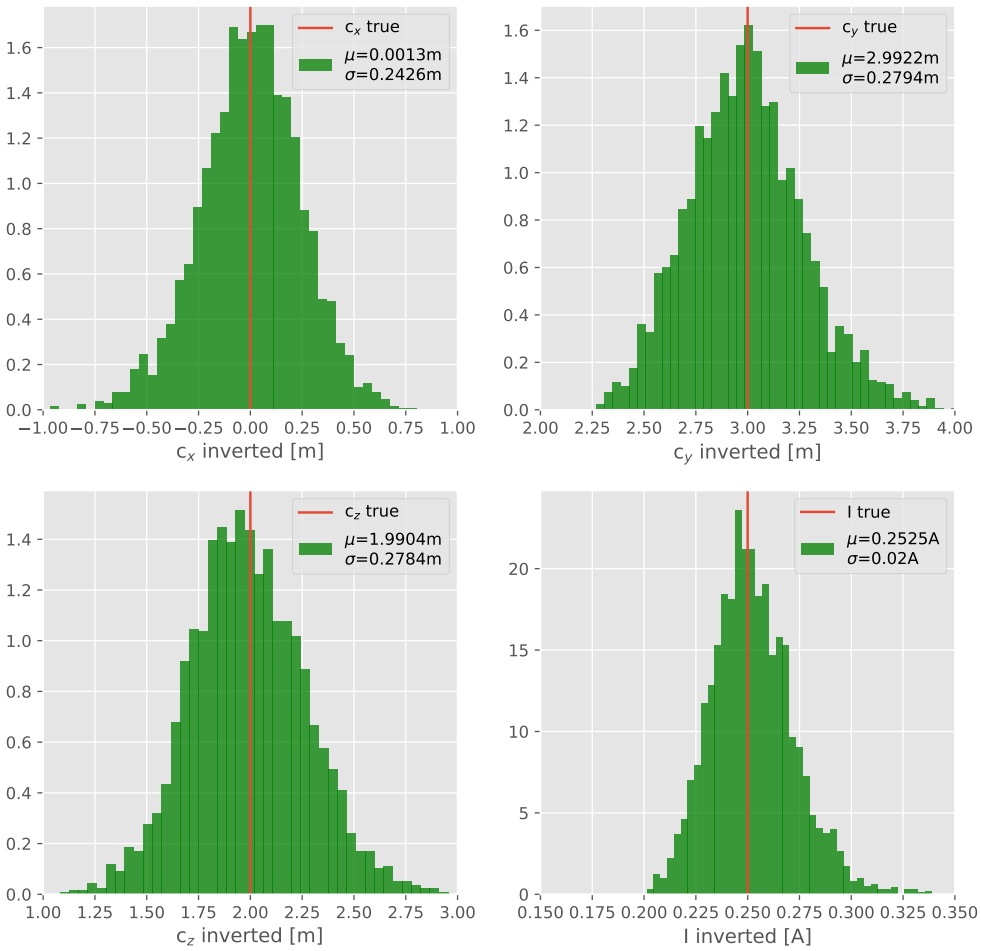

Figure A-1: Inversion results of cable setup C1 in sea water with noise for CTS I and Array 2. For a statistical representation, 3000 iterations are executed. Besides the histogram, the standard deviation σ and mean μ are shown.

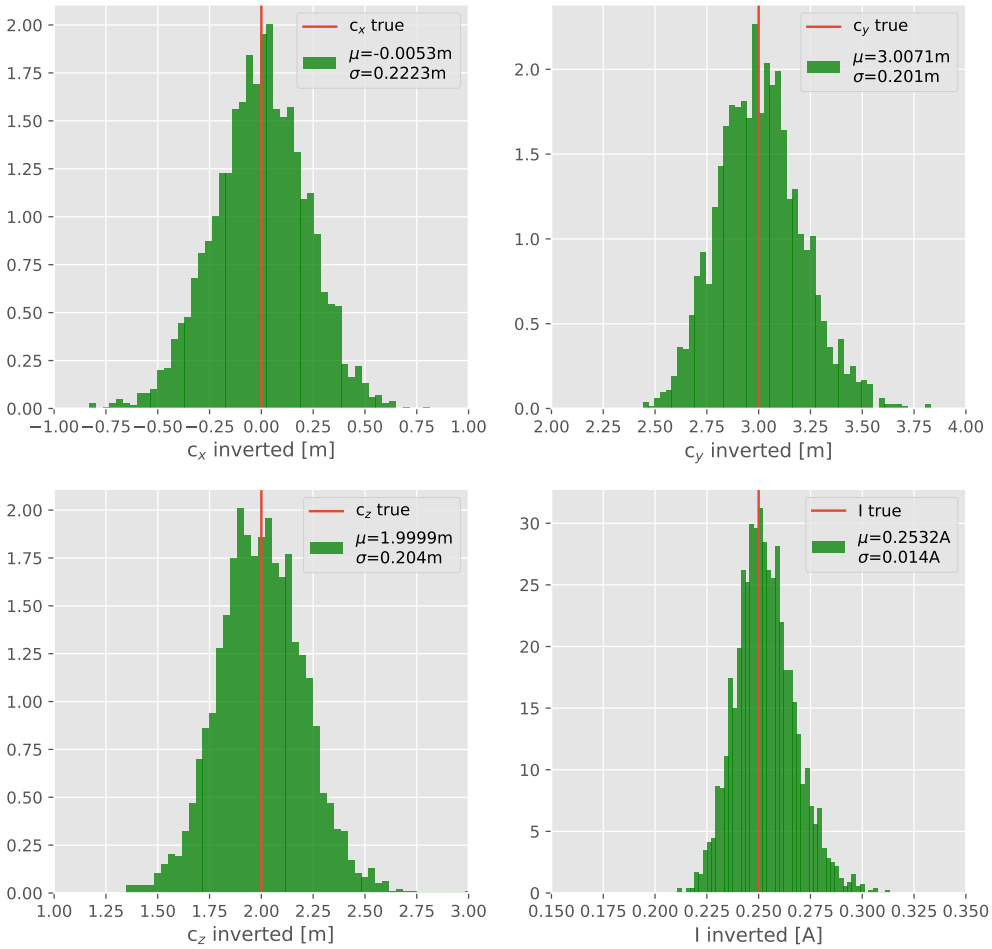

Figure A-2: Inversion results of cable setup C1 in sea water with noise for CTS I and Array 4. For a statistical representation, 3000 iterations are executed. Besides the histogram, the standard deviation σ and mean μ are shown.

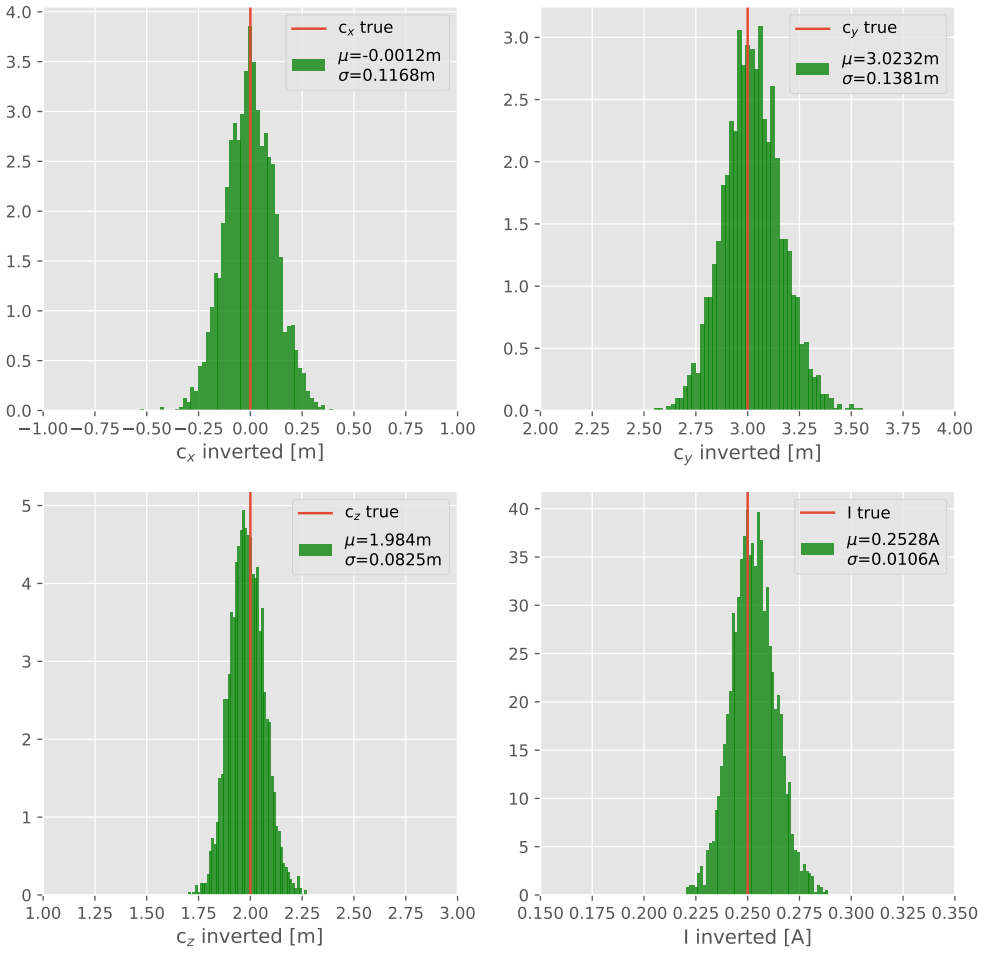

Figure A-3: Inversion results of cable setup C1 in sea water with noise for CTS II and Array 5. For a statistical representation, 3000 iterations are executed. Besides the histogram, the standard deviation σ and mean μ are shown.

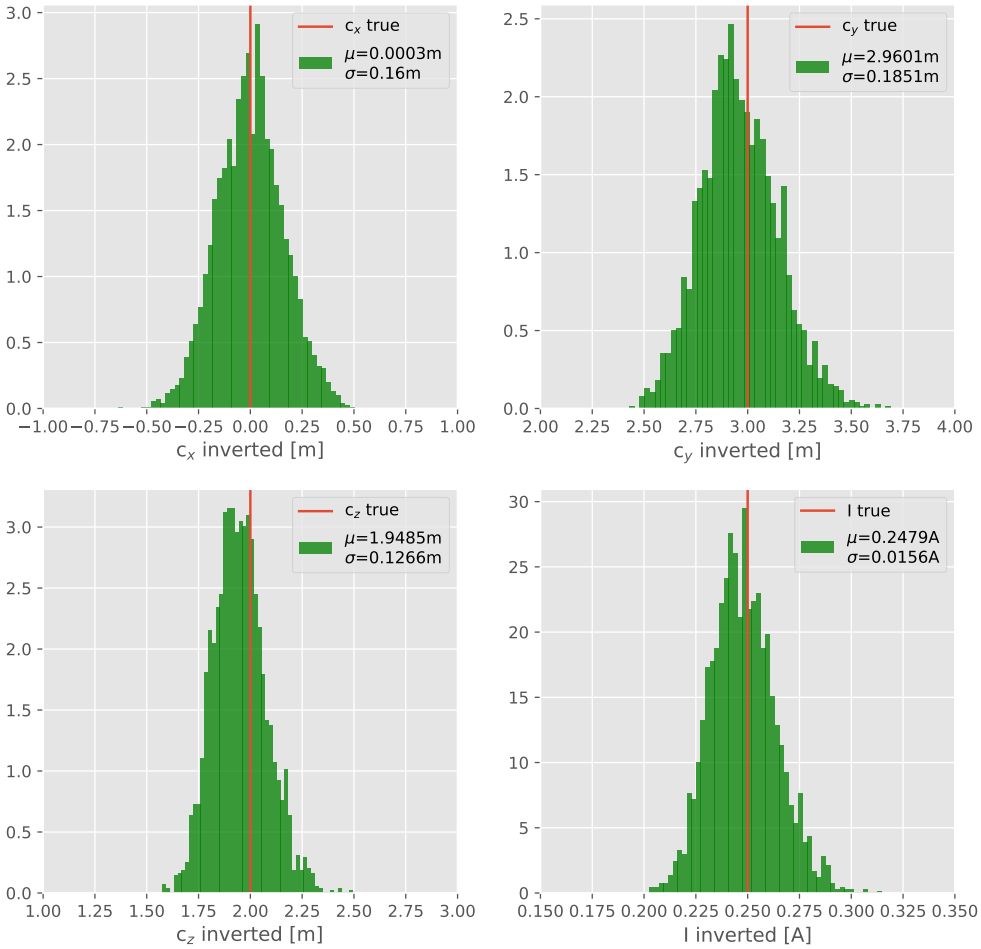

Figure A-4: Inversion results of cable setup C1 in sea water with noise for CTS II and Array 6. For a statistical representation, 3000 iterations are executed. Besides the histogram, the standard deviation σ and mean μ are shown.

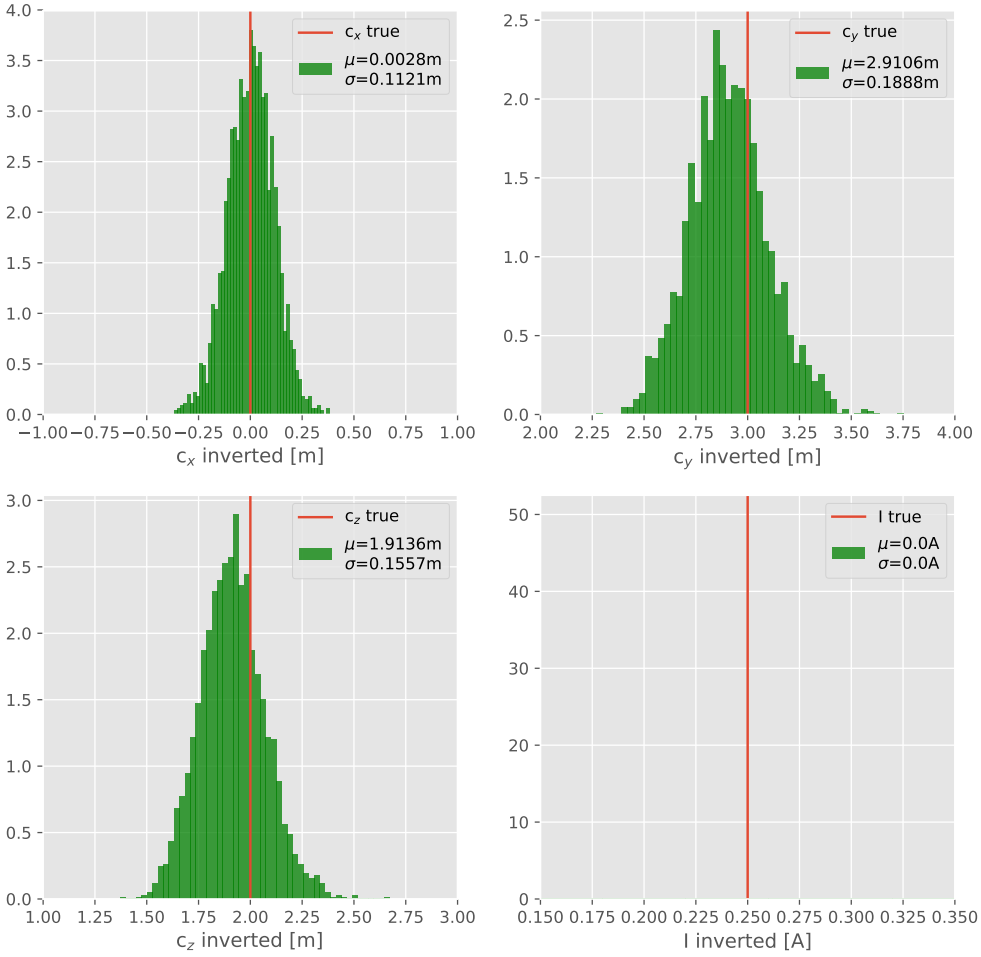

Figure A-5: Inversion results of cable setup C1 in sea water with noise for CTS III and Array 5. For a statistical representation, 3000 iterations are executed. Besides the histogram, the standard deviation σ and mean μ are shown.

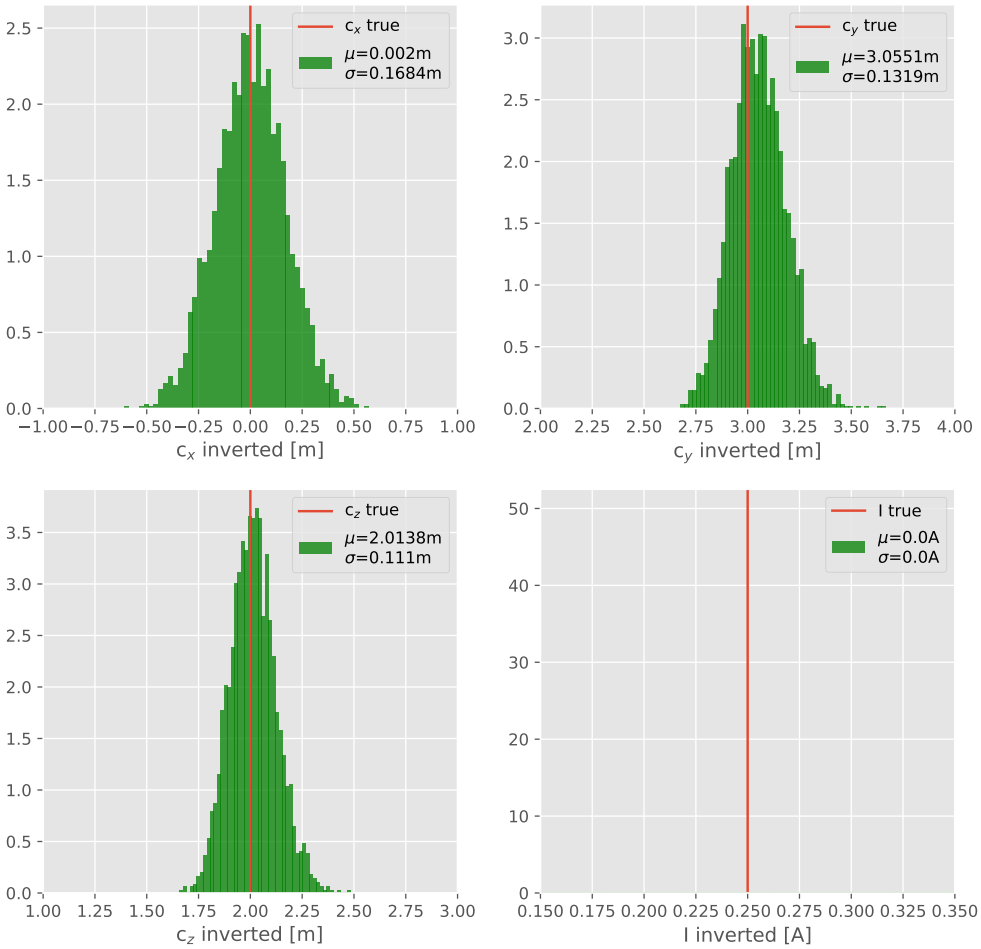

Figure A-6: Inversion results of cable setup C1 in sea water with noise for CTS III and Array 6. For a statistical representation, 3000 iterations are executed. Besides the histogram, the standard deviation σ and mean μ are shown.

A-2-2 Distance study

Cable tracker system I

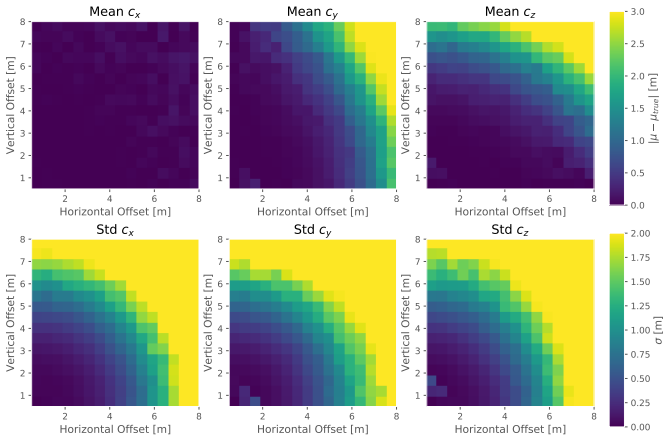

Figure A-7: Distance study of CTS I and Array 2 with azimuth angle between sensor frame and cable of $22.5°$. The model domain consists of sea water and noise.

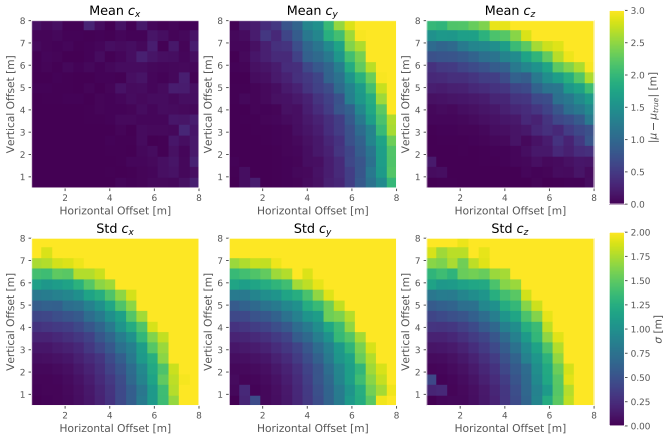

Figure A-8: Distance study of CTS I and Array 2 with azimuth angle between sensor frame and cable of $45°$. The model domain consists of sea water and noise.

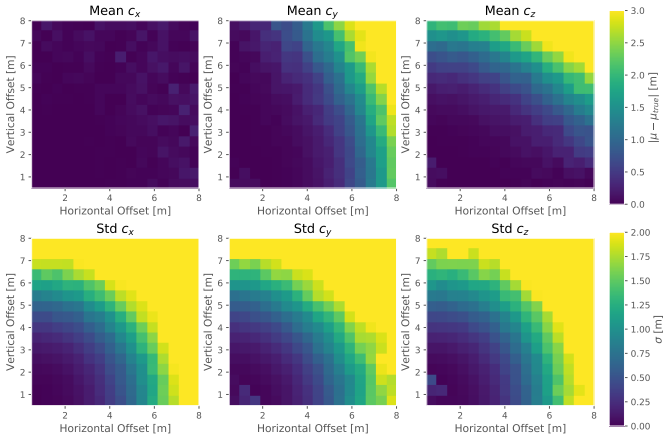

Figure A-9: Distance study of CTS I and Array 2 with azimuth angle between sensor frame and cable of $66.5°$. The model domain consists of sea water and noise.

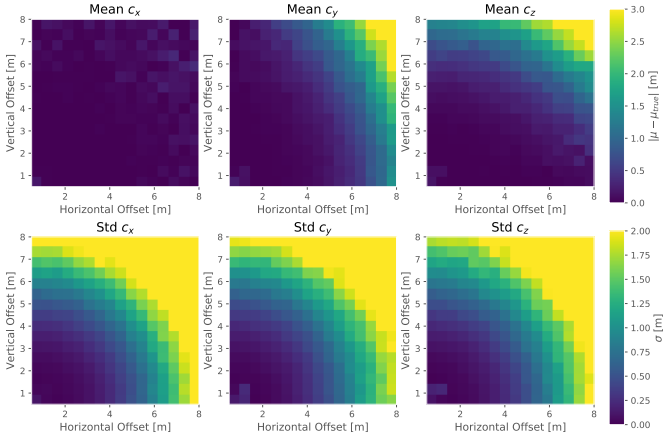

Figure A-10: Distance study of CTS I and Array 4 with azimuth angle between sensor frame and cable of $22.5°$. The model domain consists of sea water and noise.

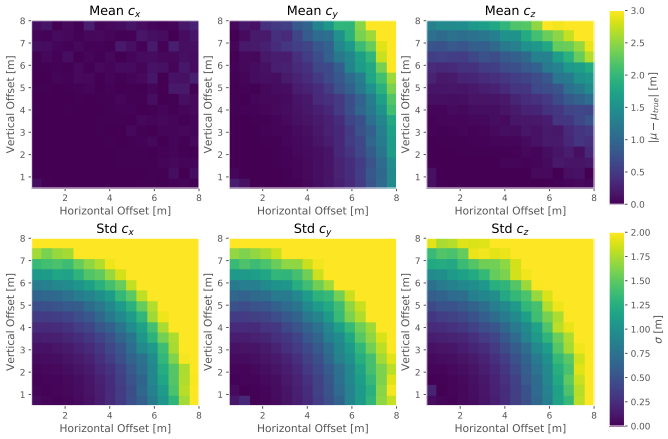

Figure A-11: Distance study of CTS I and Array 4 with azimuth angle between sensor frame and cable of $45°$. The model domain consists of sea water and noise.

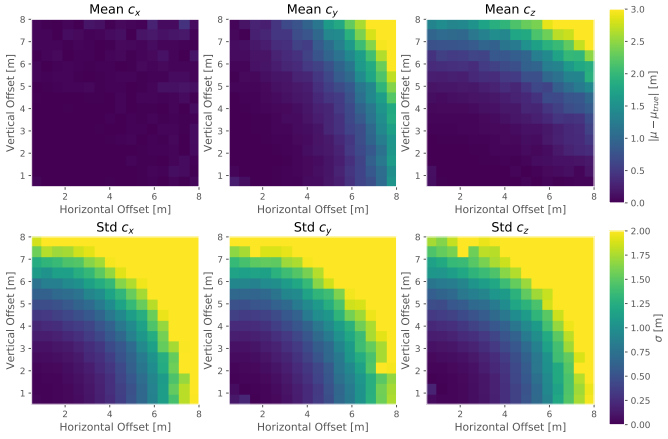

Figure A-12: Distance study of CTS I and Array 4 with azimuth angle between sensor frame and cable of $66.5°$. The model domain consists of sea water and noise.

Cable tracker system II

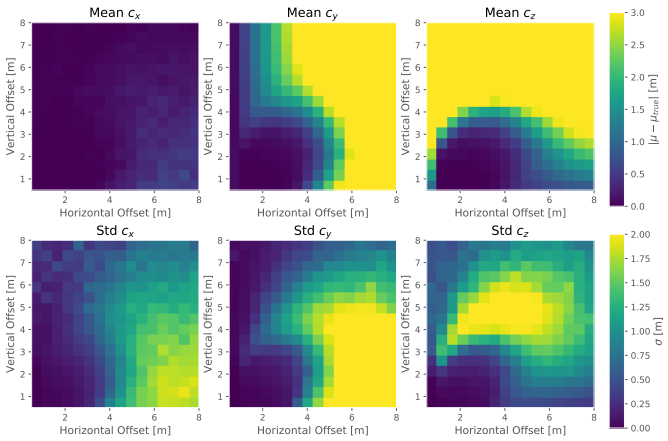

Figure A-13: Distance study of CTS II and Array 5 with azimuth angle between sensor frame and cable of $22.5°$. The model domain consists of sea water and noise.

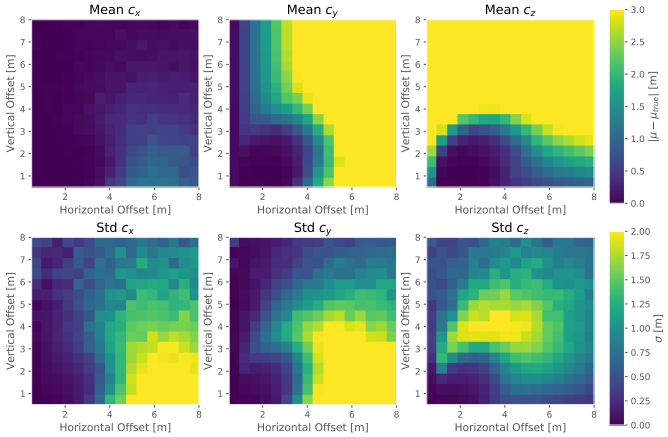

Figure A-14: Distance study of CTS II and Array 5 with azimuth angle between sensor frame and cable of $45°$. The model domain consists of sea water and noise.

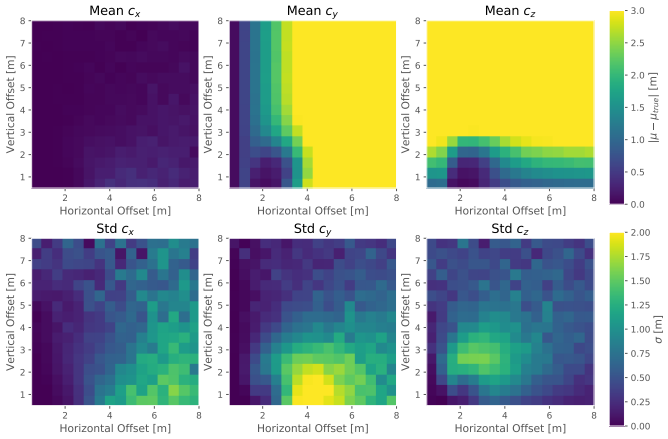

Figure A-15: Distance study of CTS II and Array 5 with azimuth angle between sensor frame and cable of $66.5°$. The model domain consists of sea water and noise.

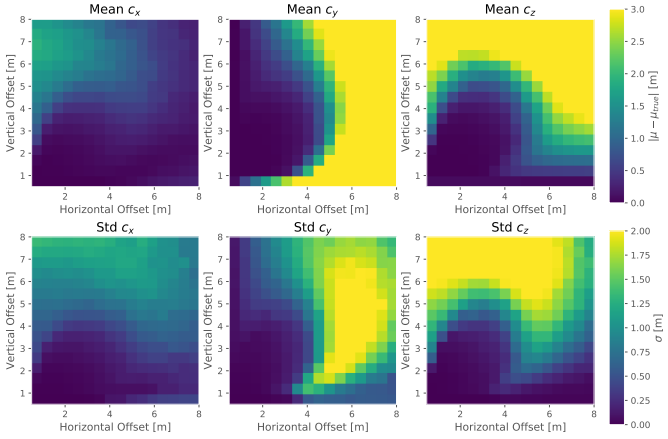

Figure A-16: Distance study of CTS II and Array 6. The model domain consists of sea water and noise.

Cable tracker system III

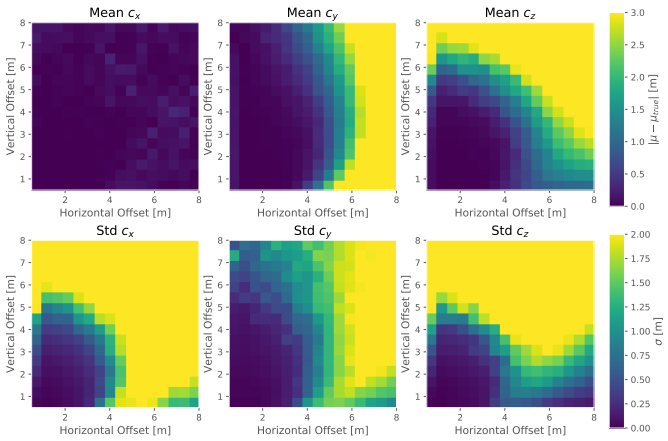

Figure A-17: Distance study of CTS III and Array 5 with azimuth angle between sensor frame and cable of $22.5°$. The model domain consists of sea water and noise.

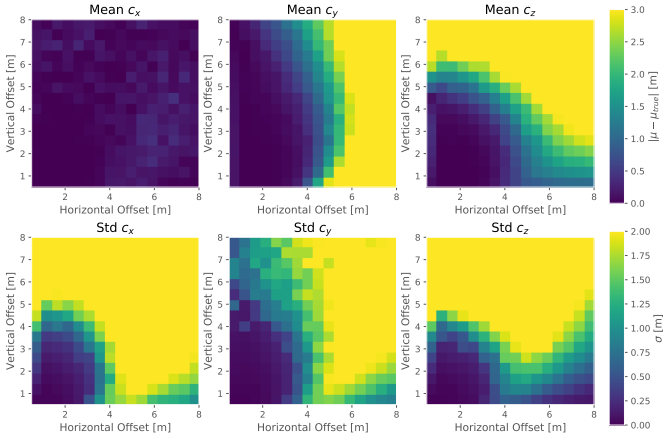

Figure A-18: Distance study of CTS III and Array 5 with azimuth angle between sensor frame and cable of $45°$. The model domain consists of sea water and noise.

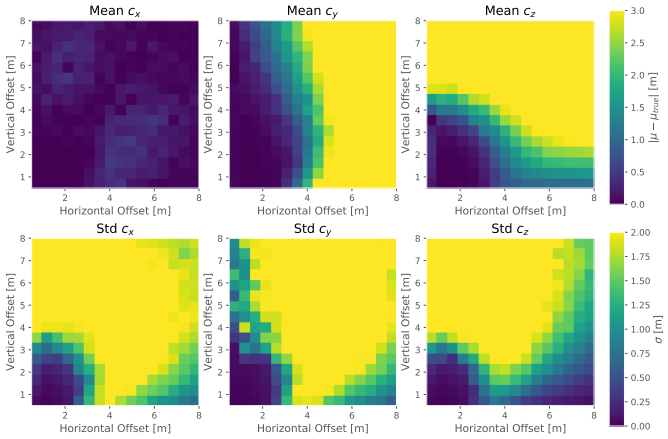

Figure A-19: Distance study of CTS III and Array 5 with azimuth angle between sensor frame and cable of $66.5°$. The model domain consists of sea water and noise.

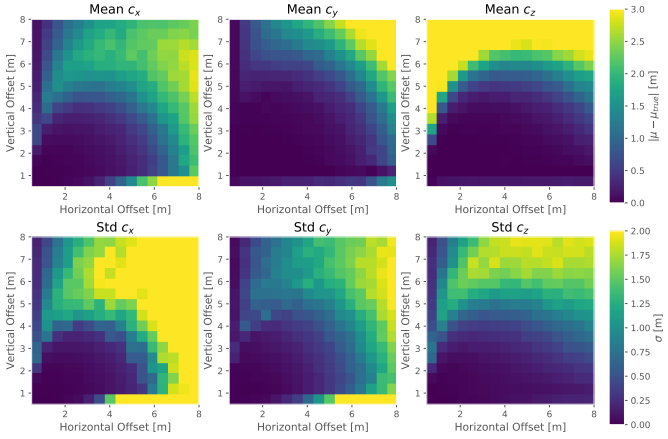

Figure A-20: Distance study of CTS III and Array 6. The model domain consists of sea water and noise.

A-2-3 Influence of tone frequency

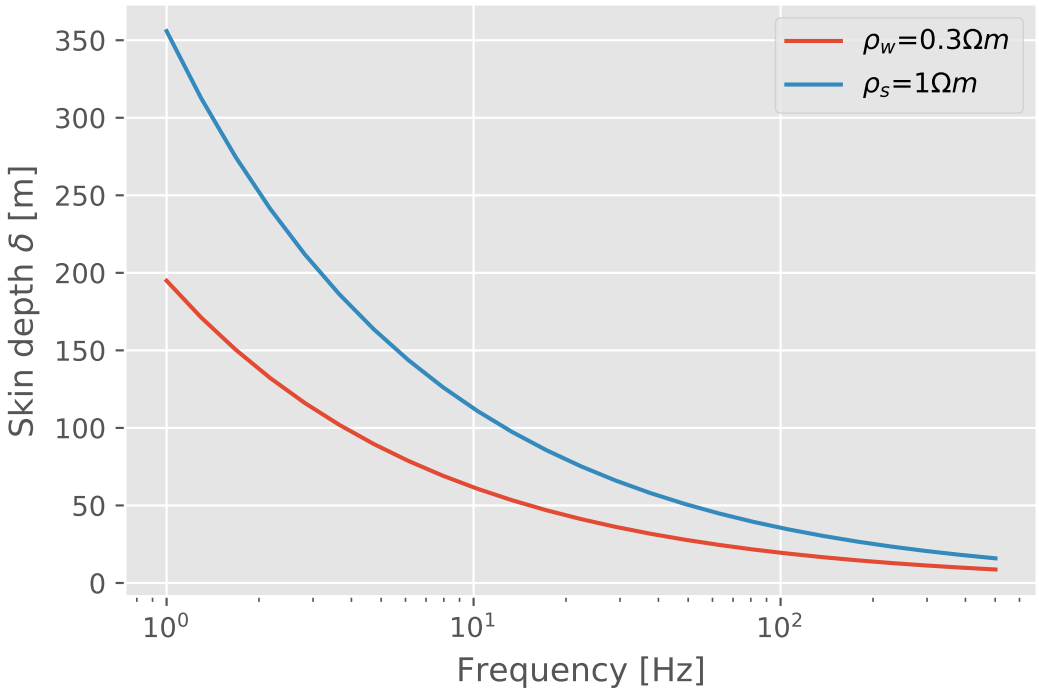

Figure A-21: Frequency dependency of the skin depth δ for sea water ($\rho_w = 0.3\,\Omega\mathrm{m}$) and seabed soil $\rho_s = 1\,\Omega\mathrm{m}$.

A-3 Field cable

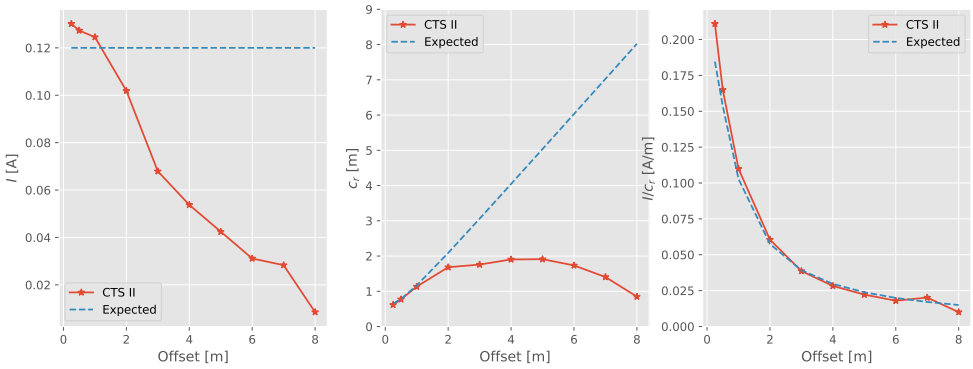

Figure A-22: The inverted and expected current I and distance c_r relative to offset are shown in this figure. Additionally, the inverted and expected ratio of both quantities is displayed.

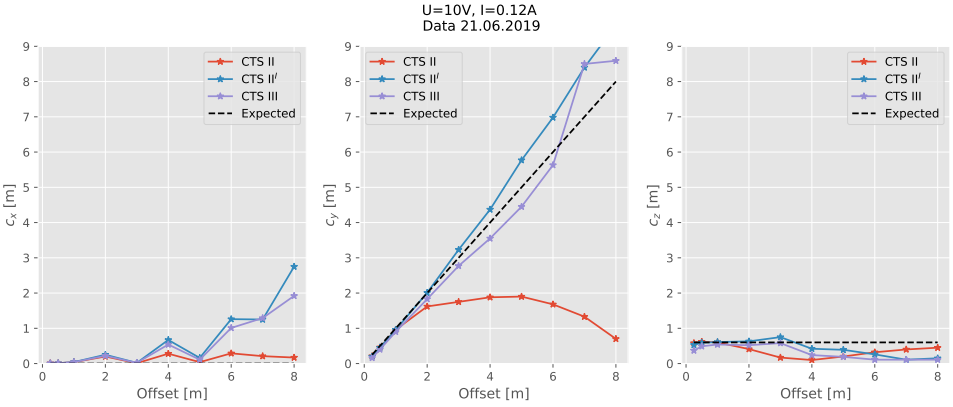

(a) Inversion results from CTS II, CTS^I and CTS III

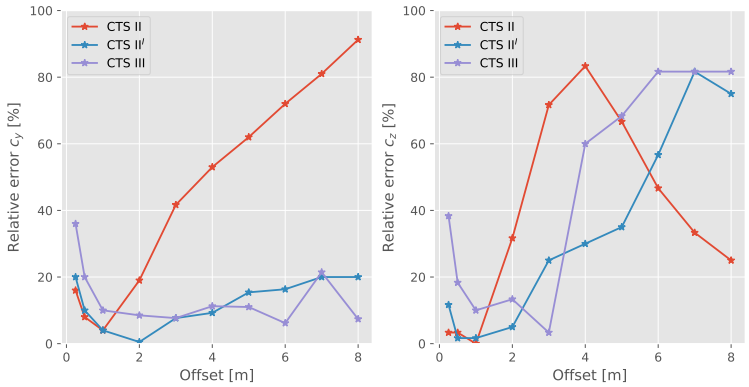

(b) Relative error of inversion results from CTS II, CTS^I and CTS III. The relative error of c_x cannot be calculated.

Figure A-23: The inversion results are shown for CTS II, CTS^I and CTS III in a field experiment on a field wire.

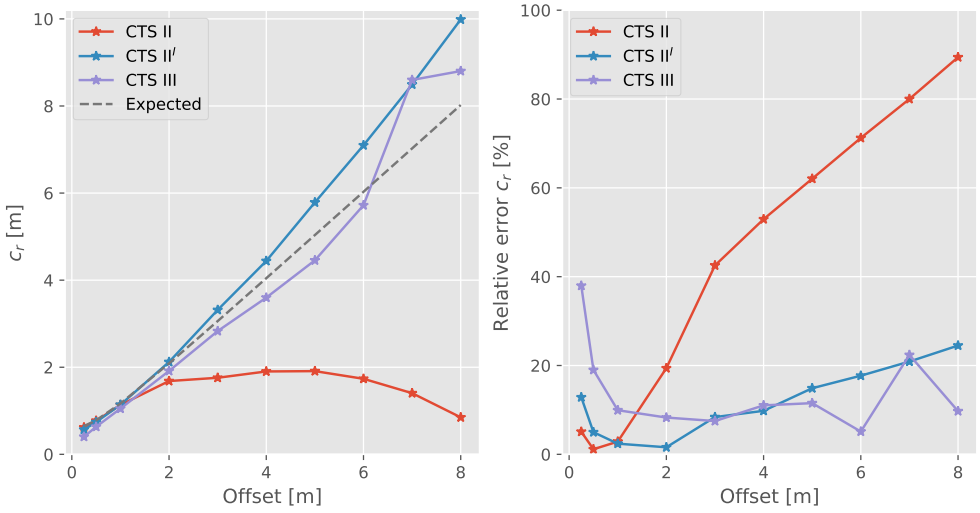

Figure A-24: The inverted and expected distance c_r relative to offset for CTS II, CTS^I and CTS III are shown.